A Process for the Manufacture of High Temperature Bi-epitaxial Josephson Junctions

by

Hendrik Adrianus Cornelis de Villiers

Thesis presented in partial fulfilment of the requirements for the degree of Master of Science in Engineering (Electronic Engineering with Computer Science) at the University of Stellenbosch

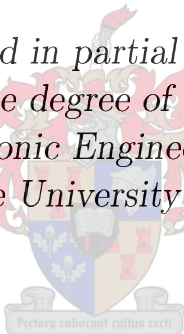

Study leaders:

Prof. W. J. Perold   Dr. C. J. Fourie

March 2007

Copyright © 2007 University of Stellenbosch
All rights reserved.

Declaration

I, the undersigned, hereby declare that the work contained in this thesis is my own original work and that I have not previously in its entirety or in part submitted it at any university for a degree.

Signature: ....

H. A. C. De Villiers

Date: ....

Abstract

This thesis is concerned with the fabrication of high temperature bi-epitaxial grain boundary Josephson junctions for use in superconducting microelectronic circuits. It aims to provide a proof-of-concept manufacturing process which can serve as a basis for future research at the University of Stellenbosch.

The work in this thesis integrates and extends previous work to produce a workable fabrication process. Deposition is performed using pulsed laser deposition (PLD). A pulsed oxygen source and shadow mask are used to improve film quality. The search for working process parameters, as well as the analysis of the resulting thin-films, are discussed. Etching is performed using argon ion milling. This process is outlined, along with a discussion of improvements made to the milling unit to increase process uniformity.

A prototype device is manufactured. An MgO substrate is covered with a CeO_2 seed layer which is then partially removed using argon ion milling. This is followed by the deposition of a thin film of the high temperature superconductor YBCO. Grain boundaries form along the borders separating the regions with and without seed layer coverage. The YBCO thin film is patterned to create the desired circuit. Contact pad metallisation using gold is also performed so that the circuit can be connected electrically to outside systems.

The successful creation of grain boundary junctions is demonstrated and electrical characterisation is performed on them. The Josephson effect is demonstrated in the prototype device at temperatures up to 60 K. The AC Josephson effect and critical current modulation are observed. Future improvements of the process are discussed along with possible applications.

Opsomming

Hierdie tesis handel oor die vervaardiging van hoë temperatuur bi-epitaksiële korrelgrens Josephson skakels vir gebruik in supergeleidende mikroelektroniese bane. Dit beoog die ontwikkeling van 'n konsepvervaardigingsproses wat as grondslag kan dien vir toekomstige navorsing by die Universiteit van Stellenbosch.

Die werk in hierdie tesis integreer vorige werk en brei dit uit om 'n werkende vervaardigingsproses op te lewer. Deposisie word deur middel van gepulseerde laser deposisie (PLD) gedoen. 'n Gepulseerde suurstofbron en 'n skadumasker word aangewend om die kwaliteit van lagies te verbeter. Die soektog na werkende prosesparameters, asook die analise van die resulterende dunfilms, word bespreek. Argon ioonetsing word aangewend om lagies te ets. Hierdie proses word beskryf met 'n saamgaande bespreking oor veranderings wat aangebring is tot die proses om uniformiteit te verbeter.

'n Prototipe toestel word vervaardig. 'n MgO substraat word bedek met 'n CeO_2 kiemlaag wat daarna gedeeltelik verwyder word deur middel van argon ioonetsing. Hierdie word gevolg deur die deposisie van 'n dun film van die hoë temperatuur supergeleier YBCO. Korrelgrense vorm waar gebiede met en sonder kiemlaagdekking bymekaar kom. Die YBCO dun film word geëts om die verlangde stroombaan te vorm. Goud deposisie word gebruik om die stroombaankontakte voor te berei vir konneksie met eksterne stroombane.

Die suksesvolle vervaardiging van korrelgrens skakels word gedemonstreer en elektriese karakterisering word op hulle uitgevoer. Die Josephson effek word gedemonstreer in die prototipe by temperature tot en met 60 K. Die WS Josephson effek en kritiese stroom modulasie word waargeneem. Toekomstige verbeterings tot die proses, asook moontlike toepassings, word bespreek.

Pectora roborant cultus recti

Acknowledgements

I would like to express my sincere gratitude to the following people and organisations who have contributed to making this work possible:

- Wynand van Staden for his friendship, his willingness to help and encouragement throughout this time.
- Ulrich Büttner for his endless enthusiasm, his helpfulness and his inspirational work ethic.
- Akram Elkaseh for his helpfulness and various AFM measurements.
- Dr. V. S. Vallabhapurapu for his advice and encouragement.
- Dr. M. Meinchen for the test trench AFM measurements.
- Jan Gertenbach at anorganic chemistry for the use of their X-ray powder diffractometer.
- Dr. R. Bucher at iThemba labs for his help doing the initial X-ray diffraction scans which preceded the work presented here.
- Ulli Deutschländer, Dr. C. Steenkamp, Pieter Neethling and Gurthwin Bosman at the Laser Research Institute (LRI) for their assistance.
- Anita van der Spuy for her constant readiness in dealing with the material suppliers.
- Viola Lengner for keeping me on track.
- The Wilhelm Frank Trust and the Harry Crossley Foundation for their financial support throughout this work.

- Prof. W. J. Perold and Dr. C. J. Fourie of the University of Stellenbosch as my study leaders for their continued support and encouragement.

- Finally, to all my family and friends. Thank you for your understanding, love and support throughout this time. It is deeply appreciated.

Contents

Declaration **ii**

Abstract **iii**

Opsomming **iv**

Acknowledgements **v**

Contents **vii**

List of Figures **xi**

List of Tables **xiv**

Nomenclature **xv**

1 Introduction **1**

2 Josephson Junctions **5**

2.1 Introduction 5
2.2 Superconducting Tunnel Junctions 6
2.3 Basic Lumped Junctions 6
2.4 Generalised Josephson Junctions 7
2.5 Resistively Shunted Junctions 11
2.5.1 DC Excitation 11
2.5.2 AC Excitation 12
2.6 Magnetic Field Effects 15
2.7 Summary 16

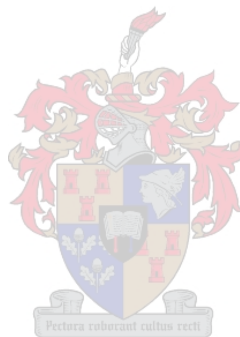

3 High-T_c Josephson Junctions **17**
3.1 Introduction 17
3.2 High-T_c Specific Issues 17
3.3 High-T_c Junction Types 18
3.3.1 Extrinsic Junctions 18
3.3.2 Intrinsic Junctions 19
3.4 Grain Boundaries 20
3.4.1 Grain Boundary Types 20
3.5 Engineered Grain Boundaries 21
3.5.1 Bicrystal junctions 21
3.5.2 Step-edge Junctions 22
3.5.3 Bi-epitaxial Grain Boundaries 23
3.6 Review of Previous Work 24
3.7 Bi-epitaxial Junctions 26
3.7.1 Background 26
3.7.2 Single Seed Layer Approach 28
3.7.3 Fabrication 29
3.8 Summary 30

4 Crystal Orientation in Thin-Films **31**
4.1 Introduction 31
4.2 Texturing in Thin-Films 31
4.2.1 Epitaxial growth 32
4.2.2 In-plane Texturing 33
4.3 Overview of Powder Diffraction 33
4.3.1 Lattice Planes 34
4.3.2 Bragg Diffraction 35
4.3.3 X-ray Powder Diffractometers 37
4.3.4 Powder Diffraction Patterns 37
4.3.5 Effects of Preferred Orientation 38
4.3.6 Seed Layer Diagnostics 38
4.4 Summary 40

5 Pulsed Laser Deposition **41**
5.1 Introduction 41

Pectora roborant cultus recti

5.2 Process Overview . . . 42
5.2.1 Experimental Setup . . . 42
5.2.2 Key Process Parameters . . . 45
5.2.3 Laser Ablation Events . . . 47
5.3 PLD Configurations . . . 48
5.3.1 Standard On-axis PLD . . . 48
5.3.2 Non-Standard PLD Configurations . . . 49
5.4 Pulsed Oxygen Source . . . 55
5.4.1 Valve timing . . . 55
5.5 YBCO Deposition . . . 57
5.6 Seed Layer Deposition . . . 58
5.6.1 Normal PLD of Cerium Oxide . . . 59
5.6.2 PLD of Cerium Oxide with a Pulsed Oxygen Source . . . 61
5.6.3 Cerium Oxide Seed Layer with YSZ Buffer Layer . . . 62
5.7 Summary . . . 63

6 Thin-Film Patterning **65**
6.1 Introduction . . . 65
6.2 Ultraviolet Photolithography . . . 65
6.2.1 Procedure . . . 66
6.3 Argon Ion Milling . . . 67
6.3.1 Process Overview . . . 67
6.3.2 Local Milling Facility . . . 68
6.3.3 Mill Operation . . . 69
6.4 Summary . . . 72

7 Device Fabrication **73**
7.1 Introduction . . . 73
7.2 Seed Layer Deposition . . . 73
7.2.1 Optical Inspection . . . 75
7.2.2 Layer Crystallinity . . . 75
7.3 Seed Layer Patterning . . . 76
7.4 YBCO Deposition . . . 80
7.5 YBCO Patterning . . . 83
7.6 Gold Pads and Wirebonding . . . 87

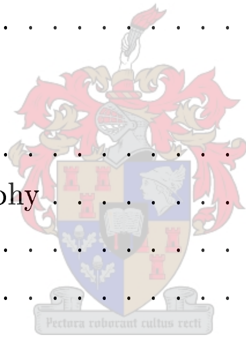
Pectora roborant cultus recti

7.7 Summary 88

8 Device-level Testing and Results **90**

8.1 Introduction 90

8.2 I(V) Characteristics 91

8.2.1 Test Setup 91

8.2.2 Results 92

8.3 AC Josephson Effect 94

8.3.1 Test Setup 94

8.3.2 Results 94

8.4 Critical Current Modulation 96

8.4.1 Test Setup 96

8.4.2 Results 97

8.5 Summary 99

9 Conclusions and Recommendations **101**

9.1 Conclusion 101

9.2 Recommendations 103

A Pulsed Valve Control **106**

A.1 Timing generator 106

A.2 Valve driver unit 108

B X-ray Diffraction Results **110**

C Supplementary Results **123**

D Axial Field of a Helmholtz Coil **126**

E Electron Back-scatter Diffraction **128**

Bibliography **131**

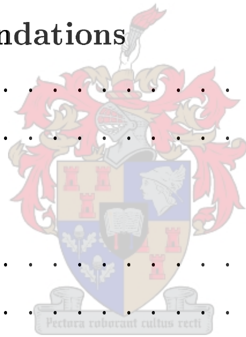

List of Figures

2.1 Structure of a tunnel junction 6
2.2 I(V) curve of a Josephson junction at 0K 8
2.3 I(V) curve of a Josephson junction with sub-gap conduction 9
2.4 The generalised Josephson junction model 10
2.5 The influence of β_c in the RSJ model (adapted from [26]) 12
2.6 The AC Josephson effect (adapted from [26]) 14
2.7 Geometry for critical current modulation 15
2.8 Critical current of a short junction in a magnetic field 16

3.1 Extrinsic junctions: (a) Step-edge SNS (b) Ramp-edge (adapted from [20]) . . 19
3.2 Intrinsic junctions: (a) Microbridge (b) C-Axis coupling step 20
3.3 Grain boundary types (adapted from [14]) 21
3.4 Grain boundary junctions: (a) Bicrystal (b) Step-edge 22
3.5 Generalised bi-epitaxial junction structure 27
3.6 Bi-epitaxy using only a seed layer 29
3.7 Direct method for CeO_2-based junction fabrication 30

4.1 Epitaxial thin-film 32
4.2 Thin-film with no in-plane texturing 33
4.3 Thin-film with in-plane texturing 34
4.4 Two-dimensional example of Miller indices (adapted from [16]) 35
4.5 Bragg diffraction geometry 36
4.6 The θ–θ Bragg-Brentano Geometry 37
4.7 An example of a CeO_2 powder diffraction pattern 40

5.1 Schematic representation of the PLD setup 42
5.2 Stages of the ablation process (adapted from [1]) 47

5.3 Geometry of standard PLD 49
5.4 Geometry of PLD with a pulsed oxygen source (no shadow mask) 51
5.5 Improvement of the surface quality using a shadow mask 53
5.6 Geometry of PLD with pulsed oxygen source (with shadow mask) 54
5.7 Ion gauge signal adapted from [13]. The source did not provide vertical axis divisions. 55
5.8 Plume brightening due to interaction of the gas pulse and the ablation plume . 56
5.9 Susceptibility test for the pulsed oxygen YBCO PLD 58
5.10 Powder diffraction patterns for Samples D1 and D2 62

6.1 Diagram of the local argon ion milling facility 68
6.2 Three-grid accelerator system (adapted from [2]) 70
6.3 AFM image of CeO_2 test trench 72

7.1 Post-deposition seed layer surface 75
7.2 Powder diffraction pattern of the CeO_2 seed layer 76
7.3 Sample outline on step-edge mask by Snetler [32] for seed layer photomasking 77
7.4 Photoresist mask for the boundary (white region is CeO_2) 78
7.5 Post-mill device surface (dark region is the milled area) 79
7.6 Grain boundary after YBCO deposition (dark region is YBCO on CeO_2) . . . 81
7.7 Susceptibility test for the YBCO thin-film 82
7.8 Device mask designed by Snetler [32] 83
7.9 Leg numbering convention 83
7.10 Photoresist pattern showing leg 4 (dark region is YBCO on CeO_2) 85
7.11 Patterned YBCO showing leg 4 (yellow region is CeO_2) 86
7.12 Gold pad with wirebonds 88

8.1 I(V) curve for leg 4 of the prototype (T=42 K) 93
8.2 Critical current versus temperature for leg 4 93
8.3 Shapiro steps at 18.09 GHz for leg 4 of the prototype (T=42 K) 95
8.4 Critical current modulation for leg 4 97
8.5 Illustration of grain boundary faceting 98

A.1 Stanford Research Systems DG535 106
A.2 Timing diagram for synchronisation setup 107
A.3 Valve driver unit 108

B.1 Powder diffraction pattern for sample S1 . . . 110
B.2 Powder diffraction pattern for sample S2 . . . 111
B.3 Powder diffraction pattern for sample S3 . . . 112
B.4 Powder diffraction pattern for sample S4 . . . 113
B.5 Powder diffraction pattern for sample S5 . . . 114
B.6 Powder diffraction pattern for sample S6 . . . 115
B.7 Powder diffraction pattern for sample S7 . . . 116
B.8 Powder diffraction pattern for sample P1 . . . 117
B.9 Powder diffraction pattern for sample P2 . . . 118
B.10 Powder diffraction pattern for sample P3 . . . 119
B.11 Powder diffraction pattern for sample P4 . . . 120
B.12 Powder diffraction pattern for sample D1 . . . 121
B.13 Powder diffraction pattern for sample D2 . . . 122

C.1 I(V) curve for leg 6 of the prototype (T=42 K) . . . 123
C.2 Critical current versus temperature for leg 6 of the prototype . . . 124
C.3 Shapiro steps at 18.00 GHz for leg 6 of the prototype (T=42 K) . . . 125

E.1 Geometry for EBSD analysis (adapted from [29]) . . . 129

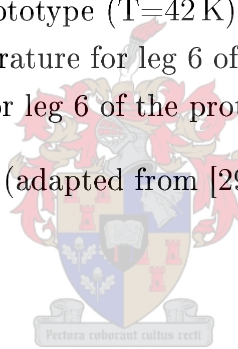

List of Tables

3.1 Selected results for in-plane epitaxial relationships according to Wu *et al* [38] . 28

4.1 2θ values for the (111)- and (200)-peaks in the seed layer materials 39

5.1 Optimal standard PLD parameters for YBCO used by Rottier [30] 57
5.2 Pulsed Oxygen PLD parameters for YBCO 58
5.3 Process parameters for PLD of the seed layer 64

6.1 Energy requirements associated with various physical processes [22] 68

7.1 CeO_2 deposition parameters (sample P1) 74
7.2 Photoresist parameters for seed layer patterning 78
7.3 Seed layer milling parameters 79
7.4 YBCO deposition parameters 80
7.5 Photoresist parameters for YBCO patterning 84
7.6 YBCO milling parameters 84
7.7 Gold deposition parameters 87

A.1 Valve driver output pulse durations 109

Pectora roborant cultus recti

Nomenclature

Constants:

$\mu_0 =$ $4\pi\times10^{-7}$ H/m (Permeability of free space)

$\Phi_0 =$ $\frac{h}{2e} = 2.07 \times 10^{-15}$ T·m^2 (Single flux quantum)

$e =$ 1.602×10^{-19} C (Electron charge)

$h =$ 6.626×10^{-34} J·s (Planck's constant)

Variables:

I_c Critical current

R_n Normal state resistance

V_g Gap voltage ($\frac{2\Delta_0}{e}$)

Δ_0 Gap parameter or gap energy

φ Gauge-invariant phase difference

ξ_{GL} Ginzburg-Landau coherence length

Abbreviations:

cps Counts per second

Low-T$_c$ Low critical temperature

High-T$_c$ High critical temperature

RSJ Resistively shunted junction

RSFQ Rapid Single Flux Quantum

SQUID Superconducting Quantum Interference Device

YBCO Yttrium Barium Copper Oxide ($YBa_2Cu_3O_{7-\delta}$)

YSZ Yttria Stabilised Zirconium

Chapter 1

Introduction

Superconducting microelectronic circuits based on Josephson junctions derive their importance from a few key properties. Firstly, because of the extremely high switching speed of the junctions, they can be used to great effect in building digital circuits. Rapid single flux quantum (RSFQ) circuits, which have the Josephson junction as their fundamental building block, have been demonstrated to operate up to 770 GHz [6]. The extremely low power dissipation of these elements allows them to be packed with much greater density than non-superconducting technologies. Also, because of their sensitivity to magnetic fields, Josephson junctions can be used to make extremely sensitive magnetometers (Superconducting Quantum Interference Devices or SQUIDs), some of the most sensitive magnetometers currently available.

To date, most applications of Josephson junction technology make use of low-T_c superconductors. Although low-T_c circuits are indispensable in the various niches that they occupy, widespread use of them is limited by the need to provide them with a suitable cryogenic environment for operation. Since low-T_c circuits usually operate at 4.2 K, either liquid helium or a cryocooler capable of reaching this temperature is required to cool these devices. Since liquid helium is extremely expensive (as are cryocoolers with this cooling capacity), it would be attractive to be able to operate at higher temperatures.

High-T_c superconductors allow us to meet this need. $YBa_2Cu_3O_{7-\delta}$(YBCO), the high-T_c superconductor used in this thesis, already starts superconducting at 92 K, allowing

one to use liquid nitrogen (which boils at 77 K) to cool devices made from this material. The resultant reduction in cost and setup complexity opens up many new application possibilities and promises to bring older ones to a larger market.

The manufacture of Josephson junctions using high-T_c materials is, however, a non-trivial affair in comparison with low-T_c processes. Because of the extremely short coherence lengths in high-T_c materials, normal tunnel junctions cannot currently be fabricated with the needed reproducibility [20]. Even given that there are alternative ways of producing junctions in these materials, there are many more hurdles to overcome in the deposition and processing of the thin-films.

In order to produce practical devices based on high-T_c materials, we must find a reliable way of manufacturing them. The purpose of this thesis is to explore one such route, bi-epitaxy, and to demonstrate its workability with the equipment available to the researcher.

Bi-epitaxy can be defined as the technique where the in-plane crystallographic orientation of a high-temperature superconductor (YBCO in this case) is controlled by employing a seed layer of a material different to that of the substrate. The superconductor grown on the seed layer has a different crystallographic orientation from that of the superconductor grown directly on the substrate, leading to a grain boundary along the line separating the two regions.

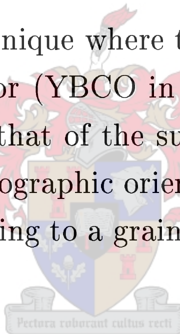

This technique has several advantages, one of which is its relative simplicity. This implies less chance of error due to an overly complicated manufacturing process. Secondly, the positions of the grain boundaries are definable by photolithography, making it possible to place Josephson junctions at arbitrary places on the substrate. Thirdly, there exists the possibility of extending the manufacturing process to multilayer devices. These properties make bi-epitaxy an attractive method for grain boundary fabrication.

Before continuing we will give a quick overview of the contents of the chapters that follow:

Chapter 2 (Josephson Junctions) — Here the general characteristics of Josephson junctions will be discussed, with the focus being on their terminal behaviour for testing and characterisation purposes.

Chapter 3 (High-T_c Josephson Junctions) — In this chapter, issues unique to high-T_c

junctions are delt with. The properties of the various materials employed will be examined, followed by an overview of the different kinds of high-T_c junctions. Special consideration will be given to grain boundary junctions, along with a review of previous work done on these junctions at the University of Stellenbosch. Finally, the method of bi-epitaxy will be discussed.

Chapter 4 (Crystal Orientation in Thin-Films) — An overview will given here of the relevant concepts pertaining to the crystalline structure of thin films. A short review of X-ray powder diffraction is presented, along with selected powder diffraction pattern information for the purpose of thin-film analysis in later chapters.

Chapter 5 (Pulsed Laser Deposition) — Pulsed laser deposition (PLD) is the focus of this chapter, which will commence with an overview of this process. The PLD of the various materials employed in this thesis is then examined. A pulsed oxygen source and a shadow mask are introduced to improve the deposition process. Deposition parameters are then found by experimentation and tabulated. The quality of the resulting thin-films is tested using various techniques.

Chapter 6 (Thin-Film Patterning) — This chapter covers the etching of thin-films using argon ion milling, which allows for the selective removal of material through sputtering with high energy ions. The etch uniformity of the in-house milling equipment is improved through modification of the ion extraction grid. Finally, the etch rates of materials relevant to this work are found and tabulated.

Chapter 7 (Device Fabrication) — The creation of a prototype device is demonstrated using an integrated manufacturing process based on the techniques developed in the preceding chapters. The process parameters employed at each stage are given. The progress at various stages of the process is monitored using an array of techniques.

Chapter 8 (Device-level Testing and Results) — The functionality of the prototype is checked through the performance of various measurements. The Josephson effect is demonstrated. Measurements of critical current and normal state resistance are presented. The AC Josephson effect is observed through the generation of Shapiro steps. Critical current modulation is demonstrated in the presence of a magnetic field, and is found to be consistent with the intended 45° asymmetric grain boundary.

Chapter 9 (Conclusions and Recommendations) — Conclusions are drawn as to the success of this work. The relative strengths and weaknesses of the resulting process are discussed along with future recommendations for improvements and research possibilities.

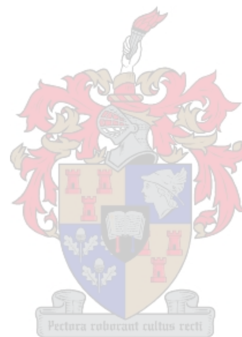

Chapter 2

Josephson Junctions

2.1 Introduction

The focus of this chapter will be on the electrical properties of the resistively shunted junction (RSJ) model. Although the discussion will be based on the superconducting tunnel junction prevalent in most low-T_c technologies, the model holds for many high-T_c grain boundary junctions and therefore provides an excellent tool for characterising these elements, as well as the design and simulation of circuits which contain them. The behaviour of the elements due to the application of various sources will also be presented briefly to illuminate discussions on testing in later chapters.

Josephson junctions and superconductors in general exhibit a multitude of fascinating properties, many with practical applications. However, an exhaustive overview of these topics is beyond the scope of this thesis. We will therefore restrict our discussion to the phenomena and mechanisms most relevant to our purpose. For a more complete introduction to this field, many excellent reference works are available [26, 34].

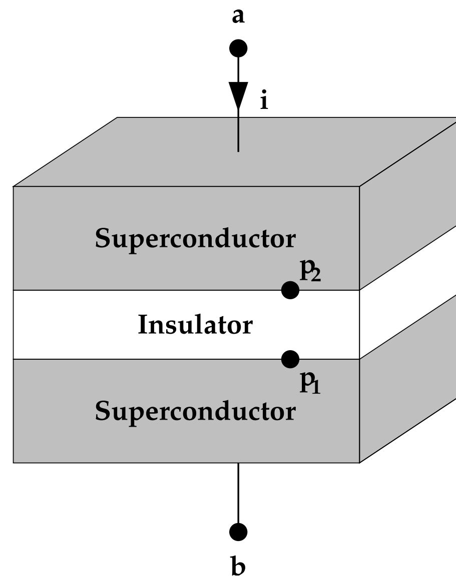

Figure 2.1: Structure of a tunnel junction

2.2 Superconducting Tunnel Junctions

The tunnel junction is perhaps the most basic of devices utilising the Josephson effect. The structure of the junction is incredibly simple, consisting of a sandwich structure of two superconducting layers with an insulating layer between them (see Figure 2.1).

2.3 Basic Lumped Junctions

Consider the simplest case where the contact areas of the superconducting electrodes with the insulator are small enough so that the current density across these surfaces can be considered uniform. Given this, the junction can be treated as a lumped device with terminal characteristics described by the total current supplied to the element.

It can be shown [26] that for a basic lumped junction, the terminal current is given by

$$i = I_c \sin \varphi(t) \tag{2.3.1}$$

where $\varphi(t)$ is the gauge-invariant phase difference between the two terminals defined as

$$\varphi(t) = \theta_1(t) - \theta_2(t) - \frac{2\pi}{\Phi_0}\int_1^2 \mathbf{A}(\mathbf{r}, t) \cdot d\mathbf{l}. \tag{2.3.2}$$

Here I_c is defined as the critical current of the junction, which is the maximum current that the basic lumped junction can carry. θ_n is the phase of the complex wavefunction $\Psi(\mathbf{r}, t)$ at the point p_n (defined in Figure 2.1). The line integral is along a contour connecting points p_1 and p_2, Φ_0 is the value of one flux quantum ($\frac{h}{2e}$) and $\mathbf{A}$ is the magnetic vector potential.

It can also be shown that the gauge-invariant phase difference is related to the terminal voltage by the equation

$$\frac{d\varphi}{dt} = \frac{2\pi}{\Phi_0} v. \tag{2.3.3}$$

2.4 Generalised Josephson Junctions

From (2.3.1), it is obvious that a basic lumped junction can only support a maximum current of I_c. The question now arises as to what happens when an actual Josephson junction is driven at currents greater than this value. The key observation to be kept in mind is that the current referred to in the equation is a supercurrent. It is therefore possible for a junction to support larger currents if recourse is taken to normal currents. We will now proceed to generalise basic junctions to allow for this.

The supercurrent referred to in (2.3.1) can persist without any applied voltage. Noting from (2.3.3) that the gauge-invariant phase difference remains constant at zero applied voltage, it is possible for the phase difference to remain at some arbitrary value for all time. This would of course imply a constant value of i in (2.3.1).

Supercurrents are carried by paired electrons called Cooper pairs. Persistent supercurrents between separated regions of superconductor are possible because Cooper pair tunnelling can occur without a net input of energy. However, for normal conduction this is no longer the case.

Normal conduction in the Josephson junction involves the tunnelling of normal electrons through the insulating barrier. There exist two prominent mechanisms by which normal electrons are produced for this purpose. The first is the breaking of Cooper pairs by thermal effects. The second is the breaking of Cooper pairs due to an energy input provided by an applied voltage.

Because the electrons in a Cooper pair are bound with an energy of Δ_0, an energy input of $2\Delta_0$ is required to break each pair. This implies that an applied voltage of $V_g = \frac{2\Delta_0}{e}$ (called the gap voltage) will be just enough to break the pairs [34].

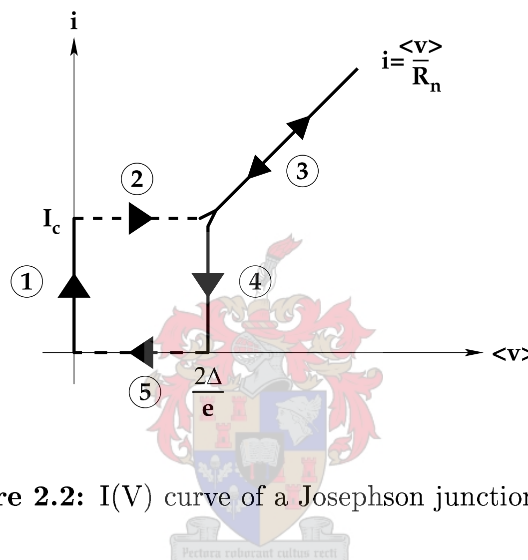

Figure 2.2: I(V) curve of a Josephson junction at 0K

Pectora roborant cultus recti

First consider the operation of an idealised junction at 0K as shown in Figure 2.2[1]. As the current through the junction is increased from zero, the voltage remains at zero along the line marked 1. This continues until the critical current is reached.

With the temperature at absolute zero and the assumption that the junction is perfectly fabricated, there are no normal electrons present at voltages below the gap voltage. Therefore, when the current in the junction goes above the critical value, Cooper pairs must be broken to generate electrons which can carry the excess current through normal conduction. The voltage across the junction jumps abruptly to the gap voltage because of this energy consumption. This transition is represented by the dashed line marked 2.

[1] Given a constant current driving source, the voltages referred to in Figures 2.2 and 2.3 are time averages. See Orlando and Delin [26] for more detail.

Further increase, and subsequent decrease, of current above the critical current is sustained through normal metal-to-metal tunnelling which can be modelled by a simple resistance. This resistance (R_n) is referred to as the normal state resistance. The I(V) curve follows the segment marked 3 in this region of operation.

When the current is decreased below the critical value, the voltage stays constant at the gap voltage until the current reaches zero, then jumps abruptly back to zero. This part of the I(V) curve is represented by the segments marked 4 and 5 respectively.

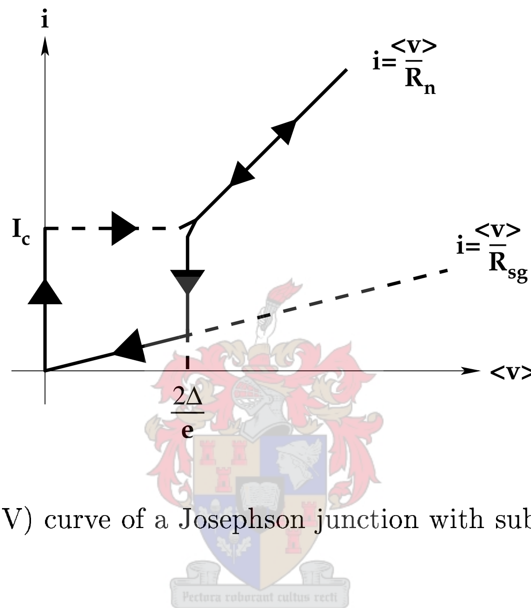

Figure 2.3: I(V) curve of a Josephson junction with sub-gap conduction

Pectora roborant cultus recti

When the temperature is non-zero, the situation changes slightly since there is the constant presence of normal electrons produced by thermal excitations. The return path from the normal to the superconducting state is modified as shown in Figure 2.3. Note that the bottom part of the curve now follows the line $i = \frac{v}{R_{sg}}$. R_{sg}, or the sub-gap resistance, represents the associated resistance of the energy loss due to the tunnelling of normal electrons at voltages below the gap voltage. Note that we have $R_n < R_{sg}$. This reflects the fact that fewer normal electrons are available below the gap voltage.

We observe that the generalised Josephson junction has a resistance which is dependent on the terminal voltage. This resistance is given by the expression

$$R_j(v) = \begin{cases} R_{sg} & 0 < v < V_g \\ R_n & v > V_g \end{cases} . \tag{2.4.1}$$

This resistance operates as a parallel conduction channel to the basic junction's supercurrent.

The product of the critical current and the normal state resistance, or the I_cR_n product, is an important parameter as it is closely tied to circuit performance. For RSFQ circuits, the maximum operating frequency is proportional to this value [34]. Therefore, for this important application, the I_cR_n product can be treated as a figure of merit for a given junction.

To complete the model, the junction capacitance needs to be taken into account. An approximate expression for this can be found from the fact that the junction structure is that of a parallel plate capacitor, giving

$$C_j \approx \frac{\epsilon_0 \epsilon_r A}{d} \tag{2.4.2}$$

where ϵ_0 is the permittivity of free space, ϵ_r is the relative permittivity of the dielectric, A is the junction area and d is the thickness of the dielectric.

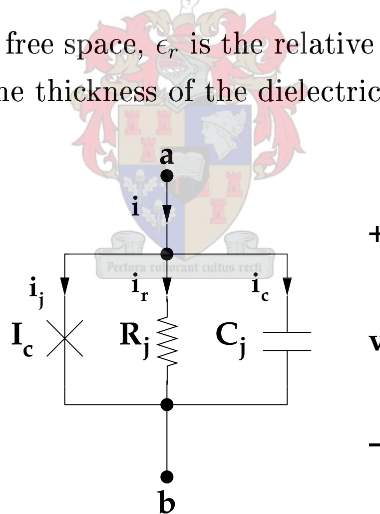

Figure 2.4: The generalised Josephson junction model

Figure 2.4 shows the schematic representation of the developed model. Note that the element on the left represents the basic lumped junction as discussed earlier. The resistor and the capacitor represent the junction resistance and capacitance as defined earlier in this section. The behaviour of this model under various conditions will now be considered.

2.5 Resistively Shunted Junctions

From Figure 2.4, Kirchoff's current law, (2.3.1) and (2.3.3), the differential equation governing the current in this system is given by

$$\begin{aligned} i &= i_j + i_r + i_c \\ &= I_c \sin\varphi + \frac{1}{R_j} v + C_j \frac{dv}{dt} \\ &= I_c \sin\varphi + \frac{1}{R_j} \frac{\Phi_0}{2\pi} \frac{d\varphi}{dt} + C_j \frac{\Phi_0}{2\pi} \frac{d^2\varphi}{dt^2}. \end{aligned} \tag{2.5.1}$$

Along with (2.3.3), this equation describes the time evolution of the system. A simplifying assumption for the analysis of this set of equations is to take $R_j = R_n$. The resulting model is referred to as the resistively shunted junction (RSJ) model [26]. In this section, the response of the RSJ model to the application of various sources will be discussed.

2.5.1 DC Excitation

The I(V) curve due to DC excitation has already been discussed. There is, however, the added complication of the effect of the junction capacitance, which has great influence on I(V) behaviour. The Stewart-McCumber parameter is a measure of the dominance of the capacitor dynamics in the RSJ model [26]. It is given by

$$\beta_c = \frac{2\pi I_c R_n^2 C}{\Phi_0}. \tag{2.5.2}$$

Figure 2.5 shows the behaviour of resistively shunted junctions as β is varied. In the limit were $\beta_c \ll 1$ (the overdamped limit), the capacitance is negligible and the I(V) behaviour is non-hysteretic as shown in the figure. Where $\beta_c \gg 1$ (the underdamped limit), the capacitance dominates and the curve becomes hysteretic.

High-T_c junctions appear to be internally shunted at 77 K [20]. Thus, their behaviour tends towards the region $\beta_c \ll 1$, usually exhibiting non-hysteretic I(V) curves. We therefore

expect to measure curves of this type during the later section on testing.

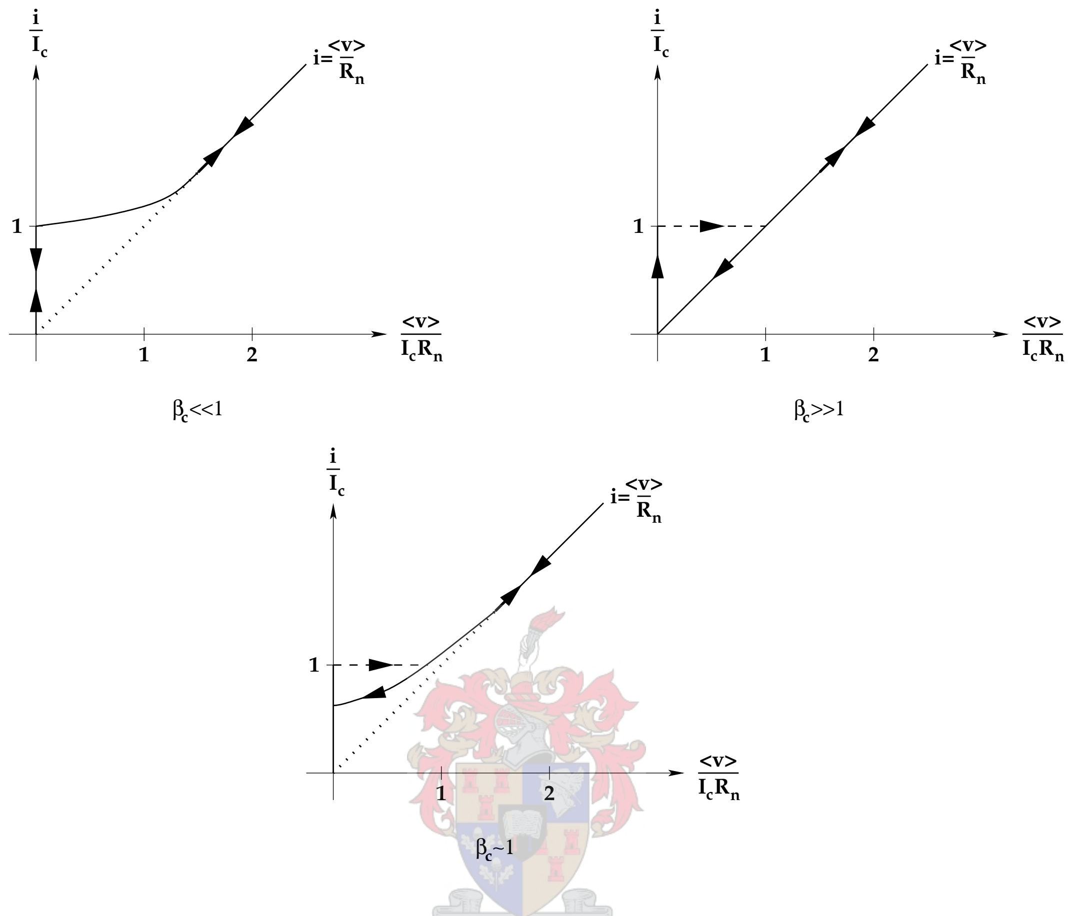

Figure 2.5: The influence of β_c in the RSJ model (adapted from [26])

2.5.2 AC Excitation

Application of high frequency power to a Josephson junction leads to an interesting phenomenon called the AC Josephson effect. The I(V) curve of a junction under these conditions shows stair-step features, with each step having a well defined height in terms of the frequency of the applied power.

First consider a basic lumped junction driven by an AC voltage source with a DC offset. The expression for the driving voltage is given by

$$v_J(t) = V_0 + V_s \cos \omega_s t. \tag{2.5.3}$$

It can be shown that the current response of the junction can be expressed in terms of the infinite series

$$i_J(t) = I_c \sum_{n=-\infty}^{\infty} (-1)^n \left[J_n \left(\frac{2\pi V_s}{\Phi_0 \omega_s} \right) \right] \sin \left[\left(2\pi \frac{V_0}{\Phi_0} - n\omega_s \right) t + \varphi(0) \right] \tag{2.5.4}$$

where $\varphi(0)$ is the gauge invariant phase difference at $t = 0$ and J_n is the nth order Bessel function of the first kind [26]. The average current can be found by observing that the averages of the sinusoids are zero except in the case where the coefficient of t is zero. This occurs when

$$V_0 = n \frac{\Phi_0}{2\pi} \omega_s. \tag{2.5.5}$$

Given an arbitrary $\varphi(0)$, the average current obeys

$$|\langle i_J(t) \rangle| \leq I_c J_n \left(\frac{2\pi V_s}{\Phi_0 \omega_s} \right). \tag{2.5.6}$$

Consider the same scenario, but with a resistively shunted junction. Assuming $\beta_c \ll 1$ (as is the case for most high-T$_c$ junctions), we have a negligible junction capacitance. The RSJ model thus only requires the addition of a resistance R_n to the basic lumped junction. Since the voltage across the elements is given, the average current is given by

$$\langle i(t) \rangle = \langle i_J(t) \rangle + \frac{\langle v_J(t) \rangle}{R_n} = \langle i_J(t) \rangle + \frac{V_0}{R_n}. \tag{2.5.7}$$

Thus, the addition of the resistor leads to an augmentation of the average current by the average current through the resistor. A series of current "spikes", produced by the basic lumped junction at voltages given by (2.5.5), is superimposed on this ohmic component.

Pectora roborant cultus recti

The spike amplitudes are given by (2.5.6). Figure 2.6 illustrates this resulting average current.

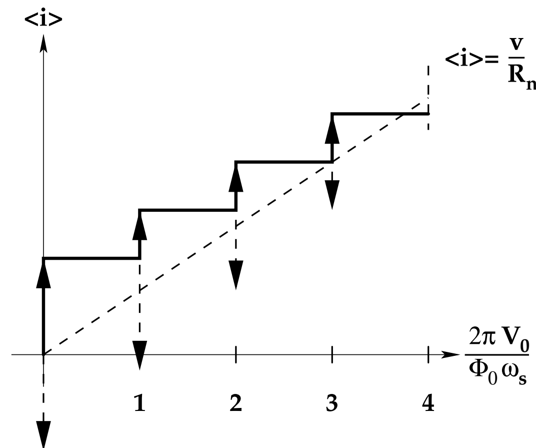

Figure 2.6: The AC Josephson effect (adapted from [26])

As the average current increases from zero, the curve follows the first current spike until the current which the basic lumped junction must carry would violate (2.5.6). At this point the junction switches to the next spike, causing a step in the voltage. This continues as the average current is swept upwards, producing the stair-step curve shown by the solid line (note that the horizontal portions of the curve are not part of the solution, but are present in practical measurements). These steps are referred to as Shapiro steps.

It is important to note that the voltages at which the steps occur (given by (2.5.5)) are determined only by the driving frequency and fundamental constants. This unique phenomenon is exploited in Josephson voltage standards to produce very accurate reference voltage sources.

The AC Josephson effect provides unambiguous evidence of the presence of Josephson junctions. This will be used to prove the functioning of the production device in the section on testing.

2.6 Magnetic Field Effects

The presence of an uniform magnetic field threading the junction has the effect of suppressing the critical current. This is caused by a linear gradient in the gauge invariant phase difference induced by the magnetic field. From (2.3.1), we know that a linear gradient in φ will cause an oscillating supercurrent along the junction interface. Since the supercurrent is no longer uniform, but sinusoidally modulated in space, the total supercurrent is less. This leads to a reduction of the critical current.

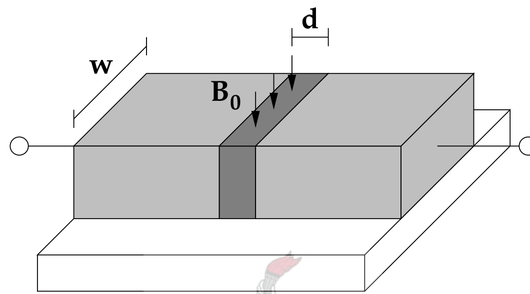

Figure 2.7: Geometry for critical current modulation

Suppose that the applied field has a uniform flux density B_0. The field enters the insulator as shown in Figure 2.7. The total flux Φ_I in the insulator is given by wdB_0. However, the magnetic field penetrates into the superconducting electrodes to an effective depth of λ (the penetration depth) resulting in an effective barrier thickness d' of $d + 2\lambda$. Thus the total flux treading the junction is given by

$$\Phi_J = w(d + 2\lambda)B_0. \tag{2.6.1}$$

To simplify the analysis, we neglect the self-fields produced by the tunnelling current. This is called the short junction approximation which is valid when $w < \sqrt{\frac{\pi\Phi_0}{\mu_0 J_c d'}}$. It can shown that for short junctions the critical current can be expressed as [26]

$$i_{max}(\Phi_J) = I_c \left| \frac{\sin \frac{\pi\Phi_J}{\Phi_0}}{\frac{\pi\Phi_J}{\Phi_0}} \right|. \tag{2.6.2}$$

Figure 2.8 illustrates the behaviour of (2.6.2). Many Josephson junctions exhibit this type of modulation, which is often referred to as Fraunhofer modulation. However, this is not the case for asymmetric 45° grain boundary junctions (which will be fabricated in this work). These deviations will be used as evidence for the success of the process in Chapter 8.

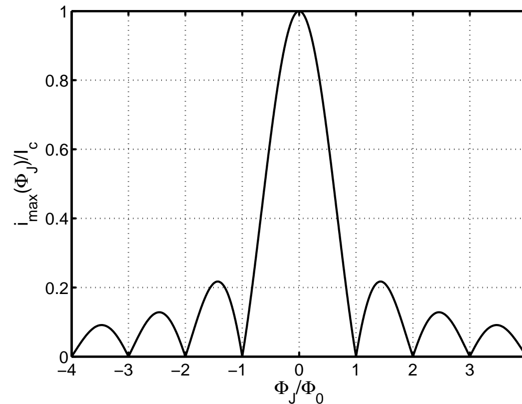

Figure 2.8: Critical current of a short junction in a magnetic field

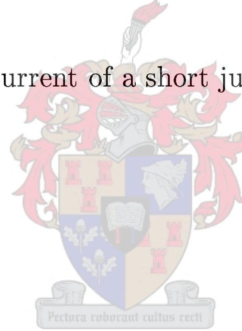

2.7 Summary

The basic electrical properties of Josephson junctions have been reviewed. The resistively shunted junction model has been presented, providing an understanding of key junction parameters. Terminal behaviour under the application of DC and AC sources has been discussed, along with the effects of an applied magnetic field. This knowledge will be applied in Chapter 8 to verify the Josephson effect and to characterise the junctions.

Chapter 3

High-T_c Josephson Junctions

3.1 Introduction

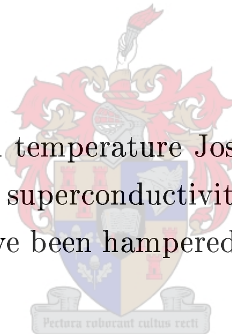
Pectora roborant cultus recti

The development of improved high temperature Josephson junction fabrication technologies remains a focus of the high-T_c superconductivity community. To date efforts towards the creation of complex circuits have been hampered by difficulties in attaining reasonable reproducibility and performance.

In this chapter we will begin by discussing the unique challenges that high-T_c materials pose in the creation of usable Josephson junctions. An overview of the various types of high-T_c junctions will be provided, with the focus being on the grain boundary junction. The most popular ways in which grain boundary junctions are manufactured will be discussed. We will then review the previous work done on grain boundary junctions at the University of Stellenbosch, followed by a detailed discussion of the chosen fabrication method, bi-epitaxy.

3.2 High-T_c Specific Issues

The difficulties encountered in high-T_c device manufacture stem from several factors. Firstly, high-T_c superconductors are structurally more complex than low-T_c varieties.

While popular low-T$_c$ superconductors are generally composed of single elements (e.g. Niobium) or simple alloys, high-T$_c$ superconductors tend to be composed of many elements with complex unit cell arrangements. This makes these materials correspondingly harder to deposit and process.

Furthermore, in a high-T$_c$ superconductor, imperfections on the scale of only one unit cell can disturb the transport properties due to the very short coherence lengths inherent in these materials ($\xi_{ab} = 1.5\,\mathrm{nm}$ and ξ_c between 0.3 and 0.5 nm for YBCO [31]), while similar defects in low-T$_c$ materials have little influence on overall behaviour. This sensitivity to lattice disorder leads to the requirement that high-T$_c$ thin films need to be grown so that uncontrolled deviations from single crystallinity are avoided as much as possible. This requires the use of well-matched single-crystal substrates on which epitaxial growth can occur.

3.3 High-T$_c$ Junction Types

The unique characteristics of high temperature superconductors have led to the development of a wide variety of junction configurations, many of which are entirely novel. A quick overview of the major junction types will now be given.

Pectora roborant cultus recti

3.3.1 Extrinsic Junctions

Extrinsic junctions are formed where two closely spaced superconducting electrodes (abbreviated S) are separated by some non-superconducting interlayer. This interlayer can be an insulator (I), a semiconductor (Se), a normal metal (N) or a superconductor above its critical temperature (S'). The junction classification is obtained by concatenating the abbreviations of the layers composing the junction. For example, a planar sandwich type junction as discussed in the previous chapter is classified as SIS [12].

Various configurations of extrinsic junctions exist, some of which are shown in Figure 3.1. Although these types of junctions have had great success in low-T$_c$ applications, the short coherence lengths in high-T$_c$ materials are problematic due to the rapid depression of the

superconducting order parameter in the non-superconducting interlayer. Therefore, this layer is required to be extremely uniform and thin if it is to serve as a suitable barrier. This makes the reproducible manufacture of these devices difficult.

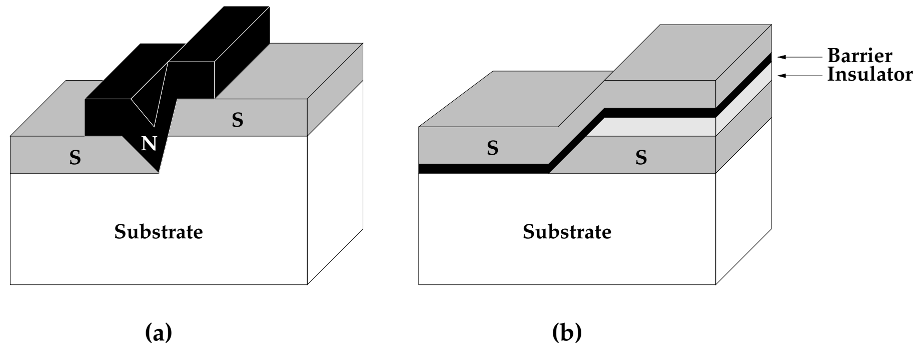

Figure 3.1: Extrinsic junctions: (a) Step-edge SNS (b) Ramp-edge (adapted from [20])

3.3.2 Intrinsic Junctions

Intrinsic junctions are junctions which make use of the inherent properties of the superconductor in order to form a weak link. For high-T_c junctions, these can be divided into microbridges and grain boundary junctions. Although microbridges are known in low-T_c technologies, the grain boundary junction is unique to high-T_c materials.

Microbridges are created by forming constrictions in lines of superconducting material. It can be shown that, if the constriction is narrow and short enough, a weak link is formed [26]. This is illustrated in Figure 3.2(a).

High-T_c superconductors consist of layered structures in which the CuO planes act as the primary transport channels. Inter-plane coupling is much weaker than intra-plane coupling and can, for materials such as Bi-2212, be understood as interlayer Josephson junctions. A class of junctions exists which takes advantage of this intrinsic Josephson effect. The resulting devices may be modelled as serially stacked Josephson junctions [41]. Figure 3.2(b) shows one such junction configuration. The superconductor is shown as being composed of layered unit cell stacks. Over the step, the supercurrent is forced to tunnel vertically along the c-axis, leading to observation of the Josephson effect.

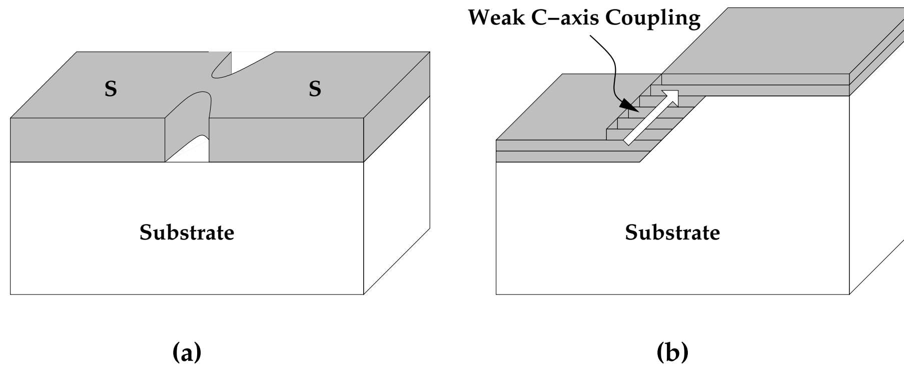

Figure 3.2: Intrinsic junctions: (a) Microbridge (b) C-Axis coupling step

3.4 Grain Boundaries

In the study of materials, grains can be defined as single crystal regions within a given material. Grain boundaries are formed where two grains meet. The short coherence lengths and highly anisotropic transport properties of high temperature superconductors ensure that (given sufficient misalignment of the neighbouring grains) weak links are formed across such boundaries in the material. Grain boundary junctions represent a popular class of high-T_c junctions of which bi-epitaxial junctions form a part. As such, an overview of grain boundary junctions will now be given to provide the needed background.

3.4.1 Grain Boundary Types

Grain boundaries are defined by the way in which the relevant neighbouring grains are misaligned. Translational grain boundaries are boundaries where the lattices in the neighbouring grains are of the same orientation, but translated relative to each other. Rotational grain boundaries, which are of primary interest to us, occur where the orientation of the two grains differ. One can distinguish between two types of rotational grain boundaries: tilt boundaries and twist boundaries [14]. Figure 3.3 illustrates the different boundary types.

The boundary type depends on the orientation of the axis of rotation relative to the grain boundary. Tilt boundaries occur where the axis of rotation lies within the grain boundary

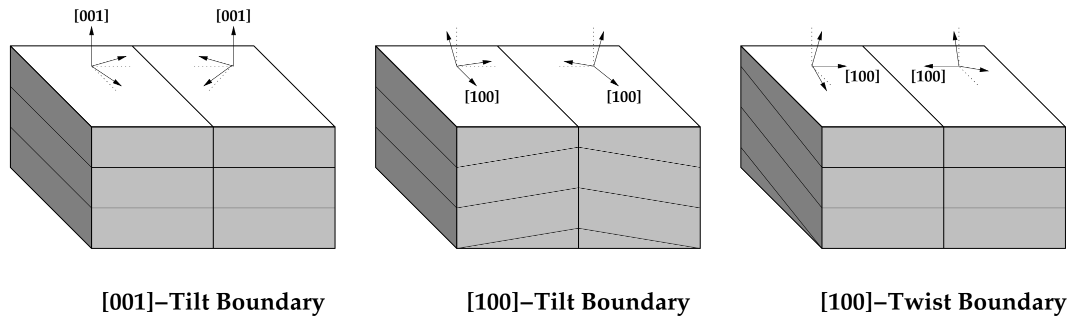

Figure 3.3: Grain boundary types (adapted from [14])

plane, whereas twist boundaries have rotational axes perpendicular to the grain boundary plane. Boundaries that contain both kinds of rotation are referred to as mixed boundaries.

Apart from the rotation angle, we must also specify the rotational axis. A specific crystallographic axis such as the c-axis ([001]) is chosen to be collinear with the rotational axis.

A further important characteristic is the symmetry of the grain boundary. In a symmetric grain boundary, both grains are rotated relative to the boundary in the same way. For an asymmetric boundary, the angles of rotation are different.

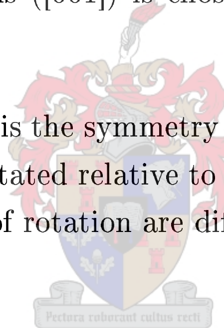

3.5 Engineered Grain Boundaries

In order to reliably exploit the properties of YBCO grain boundaries, we must be able to induce their formation in a controlled way. Several techniques have emerged to fulfil this need: bicrystals, step-edges and bi-epitaxy. We will now discuss each of these techniques in turn along with their relative strengths and weaknesses.

3.5.1 Bicrystal junctions

Bicrystal technology is based on the simple idea of creating an artificial grain boundary by fusing together two differently oriented single crystal substrates to create a new sub-

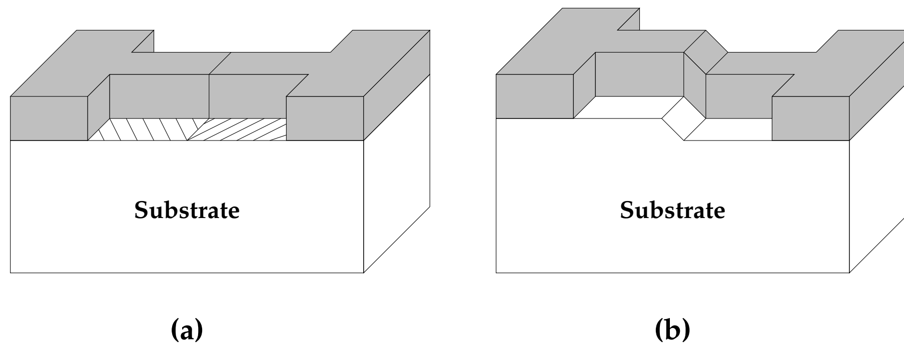

Figure 3.4: Grain boundary junctions: (a) Bicrystal (b) Step-edge

strate. A superconducting thin film can then be deposited onto this substrate resulting in a grain boundary along the line where the separate substrates were fused together. Figure 3.4(a) depicts this situation (the diagonal lines on the substrate surface indicate the local crystallographic orientation of the substrate).

Bicrystals hold the advantage that one is free to choose the grain orientations on both sides of the boundary. This freedom has allowed researchers to study the transport properties across boundaries with well defined misorientations. The process is also reliable and reasonably straightforward given the correct equipment to manufacture the substrates.

The disadvantage of bicrystal technology is that one cannot place junctions at arbitrary locations on substrate. Generally, there is only a single grain boundary present running down the middle of the substrate. The amount of junctions that one can place on the substrate is limited, restricting the complexity of circuits which can be implemented successfully. Ready-made bicrystal substrates and layers are also prohibitively expensive, allowing very little room for experimentation.

3.5.2 Step-edge Junctions

Step-edge junctions are formed by depositing YBCO onto substrates into which steps have been etched. Depending on the step angle and the sharpness of the corners, grain boundaries form along the top and/or bottom edges of the step. This is illustrated by Figure 3.4(b).

The step angle is the key process parameter, as it determines the microstructure of the resulting YBCO film which covers the step. The step height also has to be sufficient, generally this is on the order of the thickness of the YBCO thin film [14].

The type of grain boundary formed depends on the substrate material. For example, on MgO, YBCO tends to grow with its [001]-axis normal to the local substrate surface, leading to the formation of [100]-tilt boundaries. In contrast, YBCO grown on steps in $SrTiO_3$ forms only 90° grain boundaries [14].

Step-edge junctions allow the arbitrary placement of grain boundaries, removing one of the great restrictions of bicrystal technologies while still allowing variation of the grain boundary angle (given the right choice of substrate). However, manufacturing these steps requires a well characterised etch process. Since the step angle is dependent on many parameters which are hard to keep constant (such at the photoresist sidewall angle), parameter spreads tend to be larger than for bicrystal junctions. Nevertheless, step-edge junctions show good transport properties and are popular in the high-T_c junction fabrication community.

3.5.3 Bi-epitaxial Grain Boundaries

Pectora roborant cultus recti

Bi-epitaxial grain boundaries are fabricated by controlling the in-plane orientation of YBCO thin-films to form 45° [001]-tilt grain boundaries along edges defined by photolithography. This control of the in-plane orientation can be achieved by exploiting the property of certain combinations of thin-films where one layer deposited on the other grows with an a-b plane orientation which is offset by 45° relative to that of the bottom layer. Figure 3.5 shows a generalised schematic for this type of junction. Bi-epitaxial junctions were first fabricated at Conductus Inc. by Char *et al* [4] in 1991, leading to the first commercial product featuring high-T_c Josephson junctions, a SQUID magnetometer [17].

There are clear advantages to this process. Firstly, as with step-edge junctions, junctions can be placed at arbitrary locations on the substrate. Secondly, although one cannot arbitrarily choose the grain boundary angle, one is guaranteed that the angle will be 45°. Thirdly, it is possible to extend the process to multi-layer circuits.

There are some disadvantages to the process though. As we have just mentioned, the

grain boundary angle is fixed at 45°. Since this value is not optimal, the I_cR_n products of bi-epitaxial junctions are generally lower than their bicrystal and step-edge counterparts. However, the simplicity of the process still makes it very attractive.

3.6 Review of Previous Work

Given the preceding overview of high-T_c junction fabrication technology, we are now in a position to discuss the history and state of research at the University of Stellenbosch before the start of this work. Several researchers have attempted to create Josephson junctions using YBCO thin films. Even though they were not successful, the techniques that were developed and employed by these workers serve as a foundation for the efforts outlined in this thesis. We will quickly discuss the contributions and methodologies of the various researchers. A justification for the direction taken by the author is then given based on this prior work.

Most of the previous research (with the exception of Snetler) has focused on the creation of DC SQUIDs. In order to achieve these ends several approaches have been tried.

In previous work, all thin-films were deposited using PLD. Rottier [30] performed the optimisation of the process for YBCO, achieving good results. This work was used by Knox-Davies [19] and Graser [11] to deposit their thin-films. Graser included a helical shadow mask in his work. This decreased the surface roughness, but at the price of an uneven deposition.

Initial attempts at fabrication centred around the bicrystal technology. The principal researchers following this route were Conradie, Knox-Davies and Graser. Conradie [9] attempted the manufacture of a DC SQUID. In his work, he made use of ready-made bicrystal substrates, onto which he deposited YBCO using PLD. Knox-Davies [19] attempted to manufacture a high-T_c DC SQUID gradiometer using a method similar to that of Conradie. Graser [11] also attempted to create a SQUID magnetometer. In his final fabrication runs he made use of a commercial bicrystal substrate with a pre-deposited layer of YBCO.

Conradie performed a single fabrication run. Tests performed on his device revealed no trace of the Josephson effect. Indeed, it is unclear whether superconductivity was present in the device.

Knox-Davies performed two fabrication runs, none of which was successful (one sample showed flux-flow behaviour, whereas the second showed no superconductivity). The failures of the first and second devices were respectively attributed to poor substrate quality (the first substrate was recycled) and poor thin film growth (the YBCO of the second sample showed cracking).

Graser's device failed to show any signs of superconductivity. He attributed this to loss of oxygen during high temperature processing, or to surface degradation of the YBCO leading to poor electrical contact with the contact pads.

Snetler [32] attempted to make substrate steps suitable for step-edge fabrication. Development centred around the improvement of an argon-ion mill. The resulting step-edges were poor, with step angles of less than 7°. These angles are too low for the resulting grain boundary to function as a weak link.

These results were attributed to the poor photoresist sidewall angles. In one case, they were only 6°. Later optimisation of the resist angles showed that this is not the primary problem, since even modest substrate step angles of 10° were still not easily obtainable for MgO. It is thought that the most likely explanation is that the substrate is a dielectric which charges up due to the influx of positively charged argon ions. This charging effect could lead to a change in the way material is sputtered from the surface. The etch rate of the resist is also much faster than that of the substrate and this strongly limits the maximum angle that can be achieved [22].

At the commencement of the work performed in this thesis, consideration was given to these past results and how best to extend them in order to produce working Josephson junctions. The experiences with the bicrystal method showed that, although potentially viable given the state of the PLD process, the substrates are simply too expensive for experimentation. Therefore, only methods which can utilise cheaper substrates were considered. The lack of an adequate milling process precluded the manufacturing of step-edges. It however remains an open question whether the existing milling equipment can be sufficiently improved

towards this end.

Bi-epitaxy was selected as the fabrication method for two reasons. Firstly, a PLD process with demonstrable success was available. Since PLD can also be used for the deposition of the dielectric materials required by bi-epitaxy, this part of the manufacturing process seemed workable. Also, although the milling process has difficulty etching dielectrics, it should be remembered that the dielectric layers in bi-epitaxial devices are extremely thin (less than 40 nm). The milling process available at the time could easily etch these thicknesses. Furthermore, the poor step angles are not necessarily disadvantageous since, in general, one wants to avoid the creation of undesired step-edge junctions. Given these facts, bi-epitaxy was seen as a feasible alternative route for making Josephson junctions and was therefore made the topic of this thesis.

3.7 Bi-epitaxial Junctions

3.7.1 Background

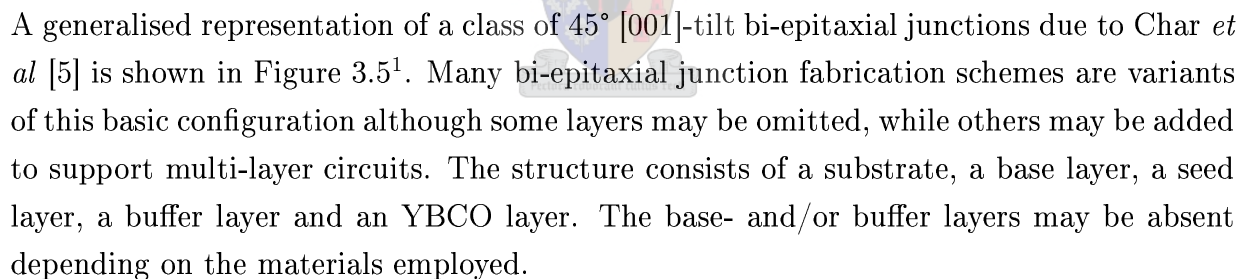

A generalised representation of a class of 45° [001]-tilt bi-epitaxial junctions due to Char *et al* [5] is shown in Figure 3.5[1]. Many bi-epitaxial junction fabrication schemes are variants of this basic configuration although some layers may be omitted, while others may be added to support multi-layer circuits. The structure consists of a substrate, a base layer, a seed layer, a buffer layer and an YBCO layer. The base- and/or buffer layers may be absent depending on the materials employed.

The function of the base layer is simply to act as a substrate material for the epitaxial growth of the seed- and buffer layers. For the rest of the discussion, the terms substrate and base layer are treated as interchangeable in cases where a separate base layer is not present. A base layer is usually employed when there is a need to use the same set of materials on different substrates. As long as good epitaxial growth of the correct orientation can be achieved for a given base layer, an arbitrary substrate material may be chosen. This allows

[1]Note that the diagrammatic representations of device structures and fabrication processes are not to scale, usually overemphasising the size of the seed and buffer layers. In real bi-epitaxial junctions, these layers are usually very thin to avoid the accidental creation of undesired step-edge junctions.

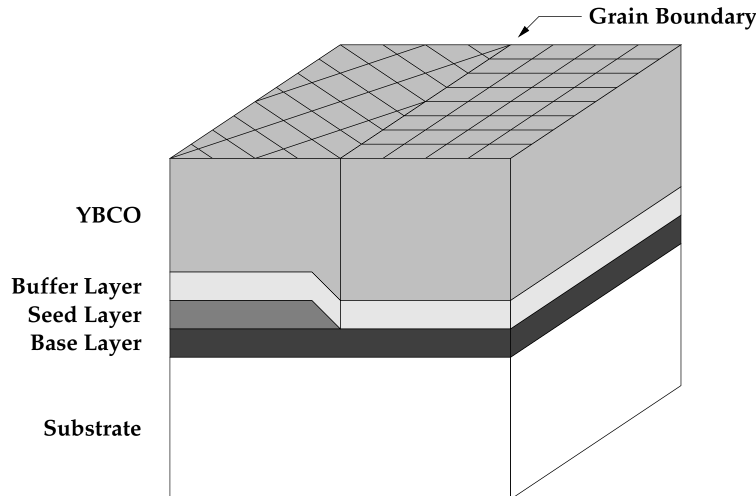

Figure 3.5: Generalised bi-epitaxial junction structure

one to employ substrates with different electrical characteristics for different applications or to use cheaper substrates to the same effect as one would use single crystal substrates of the base layer material.

As with any of the layers, the seed layer acts as template for the epitaxial growth of the next layer (which can be the buffer layer or, in its absence, YBCO). However, the seed layer is chosen so that the next layer grows with a different crystallographic orientation to that of the growth directly on the base layer. In the case depicted in the figure, a 45° [001]-tilt grain boundary forms along the line separating the seed layer and the uncovered base layer.

The buffer layer, if it is present, functions along with the seed layer as just described to achieve the required 45° in-plane rotation. It may also be used to improve the quality of the deposited YBCO layer, examples being cases where there is a chemical incompatibility between the YBCO and the bottom layers, or where there is a large lattice mismatch between the YBCO and the bottom layers which must be corrected.

The choice of base layer, seed layer and buffer layer, therefore, depends critically on the growth relationships at the interfaces between the layers in the structure. Wu *et al* [38] performed a systematic study of the growth relationships between various oxides and YBCO. Their results for the oxides used in this thesis are summarised in Table 3.1.

Bottom layer Lattice constant	CeO_2 5.41Å	MgO 4.21Å	YSZ 5.14Å
Top layer			
CeO_2	0°	0°[1]	0°
YSZ	0°	0°	0°
YBCO	45°	0°[2]	45°[3]

1. There is always a 45° component present (at least 5% according to [21]).
2. Some 45° rotated YBCO grains can be observed depending on deposition conditions and the substrate surface.
3. A simple cubic-to-cubic match (0°) can be found at low deposition temperatures.

Table 3.1: Selected results for in-plane epitaxial relationships according to Wu *et al* [38]

3.7.2 Single Seed Layer Approach

It would be appealing from a practical standpoint to minimise the amount of layers in the structure. This would have the obvious benefit of simplifying the manufacturing process, making it more amenable to research and subsequent production runs.

The minimal configuration for a bi-epitaxial junction includes only three layers: the substrate, the seed layer and the YBCO layer itself. One such minimalist configuration using MgO as a substrate and CeO_2 as a seed layer has been explored by various groups [21, 28, 40]. The structure employed by these groups is shown in Figure 3.6.

Referring to Table 3.1, we see that YBCO grows on CeO_2 with an in-plane rotation of 45°, while YBCO grows on MgO with a simple cubic-to-cubic match. Since CeO_2 grows on MgO with a simple cubic-to-cubic match as well, we expect that the YBCO grown on the seed layer will be rotated by 45° in the a-b plane relative to the YBCO grown directly on the substrate. This causes the formation of a 45° [001]-tilt grain boundary along the line separating the two regions. Note that the symmetry of the grain boundary depends on the direction of this line in the a-b plane.

Also note from the table that, for CeO_2 deposited directly on MgO, a small percentage of

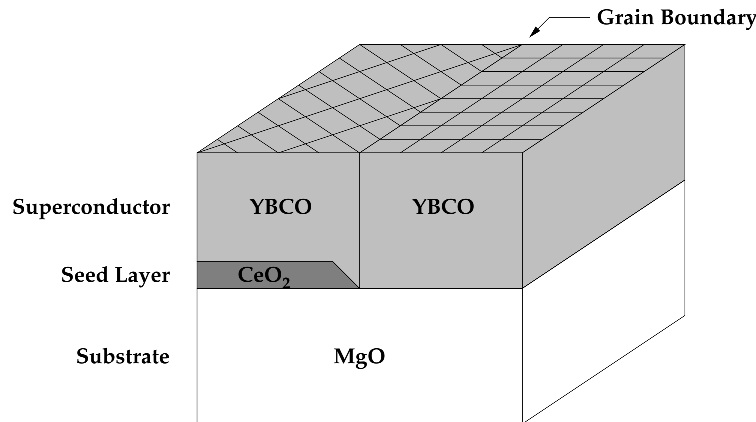

Figure 3.6: Bi-epitaxy using only a seed layer

the layer is always 45° oriented. To address this problem, Li *et al* [21] proposed the use of an yttria stabilised zirconium (YSZ) buffer layer underneath the CeO_2 as part of the seed layer structure. As such, the use of YSZ as a buffer layer for CeO_2 will also be investigated in this work.

3.7.3 Fabrication

Given the obvious simplicity of the single seed layer approach, it is ideal for performing initial investigation into the feasibility of the local fabrication of bi-epitaxial junctions. As such, junctions similar to those manufactured by Petersen *et al* [28] will be made during the course of this thesis.

The manufacturing process for this configuration is quite simple. The method involves only two deposition steps (excluding the contact pad metallisation) and two etch steps. It consists of the intuitively obvious procedure outlined in Figure 3.7.

The process starts with the deposition of a seed layer of [100]-oriented CeO_2 onto the MgO substrate. This layer is then patterned by selectively removing areas of the CeO_2 so that the desired grain boundary lines are defined by the edges of these regions. A layer of [001]-oriented YBCO is now deposited on the sample, growing with in-plane orientations as discussed previously. The circuit and junctions are then defined by another etch process which removes undesired regions of YBCO. This is followed by contact pad metallisation.

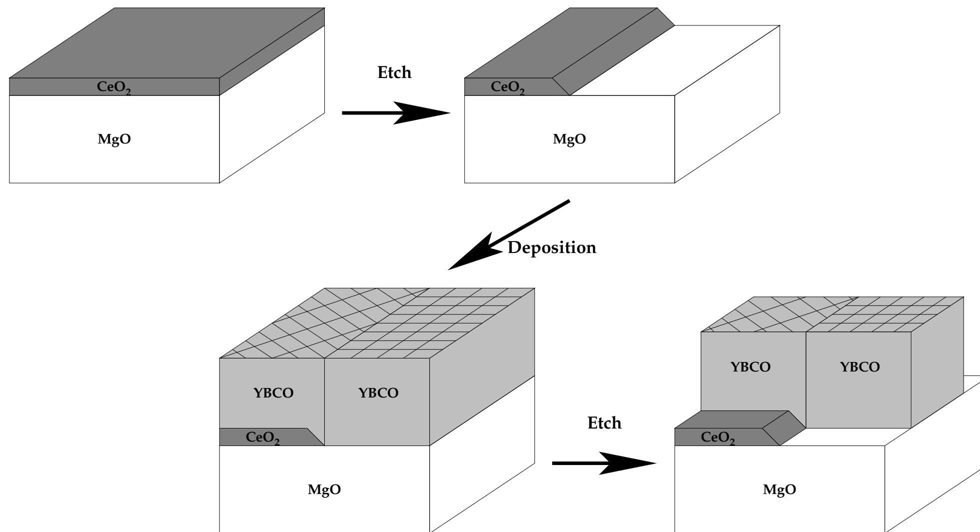

Figure 3.7: Direct method for CeO_2-based junction fabrication

3.8 Summary

In this chapter, an overview of high-T_c Josephson junctions was given. Different types of grain boundary junctions were presented and discussed. Previous work done towards the fabrication of grain boundary junctions at the University of Stellenbosch was reviewed. Given the state of local research at the time and the lack of success exhibited by the other approaches, bi-epitaxy was selected as the fabrication process to be explored in this thesis. The general structure of bi-epitaxial junctions was discussed. A single seed layer approach which utilises CeO_2 as the seed layer was selected as a good candidate for testing the feasibility of manufacturing these devices locally. A conceptual overview the fabrication process was then presented.

Pectora roborant cultus recti

Chapter 4

Crystal Orientation in Thin-Films

4.1 Introduction

The bi-epitaxy method depends critically on the seed layer cristallinity. Specifically, the seed layer must be epitaxial and of the correct crystallographic orientation. This chapter provides an overview of the concepts of epitaxy and texturing in thin-films. X-ray powder diffraction is identified as a way of performing the required tests for epitaxy. The fundamentals of the process are covered. Special attention is given to the seed layer materials CeO_2 and YSZ for the purposes of clarifying the data obtained in later chapters.

4.2 Texturing in Thin-Films

Texture, also know as preferred orientation, is the tendency for certain grain orientations to be favoured in a material. Texturing of materials can occur during crystallisation or at a later stage through thermo-mechanical processes [29].

The study of the texture of thin-films is critical for high-T_c superconductors as this strongly influences their transport properties [14]. Indeed, as we have discussed previously, grain boundary junctions are created by controlling grain orientations within a superconducting

thin-film. This is equivalent to controlling the texture of the layer.

In this section, we will discuss the two forms of texturing we will encounter during the course of this thesis: epitaxial growth and in-plane texturing.

4.2.1 Epitaxial growth

Epitaxial growth is a special case of texturing where the orientation of a single crystallographic axis in all the grains of a given film is determined by the substrate. This can occur when the substrate is well matched to the crystal structure of the depositing layer.

In defining the epitaxial relationship between a thin-film and a substrate, we must provide the orientation of both the substrate and the thin-film. The substrate orientation is usually given by specifying the lattice plane in the substrate material which is co-planar with the substrate surface. Thus, when the a-axis of an MgO substrate is normal to the substrate, we refer to the substrate as (100)-oriented. Similarly, the orientation of the thin-film is defined in terms of the substrate surface. For example, growth which leaves the c-axis of the thin-film normal to the substrate surface is referred to as (001)-growth.

In general, we want to distinguish between epitaxy and in-plane texture (which deals with the orientation of grains within planes parallel to the substrate surface). The only degree of freedom left for the grains in an epitaxial film is their in-plane orientation.

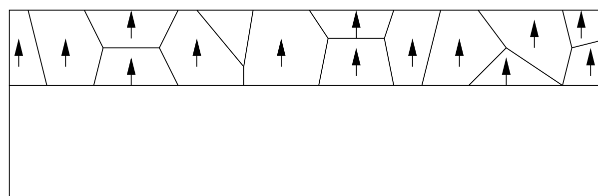

Figure 4.1: Epitaxial thin-film

4.2.2 In-plane Texturing

Epitaxial growth only defines the direction of a particular crystallographic axis in the thin-film lattice, leaving the grains free to rotate about this axis. In-plane texturing refers to the case where there is also preferred orientation in this degree of freedom. The in-plane orientation of a grain can be set by specifying two co-linear in-plane crystallographic axes, one from each material in the relationship. For example CeO_2[110]||MgO[100] indicates that the CeO_2 grows on the MgO with its [110]-axis parallel to the [100]-axis of the MgO.

Figures 4.2 and 4.3 depict examples of untextured and textured films respectively. The arrows indicate the direction of a specific crystallographic axis within each of the grains. In the untextured film the grain orientations are entirely random, while in the textured film depicted there are two grain orientations present.

As with epitaxial growth, at the correct deposition conditions, certain in-plane orientations are energetically more favorable than others. This allows us to grow entire sections of thin-film with the same in-plane texture, making the engineering of grain boundaries possible.

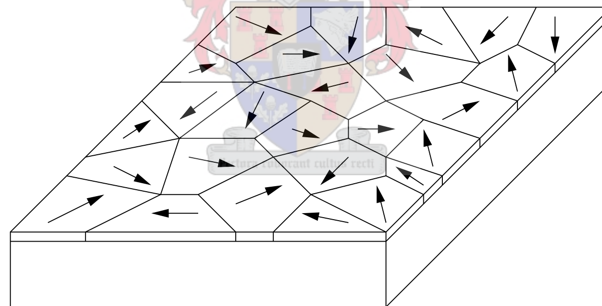

Figure 4.2: Thin-film with no in-plane texturing

4.3 Overview of Powder Diffraction

Powder diffraction is a simple yet powerful tool for characterising thin films. By using X-rays of a constant wavelength, it is possible to verify epitaxial growth and to determine exactly which grain orientations have grown epitaxially in a given layer. This allows us to

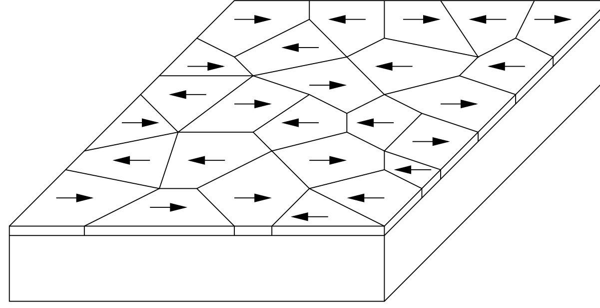

Figure 4.3: Thin-film with in-plane texturing

differentiate, for example, between a-axis and c-axis growth in YBCO thin-films. One can also determine whether the correct phase of the material has grown. We will now outline the technique and apply it to the characterisation of the seed layer materials CeO_2 and YSZ.

4.3.1 Lattice Planes

For any regular crystal lattice, we can construct sets of regularly spaced lattice planes [16]. To distinguish different sets of planes, we can assign each a set of unique indices. Consider the plane passing closest to the origin (though not the plane passing through the origin). For an orthorhombic system[1] we can construct the plane equation which describes it

$$1 = \frac{x}{x_0} + \frac{y}{y_0} + \frac{z}{z_0} \tag{4.3.1}$$

$$1 = h\frac{x}{a} + k\frac{y}{b} + l\frac{z}{c}. \tag{4.3.2}$$

Here a, b and c are the lattice constants and x_0, y_0 and z_0 are the x, y and z intercepts of the plane. We now refer to the tuplet (hkl) as the Miller indices (also known as hkl-indices) for the given set of planes. Negative indices are indicated by a bar above the index (e.g. $(1\bar{2}1)$).

[1]Since only orthorhombic lattices are considered in this text, we make this simplification for sake of argument. The definition is easily extended to non-orthorhombic systems.

To illustrate the preceding definitions, refer to Figure 4.4. In this two-dimensional example, we can see that the line closest to the origin has intercepts $\frac{a}{3}$ and $\frac{b}{2}$ on the x- and y-axis respectively. Therefore we have $h = 3$ and $k = 2$, making (32) the associated Miller indices.

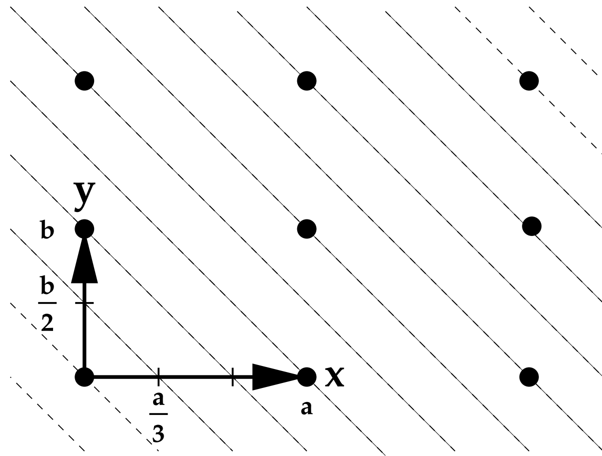

Figure 4.4: Two-dimensional example of Miller indices (adapted from [16])

To indicate a direction within the lattice we can rewrite a vector of the form $\mathbf{r} = u\mathbf{a}+v\mathbf{b}+w\mathbf{c}$ as [uvw].

The distance between successive planes with a given set of Miller indices can be easily calculated using the expression (for the orthorhombic case)

$$\frac{1}{d^2} = \frac{h^2}{a^2} + \frac{k^2}{b^2} + \frac{l^2}{c^2}. \tag{4.3.3}$$

4.3.2 Bragg Diffraction

A set Miller index tuplets can be converted into a set of distances characteristic of the material in question. This can be used to verify the presence of the material by checking for these "signature" inter-plane distances in the sample. To do this, we can make use of an X-ray powder diffractometer. The operation of powder diffractometers rests on Bragg's law, which is discussed in this section.

Consider a set of regularly spaced lattice planes as shown in Figure 4.5. We would like to determine the separation distance d between them using X-rays.

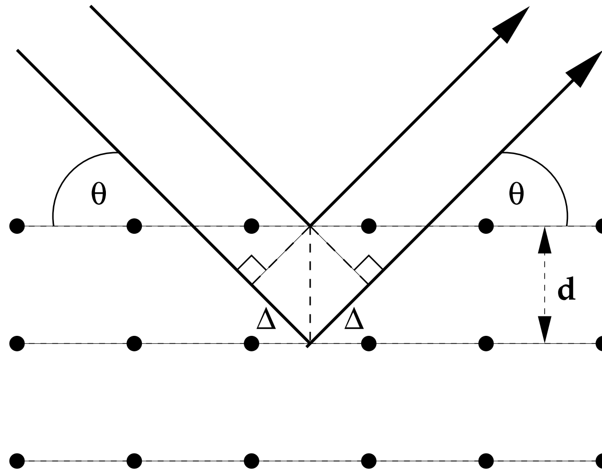

Figure 4.5: Bragg diffraction geometry

We note that the path difference of the two X-ray bundles (as indicated in the figure) is 2Δ. From the figure, we have

$$\Delta = d \sin \theta. \tag{4.3.4}$$

For constructive interference we require that the path difference must be equal to an integer multiple of the X-ray wavelength λ. From this requirement and (4.3.4), we obtain the Bragg diffraction law [25]

$$2d \sin \theta = n\lambda \qquad (n \in \mathbb{N}). \tag{4.3.5}$$

With this equation, we have a simple way of detecting sets of planes with spacing d in a material where the planes are parallel to the surface of the sample. The next section will show how this is exploited in X-ray powder diffractometers.

4.3.3 X-ray Powder Diffractometers

To obtain information about which inter-plane distances are present in a sample, measurements have to be performed at several values of θ in (4.3.5). This is done using an X-ray powder diffractometer.

Powder diffractometers implement the Bragg diffraction geometry shown in Figure 4.5. Typically, the Bragg-Brentano geometry is used in practical diffractometers. A Bruker AXS D8 Advance diffractometer was used to perform powder diffraction during this work. It uses a θ–θ measurement geometry, as shown in Figure 4.6.

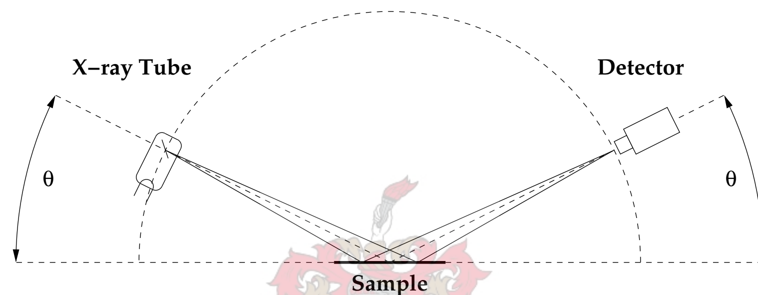

Figure 4.6: The θ–θ Bragg-Brentano Geometry

By moving both the X-ray tube and the detector so that the same angle θ is maintained by both devices relative to the substrate plane, the experimental configuration in Figure 4.5 is realised.

4.3.4 Powder Diffraction Patterns

Powder diffraction patterns provide a record of the measurements performed by powder diffractometers. They are generated in a straightforward way. The diffractometer scans the required 2θ range in discrete steps. The angular difference between successive steps is referred to as the step size. At each step, the diffractometer remains in position for a fixed amount of time. Record is kept of the number of counts the detector produces. Dividing this count by the measurement time per step produces an intensity value in counts per second (cps).

A powder diffraction pattern is produced when these measured intensities are plotted against 2θ. This generally manifests as a series of peaks, each peak being associated with some set of crystal planes with spacing defined by (4.3.5). Since in the case of device production one generally knows which material was deposited, knowledge of the inter-plane distances present in the desired material can be used to verify its presence.

4.3.5 Effects of Preferred Orientation

Preferred orientation causes the modification of the peak intensities as detected by the powder diffractometer. In the extreme case, only a subset of peaks remain present in the pattern. Only grains that have the relevant set of planes parallel to the sample surface are detected for a given 2θ.

Consider a sample covered with an epitaxial c-axis oriented thin film. Although as usual, all the lattice planes are present in the sample, only the (00n)-planes are parallel to the sample surface. Therefore, only the (00n)-peaks are present in the resulting diffraction pattern.

This observation provides us with a powerful tool in determining whether a film has grown epitaxially. One simply checks whether the peaks associated with the desired orientation is present (along with its high order multiples) to the exclusion of all other peaks.

Pectora roborant cultus recti

4.3.6 Seed Layer Diagnostics

The powder diffraction patterns of particular interest to us are those of CeO_2 and YSZ. Experimentation (as will be related in the next chapter) showed that mixed (111)- and (100)-growth is obtained for CeO_2 under various conditions. Since pure (100)-growth is desired for the seed layer, the (111)-growth must be eliminated. Powder diffraction will be used to gauge the progress of the experimentation.

CeO_2 has a lattice constant of $5.41\,\text{Å}$ [38]. For (100)-growth, we therefore expect d in (4.3.5) to be equal to $5.41\,\text{Å}$. For (111)-growth, from (4.3.3) with $h = k = l = 1$ and $a = b = c = 5.41\,\text{Å}$ we have

$$d_{(111)} = \frac{a}{\sqrt{3}} = 3.12\,\text{Å}. \tag{4.3.6}$$

The X-ray tube in the powder diffractometer used has a copper anode. After being passed through a monochromator, the emitted radiation has a mean wavelength of $K_{\overline{\alpha}} = 1.54178\,\text{Å}$ [25]. $K_{\overline{\alpha}}$ serves as the value of λ in (4.3.5). Given that we know both d and λ in (4.3.5), we can find 2θ for any n.

We are now in a position to predict where the peaks of CeO_2 will be for the (n00)- and (mmm)-orientations. However, there is an extra caveat. Due to symmetry considerations, the (100)-peak is absent in CeO_2. This is called a systematic absence [25]. Therefore, powder diffraction experiments in this work will try to identify the (200) and (111) peaks. Using (4.3.5) we have

$$2\theta = 2\arcsin\left(\frac{n\lambda}{2d}\right). \tag{4.3.7}$$

Table 4.1 lists the 2θ values for the (002)- and (111)-peaks of CeO_2. The (002)- and (111)-peaks of YSZ, which has a lattice constant of $5.14\,\text{Å}$ [38], are also given. An example powder diffraction pattern obtained from a layer of CeO_2 exhibiting mixed (111)- and (100)-growth is shown in Figure 4.7.

Material	$2\theta_{(111)}$	$2\theta_{(200)}$
CeO_2	28.6°	33.1°
YSZ	30.1°	34.9°

Table 4.1: 2θ values for the (111)- and (200)-peaks in the seed layer materials

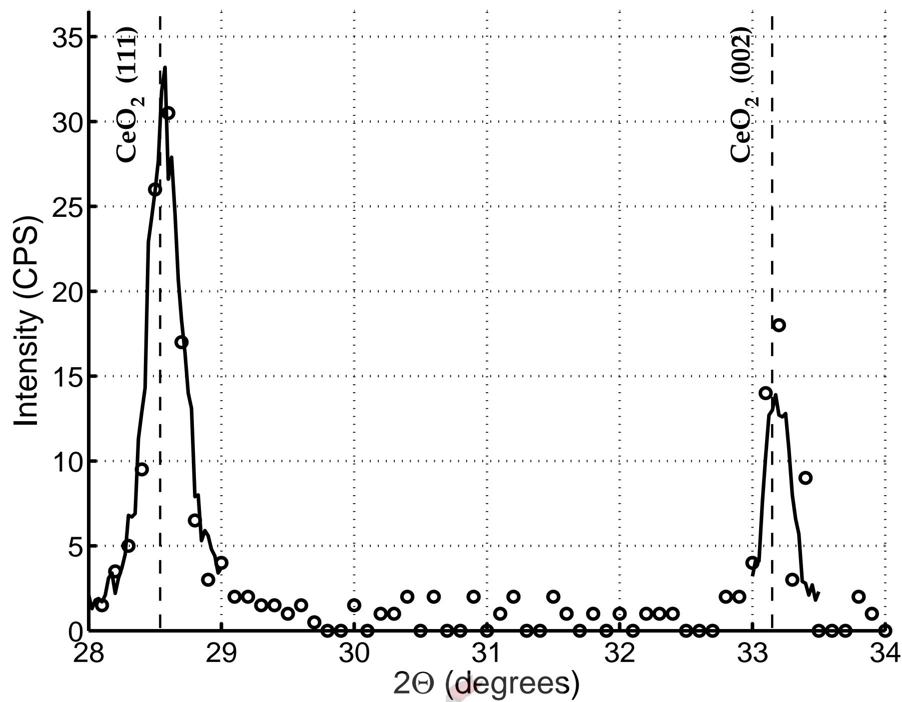

Figure 4.7: An example of a CeO_2 powder diffraction pattern

4.4 Summary

An overview of the important concepts relating to thin-film crystallinity has been provided. X-ray powder diffraction has been identified as a powerful tool for verifying the epitaxy of a thin-film. The fundamentals of powder diffraction measurements were discussed. Specific attention was paid to distinguishing between (111)- and (100)-oriented CeO_2 and YSZ, as this will be the primary application of this knowledge in the chapters that follow.

Chapter 5

Pulsed Laser Deposition

5.1 Introduction

Pulsed laser deposition (PLD) is the process where a pulsed laser source is used to ablate a target which resides in a vacuum chamber (which may or may not have an ambient pressure of an inert or reactive gas). The ablated material deposits onto a substrate which is positioned near the target. The substrate is usually mounted on a substrate heater which allows the deposition to occur at high temperatures.

PLD has become a mainstay of the high temperature superconductivity community due to its inherent flexibility in terms of possible deposition conditions and the wide variety of materials which can be ablated. The technique is relatively simple, requiring only four core components: a pulsed laser source, a vacuum chamber, a substrate heater and a target made of the chosen material (or a material which will react with the ambient gas so as to produce the desired material). The ability of the technique to allow the epitaxial growth of complex thin-films such as YBCO has further encouraged its adoption.

The purpose of this chapter is to give an overview of the process, outlining the mechanisms that give rise to deposition. The PLD of the three specific materials relevant to this work will be considered: YBCO, CeO_2 and YSZ. The effects of the use of a pulsed oxygen source, as well as a plate shadow mask will be examined. Thin-film epitaxy will be investigated

Pectora roborant cultus recti

using X-ray powder diffraction.

5.2 Process Overview

In this section, a small overview of the PLD process will be presented. The reader is referred to some of the many general reviews available in the literature for a more complete picture [1, 8, 31].

5.2.1 Experimental Setup

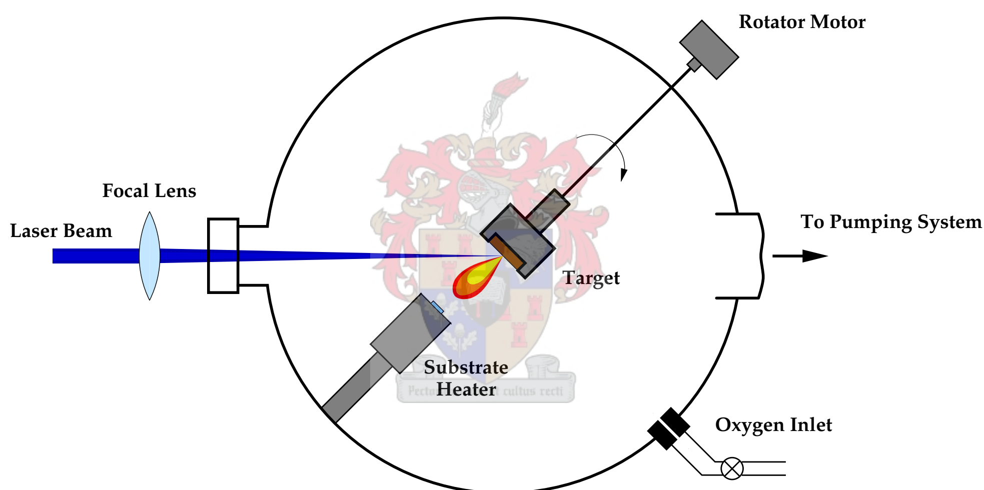

Figure 5.1: Schematic representation of the PLD setup

Figure 5.1 shows a schematic of the experimental setup for PLD. The system consists of a pulsed laser source, laser optics, vacuum chamber, target, target rotator, pre-ablation plate, substrate heater, vacuum pump and a source of ambient gas. We will now consider these elements in turn and describe their functions.

5.2.1.1 The Laser

In PLD, the energy source for material ablation takes the form of a pulsed laser. The laser is located outside the deposition chamber itself. This decoupling of the deposition chamber and the ablation energy source vastly increases the flexibility of the process by allowing the use of a wide variety of laser sources. As long as the laser characteristics are suitable, and the beam energy can be effectively coupled into the chamber, one can change conditions inside the deposition chamber almost arbitrarily without affecting the energy source [8].

For current PLD work, the excimer laser is most commonly used. This type of laser operates directly in the ultraviolet (UV) region, emitting light at wavelengths determined by the gas mixture present in the laser chamber (e.g. 157 nm for F_2 and 308 nm for XeCl).

A notable problem with the use of excimer lasers is the change in pulse energy over time. Impurities arising from the corrosion of the discharge electrodes in the laser chamber react with the halogen component of the gas mixture. This leads to a lower halogen content in the gas mixture and a correspondingly lower energy output from each discharge.

To increase reproducibility, the halogen component in the gas mixture must be replenished at regular intervals to ensure that the laser energy stays at a reasonable level. The pulse energy can then be maintained at a suitable level by adjusting the discharge voltage (although this can only be done within a narrow range).

5.2.1.2 Laser Optics

The lenses focus the beam onto the target so that the required energy density can be attained. Commercial excimer lasers tend to have rectangular beam profiles. Generally a spherical lens is employed, leading to a rectangular spot on the target. The laser aperture (the opening in the PLD chamber which allows the entry of the beam) is made from a suitable laser quality material which can transmit light efficiently at the relevant frequency. Fused silica is an example of such a material (employed at 248 nm) [8].

5.2.1.3 Vacuum Chamber

The vacuum chamber serves to provide a suitable environment for deposition to take place. One or more pumps (common examples being turbo molecular pumps or diffusion pumps) are employed to reach extremely low base pressures in the region of 10^{-5} mbar. It is desirable to keep the base pressure as low as possible to avoid atmospheric impurities contaminating the depositing thin-film.

5.2.1.4 Target

The target is generally composed of the same material that is to be deposited. For oxides, it is usually a disk made of a pressed and sintered powder. The purity of the material is of great importance, because impurities are transferred directly to the substrate along with the rest of the ablated material. Furthermore, the target material must be as uniform as possible to avoid changes in the plume as the spot position on the target changes. Another important aspect is the target consistency. A porous target can lead to the ejection of macroscopic particulates due to the explosive thermal expansion of trapped pockets of subsurface gas [1].

One of the reasons that PLD is so popular is that it is usually possible to deposit material from multicomponent targets while maintaining the same stoichiometry as the target material. In many cases, the presence of a reactive ambient gas such as oxygen allows for the restoration or addition of volatile film components. This allows one to use targets not necessarily containing all the thin-film components, for example one could use a copper target in an oxygen environment to deposit copper oxide.

5.2.1.5 Target Rotator

To avoid undesirable erosion of the target at a single spot, the target is rotated so that ablation events become spread over an annular region. Alternatively, the target may be rastered by moving it both horizontally and vertically in a regular grid. Although this is the most efficient option in terms of minimising uneven target erosion, it is also the most

complicated and is therefore not common in practice.

5.2.1.6 Pre-ablation Plate

Before depositing a thin-film, it is standard practice to ablate the surface of the target with several shots to remove impurities and degraded target material. To avoid this material depositing on the substrate, the pre-ablation plate (not shown in figure 5.1) is positioned between the target and the substrate, blocking the propagation of the material in the plume. It should be noted that, due to interactions with the background gas, it is possible for material to follow paths which are not line-of-sight. The plate must therefore be large enough to minimise this possibility. Note that advantage can be taken of this phenomenon to remove particulates, as will be discussed later.

5.2.1.7 Substrate Heater

The function of the substrate heater is threefold. Firstly, it is desirable that the heater's position and orientation relative to the target be as variable as possible to allow for alignment with the plume and changes of the working distance (the distance between the substrate and the target). One may also need to employ alternative deposition geometries (such as off-axis deposition). Secondly, it must provide a means of securing the substrate while ensuring sufficient thermal contact to avoid excessive temperature differences between the substrate and the heater. This is typically achieved by using silver conductive paint to attach the substrate to the heater. Most importantly, the heater must be able to reliably maintain temperatures appropriate to the deposition. These can be quite high for the depositions of interest to us, reaching 800 °C for some of those performed in this work.

5.2.2 Key Process Parameters

The PLD process has many degrees of freedom which influence thin-film growth in a complex, interdependent way. These include the laser energy density (E_{las}), the pulse frequency (f_{las}), the area of the spot on the target (A_{spot}), the target-substrate distance or

working distance (l_{ts}), the base pressure (P_{base}), the ambient (or average) pressure during deposition (P_{avg}), the deposition time (D_{dep}) and the substrate temperature (T_{sub}).

Although the effects the different parameters have on the resulting thin-films are complicated, certain general trends are observed.

- *Film thickness* is primarily dependent on the deposition time and the deposition rate. The deposition rate in its turn is dependent on the rate of material ejection from the target, the ambient pressure and the working distance. Increasing the pulse frequency increases the rate of material ablation. Increasing the energy density leads to greater ablation yields. Changing the spot dimensions can also change the deposition rate by changing the plume shape and therefore the preferred direction of material ejection [31]. The presence of an ambient gas causes scattering of the plume material, lowering the amount reaching the substrate. Increasing the working distance lowers the solid angle which the substrate covers relative to the plume origin, therefore lowering the deposition rate.

- *Film uniformity* is greatly influenced by the plume shape, which is largely dependent on the spot dimensions [31]. The ejected mass density has the form $cos^n\theta$ where n is empirically determined and θ is the ejection angle (with $\theta = 0°$ being normal to the target) [8]. One therefore expects the edges of the substrate to receive less material than the centre. This becomes very apparent when n becomes large (for "longer" plumes). One solution to this problem is to use larger working distances, which allows the plume material to spread out before reaching the substrate (although this does lead to lower deposition rates).

- *Film composition* depends for the most part on the target composition. A reactive ambient gas such as oxygen can react with the thin-film during its formation. Impurities from the target, especially surface impurities, can contaminate the film. Further contamination can occur due to impurities in the ambient gas, highlighting the importance of achieving very low base pressures.

- *Film crystallinity* is primarily dependent on the substrate temperature. The substrate temperature needs to be high enough to promote the surface diffusion of thin-film species. This allows the nucleation of the material into crystalline configuration.

Pectora roborant cultus recti

Deposition rates need to be low enough compared to the time taken for this diffusion to occur [1]. The ambient pressure should also be high enough to ensure the thermodynamic stability of the desired material and phase.

- *Film orientation* depends mostly on the substrate material orientation and lattice matching with the depositing thin-film (not neglecting, of course, the chemical compatability of the materials). However, process parameters can greatly influence the resulting orientation where more than one possibility exists. A good example is that of YBCO, where temperature and pressure conditions influence the deposition of either a-axis or c-axis oriented films.

5.2.3 Laser Ablation Events

Although apparently simple, the interaction of the laser pulse with the target yields a rich set of behaviours. We can identify four different stages during the evolution of the plume (illustrated in Figure 5.2) [1].

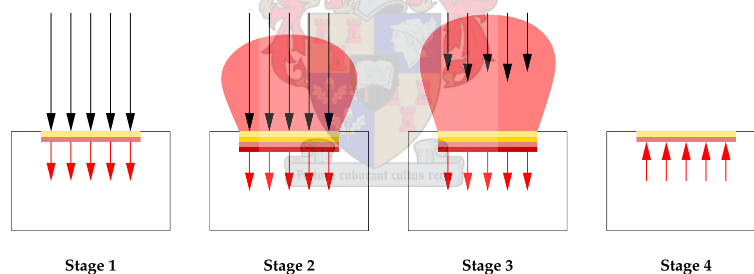

Figure 5.2: Stages of the ablation process (adapted from [1])

Stage 1: Initial interaction of the laser pulse with the target. Vaporisation and melting of the target material begins.

Stage 2: Melting and vaporisation continue, the melt front propagates into the target. Vaporised material begins to interact significantly with the incident laser beam, forming a plasma.

Stage 3: Further plasma formation due to absorption of the laser by the plume. The plasma expands adiabatically in a direction near-normal to the target.

Stage 4: Laser pulse stops. Melt front begins to recede. Re-solidification of the target.

Perhaps the greatest problem with PLD is the ejection of macroscopic particulates from the target during the ablation process. These particulates can degrade the quality of the thin-film if they alight on the substrate. Processes which produce particulates include subsurface boiling, recoil and exfoliation [37]. These processes are generally hard to suppress. To improve surface quality, particulates need to be eliminated from the depositing material after their production. One technique with this aim is shadow masking, which will be discussed shortly.

5.3 PLD Configurations

This section provides a quick overview of the PLD configurations employed in this work for the purposes of defining the various length parameters which determine the physical arrangement of the process components. The relative strengths and weaknesses of each configuration are also discussed.

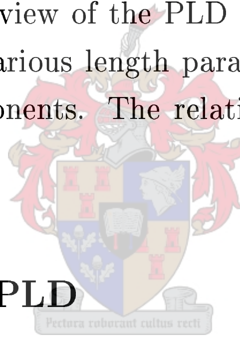
Pectora roborant cultus recti

5.3.1 Standard On-axis PLD

Figure 5.3 shows the well-known on-axis PLD configuration. The substrate is placed with its normal co-linear with the long axis of the ablation plume. The distance between the target and the substrate (l_{ts}), also known as the working distance, is the only geometrical parameter in this setup. The ambient gas pressure is maintained at a constant level throughout the deposition by using a gas inlet installed within the chamber.

This configuration, though simple, has some disadvantages. Firstly, there is nothing to prevent particulates ejected from the target from alighting on the substrate. This generally leads to poor surface roughness, which makes subsequent growth of multilayers difficult. Secondly, at the ambient pressures needed for the deposition of substances such as YBCO, the ablation plume is relatively short and the working distance has to be kept small in order for significant deposition rates to be achieved. Since plume expansion is anisotropic, this generally leads to non-uniform layer thicknesses.

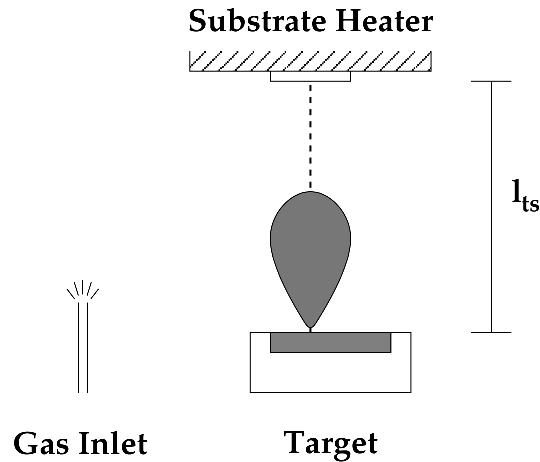

Figure 5.3: Geometry of standard PLD

These problems notwithstanding, the standard PLD configuration is still very useful for performing studies on thin-film formation. It will be used as such for obtaining an initial understanding of the deposition of the seed layer in Section 5.6.

5.3.2 Non-Standard PLD Configurations

For the reliable manufacture of multilayer devices, thin-films have to be uniform and mostly free of particulates. In this section, two alterations to the standard PLD configuration are considered which address these issues. These are the use of a pulsed oxygen source and the addition of a plate shadow mask.

5.3.2.1 PLD with a Pulsed Oxygen Source

As stated previously, the relatively high ambient pressure needed during standard PLD limits the size of the ablation plume, leading to non-uniformity of the resulting thin-film when the working distance is decreased in order to achieve significant deposition rates. Any method which allows freer expansion of the ablation plume would allow the working distance to be increased, counteracting this problem.

Gupta and Hussey studied the use of a pulsed oxygen source in the deposition of YBCO [13].

This allows for the free initial expansion of the ablation plume, enlarging it considerably. Figure 5.4 shows the configuration as used in this work.

In addition to the target and the substrate, there is now also a pulsed gas valve present in the chamber. The valve is oriented towards the substrate, while the substrate heater and target remain in their positions as for the standard configuration[1]. The distance between the valve and the substrate is given by l_{gs}, while the distance between the valve and the target is given by l_{gt}.

The valve is triggered a time τ before the laser. This allows the gas pulse to expand towards the substrate before the plume is generated. This delay is necessary to allow interaction, because the ablation fragments have velocities an order of magnitude larger than the velocity of the gas pulse [13]. The valve remains triggered for a duration of $\mathrm{T_p}$, determining how much oxygen is released in each pulse (note that the stagnant pressure in the feed line $\mathrm{P_{line}}$ is also important in determining this).

Since the initial expansion of the ablation plume is relatively free, the plume appears larger compared with standard PLD. Section 5.4 examines the interaction of the plume and the gas pulse.

In order to uniquely specify the geometry, the three lengths l_{ts}, l_{gs} and l_{gt} need to be known. Because the valve and target positions did not change during the course of these experiments, we find that we only need l_{ts} to determine the geometry. This is because l_{gt} is a known constant, as well as the angle α between the vector connecting the target and substrate and the vector connecting the target and the valve. It is therefore sufficient to relate only l_{ts} for each experiment. Except if stated otherwise, l_{gt} was set to 64 mm and α to 64°.

[1]This configuration differs somewhat from that used by Gupta and Hussey. These researchers placed the components so that the incoming plume and the incoming gas pulse each make a 45° angle with the substrate. However, the operation principal remains the same.

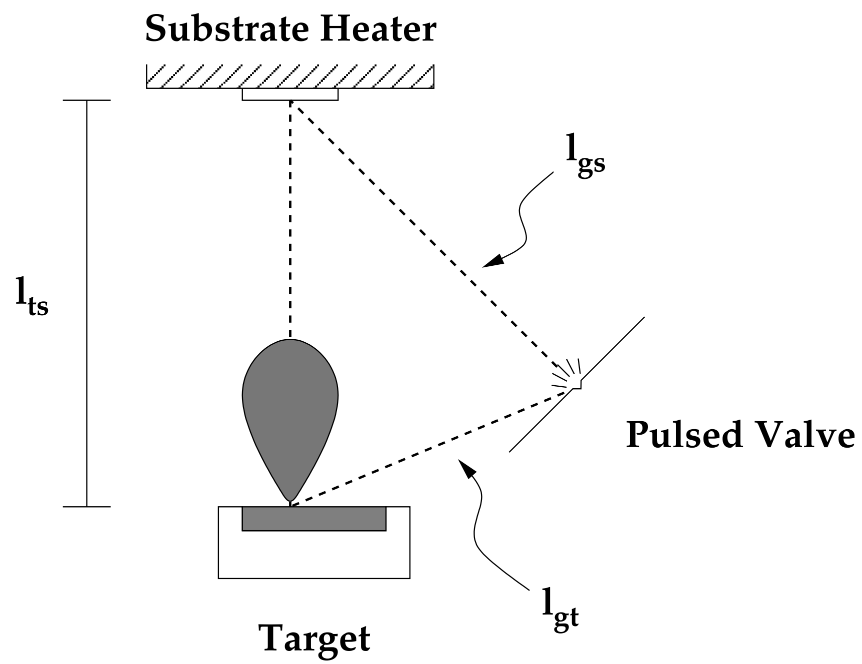

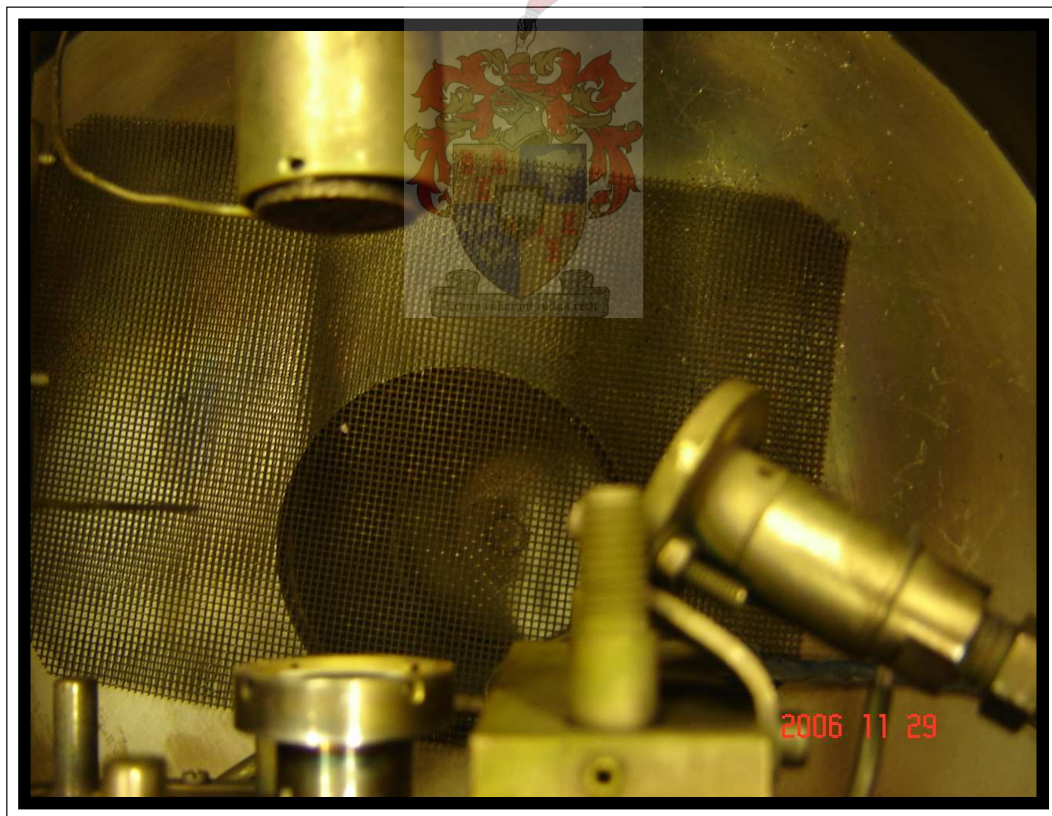

Figure 5.4: Geometry of PLD with a pulsed oxygen source (no shadow mask)

5.3.2.2 Plate Shadow Mask

One popular solution to reduce the number of particulates reaching the substrate is the inclusion of a shadow mask in the deposition geometry. A shadow mask is a physical obstruction which blocks line-of-sight deposition. Since particulates tend to have large momenta, they are less likely to be scattered into the shadowed region. The atomic and ionic constituents of the plume (as well as some of the smallest particulates) can however be sufficiently scattered to enter the shadowed region. Placing the substrate in this region therefore significantly reduces surface particulates in the resulting thin-film [24].

Previous researchers at the University of Stellenbosch utilised a variety of shadow masks [30, 11]. However, the resulting films suffered from non-uniformity. This problem can be traced back to the scale of the deposition geometry. Since the deposition rate is lower with the shadow mask, the geometry has to be compact. The small distances between the mask and the substrate do not allow for non-uniformities to spread out sufficiently. The pulsed oxygen source allows for larger plumes, changing the length scale of the deposition. Since the substrate size does not change, this implies a more uniform deposition, because the non-uniformities are more spread out by the time the substrate is reached.

To implement a shadow mask, a simple plate of appropriate size can be placed in between the target and the substrate [24]. Figure 5.6 shows this configuration. The addition of a plate shadow mask adds two parameters to the geometry. Firstly, there is the separation between the target and the shadow mask given by l_{tm}. Secondly, there is the shadow mask overhang l_m, defined as the distance between edge of the shadow mask and the spot where the plume axis intersects the shadow mask. Note that the plate has vertical extents as well, therefore l_m may have distinct values in the horizontal and vertical directions (indicated by l_{mx} and l_{mz} respectively). In this work, l_{tm} was set to 35 mm. The shadow mask overhang parameters l_{mx} and l_{mz} were 17 mm and 25 mm respectively.

Figure 5.5 shows the improved surface quality gained through the use of the shadow mask. Both cases were depositions of YBCO. Note the near absence of large particulates in the case where the shadow mask was employed.

Pectora roborant cultus recti

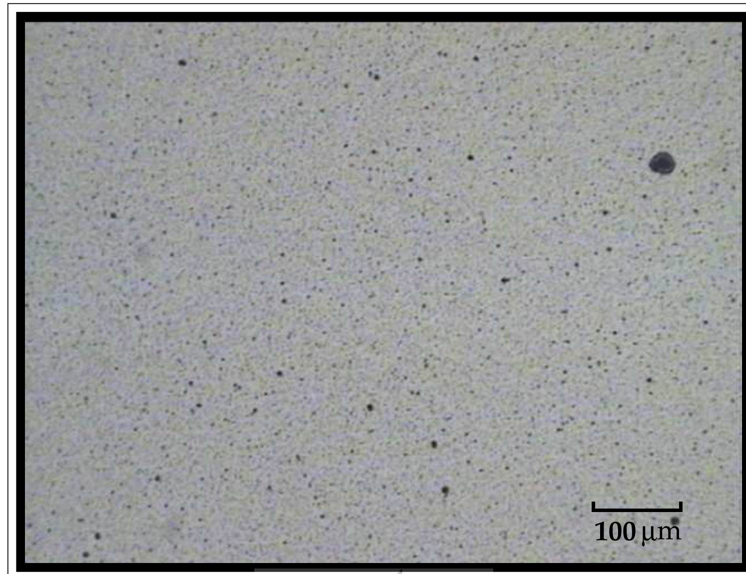

Without Shadow Mask

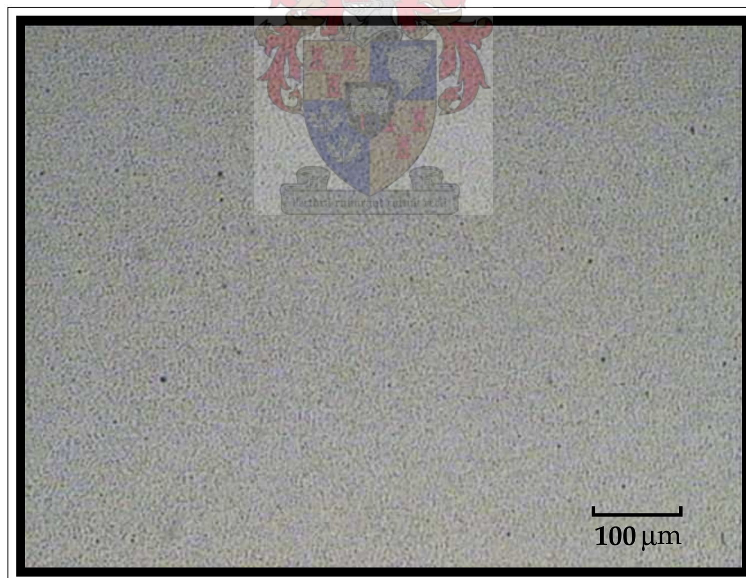

With Shadow Mask

Figure 5.5: Improvement of the surface quality using a shadow mask

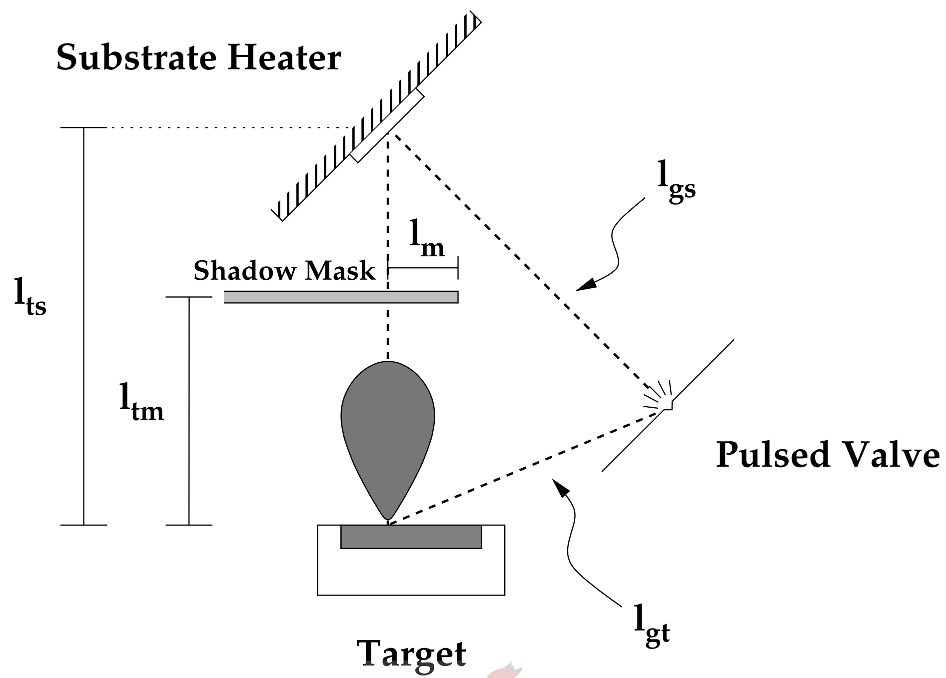

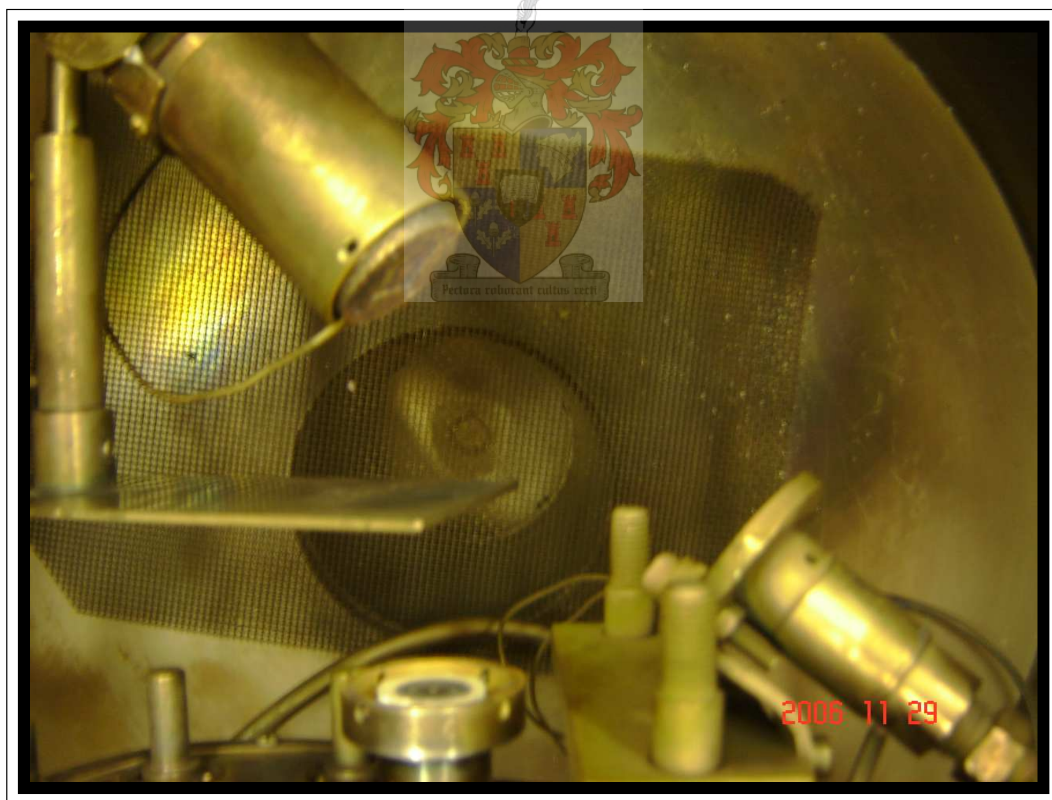

Figure 5.6: Geometry of PLD with pulsed oxygen source (with shadow mask)

5.4 Pulsed Oxygen Source

5.4.1 Valve timing

To achieve the desired interaction between the ablation plume and the oxygen pulse, we must consider the timing and synchronisation of the laser and the pulsed valve. Appendix A describes the equipment setup used for triggering the valve and the laser. In this section, the effect of changing the timing parameters is discussed.

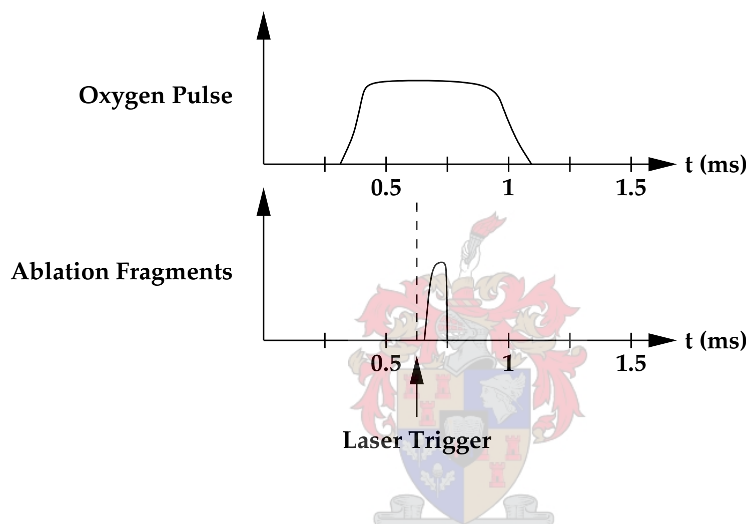

Figure 5.7: Ion gauge signal adapted from [13]. The source did not provide vertical axis divisions.

Figure 5.7 shows the arrival of a gas pulse and ablation plume species at the substrate in an experiment performed by Gupta and Hussey [13]. The gas pulse is triggered first, followed by the laser at a later time (about 625 μs in the figure). Note that the gas pulse takes much longer to reach the substrate, whereas the ablated material reaches the substrate in a time very small relative to the gas pulse length.

Proper timing is essential to ensure that the ablated material and the gas pulse reach the substrate at the same time. Define the laser delay as τ. The critical value τ_{onset} is that value of τ for which the ablated material reaches the substrate just as the gas pulse does. For lower τ, there is no interaction between the plume and the gas pulse at the substrate. There is also a time τ_{cutoff} where the ablated material reaches the substrate just as the gas pulse has passed. After this time, there is none of the needed interaction.

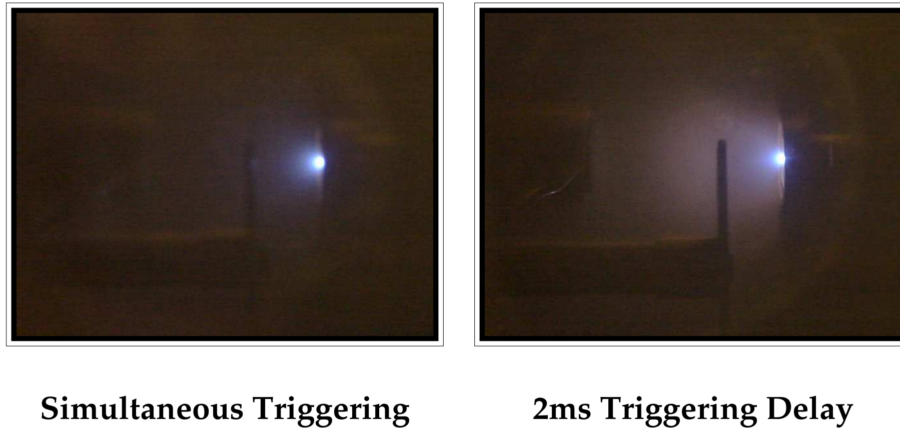

Figure 5.8: Plume brightening due to interaction of the gas pulse and the ablation plume

Fortunately, the correct synchronisation can be verified visually, as a significant brightening of the plume occurs for correct settings of τ [13]. This phenomenon is shown in Figure 5.8, where the researcher utilised an YSZ target to demonstrate the effect of valve timing. The brightening of the plume is clearly visible in the case where the laser is triggered 2 ms after the valve.

Because the valve operating delays can change due to servicing and temperature effects, calibration needs to be performed regularly. Calibration is also needed after changes to the deposition geometry. During calibration, the system is operated without a sample at the deposition temperature. The laser delay is adjusted in 100 μs increments until the onset of the plume/gas pulse interaction is observed. The laser delay is then increased by some value (400 μs for this work) to ensure good interaction. The gas pulse length is adjusted until the desired average chamber pressure is measured. The plume luminosity is checked again to ensure the correctness of the settings. Combined with knowledge of the vacuum system's pumping capacity, this makes the experimental conditions fairly reproducible. For the experimental data quoted in this work, absolute triggering delays of the order 2.0 ms were used.

5.5 YBCO Deposition

The PLD of YBCO, using the standard PLD configuration, was optimised locally by Rottier [30]. Taking his work as a point of departure, films of YBCO were deposited to gain familiarity with the PLD process.

Parameter	Value
Oxygen Pressure	0.4 mbar
Substrate Temperature	720 °C
Ozone Generator	On
Target-Substrate Distance	40 mm
Laser Pulse Frequency	10 Hz
Laser Energy	3.4 J/cm^2

Table 5.1: Optimal standard PLD parameters for YBCO used by Rottier [30]

In addition to the deposition step, YBCO needs to be annealed at high temperature in a high oxygen environment to promote the conversion of the oxygen poor tetragonal phase into the desired orthorhombic phase. In the course of this work, a 30 min anneal in 1 atm of oxygen at 500°C was found to be sufficient for these purposes.

The parameters in Table 5.1 were used as a guideline, with changes made as needed. No ozone generator was used to ionise the oxygen before it entered the chamber, since it was found that this leads to quick degradation of the O-rings, causing vacuum leaks.

Büttner extended these results for the pulsed oxygen valve [3], showing that (similar to [13]) good quality YBCO layers can be deposited at average pressures down to 0.06 mbar, allowing increased working distance and hence greater uniformity.

Several depositions onto bare MgO substrates were performed. It was decided to utilise the pulsed oxygen source for YBCO deposition because of its superior uniformity. The susceptibility test (shown in Figure 5.9) of one of the samples (deposited using parameters listed in Table 5.2) shows a T_c of 80 K with a transition width of 4 K. This reasonable transition width and relatively high T_c (YBCO has a maximum T_c of 92 K) are indicators of good thin-film quality.

Parameter	Value
Average Oxygen Pressure	0.06 mbar
Substrate Temperature	720 °C
Target-Substrate Distance	76 mm
Valve-Substrate Distance	76 mm
Valve-Target Distance	64 mm
Laser Pulse Frequency	12 Hz
Laser Energy	13.0 J/cm^2

Table 5.2: Pulsed Oxygen PLD parameters for YBCO

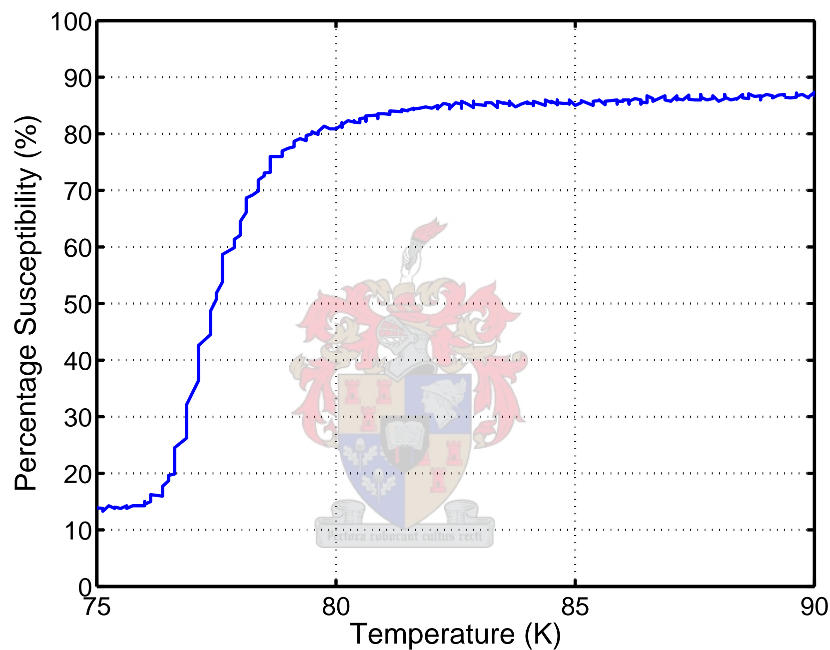

Figure 5.9: Susceptibility test for the pulsed oxygen YBCO PLD

5.6 Seed Layer Deposition

As stated in Chapter 3, the seed layer that will be used for biepitaxy in this work is CeO_2. The resulting device will be similar to those fabricated by Petersen *et al* [28] and Yang *et al* [39]. It is the purpose of this section to find a suitable set of parameters for the PLD of the seed layer. Petersen *et al* made use of on-axis RF magnetron sputtering to deposit their seed layers. There does however exist work by other researchers which make use of

PLD to deposit CeO_2.

Li *et al* [21] used a KrF excimer laser (248nm) to perform deposition of, amongst other materials, CeO_2 onto MgO. The target was a pressed pellet of CeO_2 powder sintered for 12 hours at 1400 °C. A target-substrate distance of 40 mm was maintained. Deposition conditions varied, with the temperature ranging from 730 °C to 780 °C and the oxygen pressure from 0.27 mbar to 0.53 mbar.

These researchers report mixed (111)- and (100)-growth under certain conditions. At an oxygen pressure of 0.27 mbar films were completely (100)-oriented for depositions performed below 750 °C, with mixed orientations observed at higher temperatures. They also state that an increase in oxygen pressure increases the maximum temperature for which pure (100)-growth is obtainable to 775 °C.

The group also reports that a significant fraction (at least 5%) of each thin-film grows with an in-plane rotation of 45° relative to the MgO substrate. This statement is corroborated by the results of Wu *et al* [38]. This could lead to undesired grain boundaries along the edges of these misoriented regions. Li *et al* propose the addition of a layer of YSZ under the CeO_2 to remedy this problem [21].

5.6.1 Normal PLD of Cerium Oxide

The PLD of CeO_2 can be performed similarly to that of YBCO, but without the annealing step. However, finding the deposition parameters needed to obtain the correct crystallographic orientation is problematic and is the subject of the following sections.

Initially, only a CeO_2 target was available to the researcher and so the unbuffered CeO_2 approach of Petersen *et al* was used to fabricate the prototype device. In order to achieve this, layers of CeO_2 were deposited on MgO using the local PLD facility. The crystallographic orientation of the resulting films was investigated using X-ray powder diffraction.

The target was manufactured locally using CeO_2 powder (99.9% pure) purchased from Alfa Aesar. The powder was pressed into pellet form and sintered in pure oxygen at 1000 °C

for 12 hours[2].

Several PLD runs were performed. The experimental parameters for each of these runs are listed at the end of the chapter in Table 5.3 along with the resulting values of the powder diffraction peaks. $C_{(111)}$ is the measured (111) peak intensity in counts per second (cps), with $C_{(200)}$ being the measured (200) peak intensity. The ratio of the two values $\beta = \left(\frac{C_{(200)}}{C_{(111)}}\right)$ is also tabulated. Since $C_{(200)}$ represents the desired growth and $C_{(111)}$ the undesired growth, their ratio is a figure of merit for how well each thin-film has grown in terms of its crystallographic orientation (higher values implying more favourable growth). Note that the individual intensity values $C_{(hkl)}$ should not be compared since the XRD scan parameters vary between samples. The powder diffraction patterns obtained from the samples are shown in Appendix B.

Initial parameters were chosen close to those used by Li *et al.* Sample S1 was deposited at 750 °C. To avoid mixed orientation growth, the ambient oxygen pressure was set at 0.55 mbar as suggested by these authors. As can be seen from the table, the layer showed mixed orientation with $\beta = 14$. Although the (100)-growth is clearly dominant, this is still not nearly as good as the pure (100)-growth reported by Li *et al.*

Consequently, other deposition parameters were used in an attempt to find a suitable parameter set. The deposition pressure was chosen as the principal variable, since Li *et al* reported that variations of the deposition pressure led to the elimination of (111)-growth in some cases. For most of the standard PLD runs, the temperature was kept at 750 °C. The deposition pressures ranged between 0.05 and 0.55 mbar. None of these samples (S1–2, S4–6) showed β greater than 18.

Petersen *et al* performed RF magnetron sputtering at 560 °C and, as such, layer S3 was deposited at the lower temperature of 680 °C to test for possible improvement of the epitaxy. A base for comparison is available in the form of layer S2, which had identical deposition conditions except for the temperature. It was shown that lowering the deposition temperature in this case caused an undesired enhancement of (111)-growth, with β falling from 0.47 to 0.12.

[2]It should be noted that this temperature is 400 °C below the value quoted in [21]. Unfortunately the available furnace could only reach 1000 °C. Increasing the sintering temperature could lead to a better target consistency.

Layer S7 was deposited at the slightly higher temperature of 780 °C. Again, a base for comparison is available, given by the results of layer S4. The increased temperature produced inferior results, with β dropping from 18 to 7.7.

None of the layers produced by standard PLD showed pure (100)-growth. As such, enhancements to the process were investigated to remedy the situation, the results of which are discussed in the following sections.

5.6.2 PLD of Cerium Oxide with a Pulsed Oxygen Source

A pulsed oxygen source and shadow mask were employed to see if improved layer quality would lead to more favourable epitaxy. Table 5.3 lists the results of these runs. A shadow mask was employed in three of the runs (P1–P3). P4 was performed using only the pulsed oxygen source.

In all the samples listed, the layers appeared uniform. This stands in contrast with the standard PLD samples which tended to be thicker towards the centre of the sample surface. Although most of the runs done with the pulsed oxygen source have appearances that suggest good uniformity (except in cases of poor alignment), the shadow mask does add complications. Because the deposition is dependent on the scattering of material around the mask, it was found that uneven thin-films result when the shadow mask is too close to the substrate (usually this manifested as a semi-linear gradient in the apparent thickness). Placing the mask closer to the target seems to improve the process.

The run performed without the shadow mask was relatively poor, with $\beta = 2.75$ (although this could probably be ascribed to the lower deposition temperature). However, the shadow mask runs generally produced better results than the standard PLD configuration, with β reaching 24. Layer P1 was the most uniform and well oriented ($\beta = 24$) of the pure CeO_2 depositions, and was chosen as the seed layer for the prototype device discussed in a later chapter.

Pectora roborant cultus recti

5.6.3 Cerium Oxide Seed Layer with YSZ Buffer Layer

Since the previous results suggested that the direct deposition of the CeO_2 seed layer is unreliable, it was decided to use a buffer layer of YSZ in order to suppress the (111)-growth. This would also remove the possibility of mixed in-plane rotation of the CeO_2 as reported in [21, 38].

YSZ (8% mol Y_2O_3 and 99.9% pure) was purchased from MTI Crystal Corporation. The powder was pressed into a pellet and sintered at 1000 °C for 12 hours. The resulting target was used to perform depositions D1 and D2 shown in Table 5.3. The powder diffraction patterns obtained from these samples are shown in Figure 5.10.

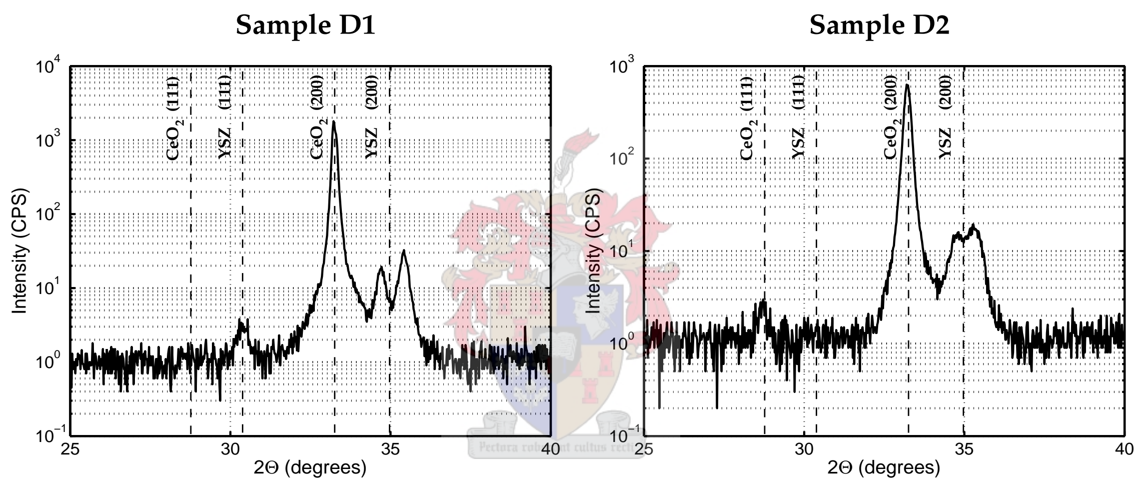

Figure 5.10: Powder diffraction patterns for Samples D1 and D2

The tabulated results show a vast improvement in β when an YSZ buffer layer is present. Indeed, for sample D1, the (111)-peak was below the noise level of the measurement, giving a value for β of at least 2000. Although the deposition temperature was now higher at 800 °C, it is unlikely that this large change in β could result from this change in temperature (note that sample S7 was deposited at 780 °C and only had $\beta = 7.7$).

Note also that both the pulsed and continuous oxygen sources produced similar results. It should be stated though that the sample produced with the pulsed oxygen source did show a very small amount of (111)-growth, but this peak is two orders of magnitude smaller

than the (200)-peak. This resulted in a β of 200, which is one order of magnitude better than any of the unbuffered samples.

Given these excellent results, it is recommended that future production runs use an YSZ buffer layer to suppress mixed orientation growth in the subsequent CeO_2 layer.

5.7 Summary

In this chapter, an overview of the PLD process was presented. The standard PLD configuration was discussed. This was expanded to include non-standard additions such as a pulsed oxygen source and a plate shadow mask. The rationale behind the triggering of the pulsed oxygen valve was discussed, along with the calibration procedure used during the experiments. YBCO depositions were performed using the pulsed oxygen valve, showing good results. A study of the deposition of CeO_2 was performed. Depositions of this substance were performed using each of the configurations discussed. It was found that the mixed orientation of the CeO_2 seed layers could be effectively suppressed using an YSZ buffer layer.

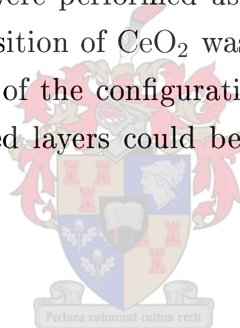
Pectora roborant cultus recti

Sample	T_{sub}(°C)	P_{avg}(mbar)	f_{las}(Hz)	D_{dep}(min)	l_{ts} (mm)	Mask	E_{las}(J/cm^2)	$C_{(111)}$ (cps)	$C_{(200)}$ (cps)	β
Process Parameters for Normal PLD of CeO_2										
S1	750	0.55	3	5	35	No	9.7	5	70	14
S2	750	0.5	10	20	31	No	6.3	175	82	0.47
S3	680	0.5	10	20	31	No	5.5	180	20	0.12
S4	750	0.15	10	20	35	No	5.2	20	360	18
S5	750	0.05	10	20	41	No	5.2	33	14	0.42
S6	750	0.1	10	20	41	No	5.2	60	300	5
S7	780	0.15	10	20	35	No	4.7	10	77	7.7
Process Parameters for PLD of CeO_2 with a Pulsed Oxygen Source										
P1	740	0.1	16	30	74	Yes	14.3	1	24	24
P2	720	0.1	16	30	76	Yes	13.6	5	62	12.4
P3	740	0.1	16	30	80	Yes	9.7	0.5	10	20
P4	690	0.1	16	20	80	No	7.8	12	33	2.75
Process Parameters for PLD of CeO_2 and YSZ										
D1[a]	800	0.3	8	20	40	No	5.8	< 2	2000	> 1000
D2[b]	800	0.06	16	10	63	No	7.1	3	600	200

Table 5.3: Process parameters for PLD of the seed layer

[a]Normal PLD.
[b]Pulsed Oxygen PLD.

Chapter 6

Thin-Film Patterning

6.1 Introduction

After deposition, it is necessary in many cases to selectively remove areas of the thin-film. This patterning is performed using a combination of a masking and an etching process. The masking process defines the areas which are to be protected from the etch process. This important part of the manufacturing process, which allows the definition of the circuit elements, is the subject of this chapter.

Parts of the patterning processes used in this thesis were inherited from previous researchers. There are, however, important changes which must be discussed along with the presentation of a few improvements. UV photolithography was utilised as the masking process in this work and will be discussed in the first part of this chapter. The etching process employed was argon ion milling, which will occupy the last part of the chapter.

6.2 Ultraviolet Photolithography

The first step in the patterning of thin-films is protecting the regions which are to be left unetched. Ultraviolet (UV) photolithography is a popular process in which a sample is

covered with a film of photoresist. As the name suggests, photoresist has the function of resisting the etching process. It is also photosensitive, allowing resist coverage of the sample to be defined by a photographic process.

Positive photoresists, such as the one used in this work, become more soluble with respect to a suitable developer after being exposed to ultraviolet radiation. By selectively covering the photoresist with a mask during exposure to an ultraviolet light source, only the uncovered regions of the photoresist become soluble. Exposure to the developer dissolves the exposed regions, leaving behind a photoresist image of the dark regions of the mask.

UV photolithography is an established process in industry and has also long been performed at the University of Stellenbosch. Many texts are available which provide a general overview of photolithography [22]. The local process has also been documented by several researchers [11, 32]. The interested reader is referred to these texts for a full discussion of the process.

6.2.1 Procedure

The process of producing a photoresist mask is relatively simple, consisting of 6 steps: cleaning, resist spinning, soft baking, exposure, development and hard baking.

First, the sample is throughly cleaned by immersing it in acetone and placing it in an ultrasonic bath for a few minutes to dislodge any impurities that have collected on the surface. The sample is then rinsed in deionised water, followed by blowing it dry with nitrogen gas.

The sample is now coated with photoresist. This is achieved by covering the sample in photoresist and spinning off the excess at high speeds. A special resist spinner is used for this purpose. The rotational velocity of the spinner determines the resist thickness, with the resist datasheet providing the relationship between these two quantities. After this, the sample is placed on a hot plate for soft baking to remove the remaining solvent in the resist and to improve film adhesion.

The resist layer is now ready for exposure. A mask aligner is used to align the chrome mask with the sample. Exposure is then performed by opening the shutter of the UV source for

a given amount of time.

Having exposed the resist layer, the exposed regions must be removed. The sample is placed in a developer solution and agitated in order to dissolve the exposed regions.

Finally, the sample is placed on a hot plate for hard baking. This removes any residual solvent and hardens the resist layer further against etching.

The parameters used for this procedure, as well as images of the resulting photoresist patterns, are related in the relevant patterning steps in Chapter 7, which covers the manufacture of the prototype.

6.3 Argon Ion Milling

6.3.1 Process Overview

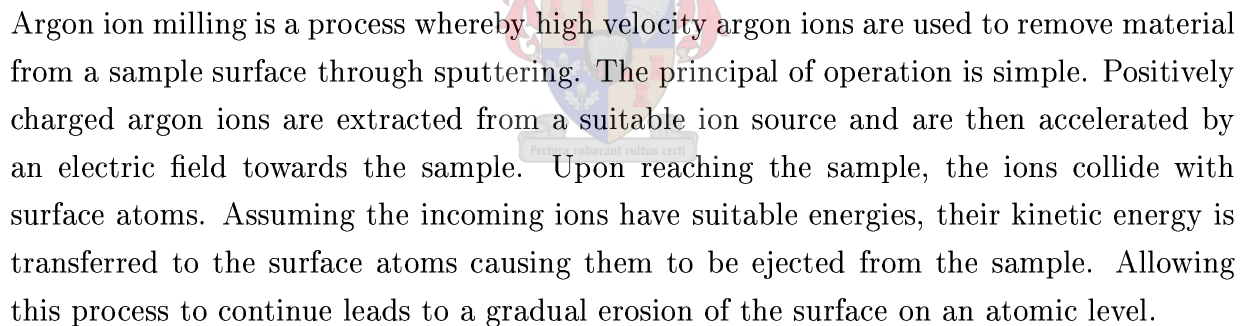

Argon ion milling is a process whereby high velocity argon ions are used to remove material from a sample surface through sputtering. The principal of operation is simple. Positively charged argon ions are extracted from a suitable ion source and are then accelerated by an electric field towards the sample. Upon reaching the sample, the ions collide with surface atoms. Assuming the incoming ions have suitable energies, their kinetic energy is transferred to the surface atoms causing them to be ejected from the sample. Allowing this process to continue leads to a gradual erosion of the surface on an atomic level.

The kinetic energy of the incoming argon ions determine the reaction of the surface (see Table 6.1). The energy must be high enough to break chemical bonds (which have energies on the order of $1\,\mathrm{eV}$ [18]) and must also impart enough energy for ejection of the material. Energies that are too high lead to undesired implantation of the ions below the surface. From Table 6.1 we see that the sputtering process requires energies in the range $10 - 5000\,\mathrm{eV}$.

Ion Energy (eV)	Reaction
< 3	Physical adsorption
$4 - 10$	Some surface sputtering
$10 - 5000$	Sputtering
$10000 - 20000$	Implantation

Table 6.1: Energy requirements associated with various physical processes [22]

6.3.2 Local Milling Facility

The argon ion milling performed during this work was done using the local argon ion milling facility. Several researchers have contributed to the development of this system [30, 32]. The system is shown in Figure 6.1 (note that the figure shows the mill in its current state, which includes the new multi-aperture extraction grids).

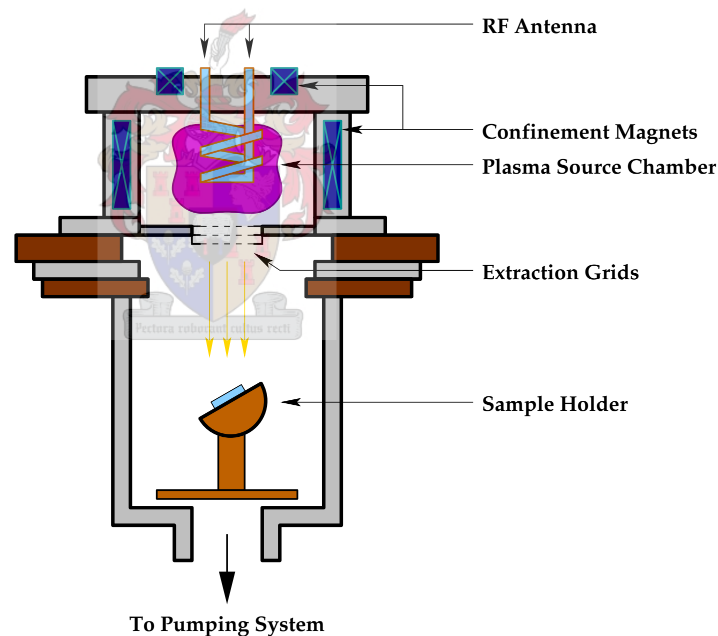

Figure 6.1: Diagram of the local argon ion milling facility

The argon ion mill consists of a plasma source chamber, a set of extraction grids, a milling chamber with a water-cooled tiltable sample holder and a diffusion pump for producing the necessary vacuum. A gas inlet in the plasma source chamber allows the addition of neutral argon gas to the plasma. A high-voltage DC power supply is used to drive the

extraction grids, providing a dual rail supply of up to 10 kV with currents on each rail having a maximum of 5 mA.

An RF multicusp ion source is used to generate the plasma. RF power at 13.56 MHz is inductively coupled into the argon gas using a water-cooled coil antenna. An RF power source is connected through a matching network to the coil. The plasma is confined to the centre of the chamber by an arrangement of $Sm - Co_5$ permanent magnets which are also water-cooled [32].

The system as used by Snetler [32] had not yet been used on YBCO and was unsuitable for the etching of thin-films in general due to the non-uniformity of the resulting etch. The etching at the centre of the sample was always appreciably deeper in comparison with the etching at the edges of the sample. This was so pronounced that the non-uniformity could be verified visually. To remedy this, it was decided to replace[1] the single aperture extraction system with a set of three aligned multi-aperture extraction grids which have aperture geometries similar to those found in Aston and Kaufman [2]. The physical implementation of the extraction grids is documented by Büttner [3]. Figure 6.2 shows a schematic representation of one set of aligned apertures.

Replacement of the single aperture extraction system led to etching that was visibly more even, appearing uniform across the surface of a sample with dimensions of $1\,\mathrm{cm} \times 1\,\mathrm{cm}$. Where it was necessary in the system used by Snetler to rotate the sample holder to increase uniformity, the new setup was able to produce uniform etching without using rotation.

Van Staden [36] performed further optimisation of the resist profiles and mill operation. The reader is referred to his work for further information regarding the local milling facility.

6.3.3 Mill Operation

In this section, the basic operating procedure of the argon ion mill is presented using the parameter set employed in this work. The resulting etch rates for YBCO and CeO_2 are also given.

[1]Note that this work was performed in conjunction with other researchers [3, 36].

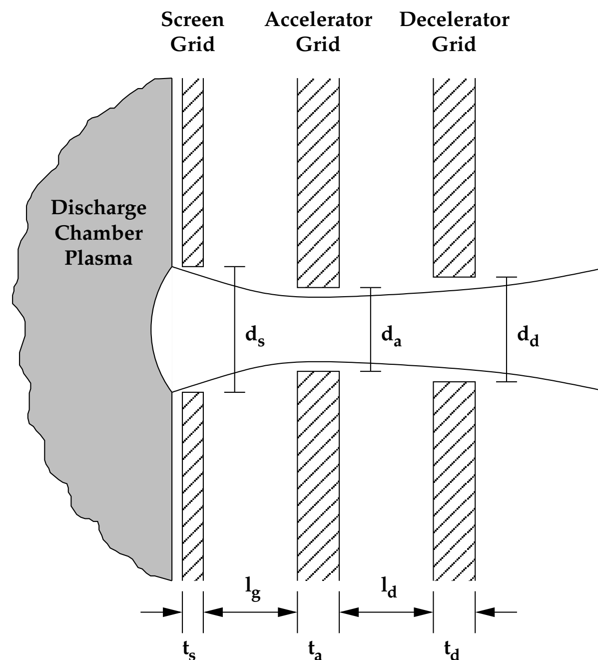

Figure 6.2: Three-grid accelerator system (adapted from [2])

The first step in operating the mill is placing the substrate in the sample holder. The back of the sample is covered with heat sink paste to ensure good thermal conductivity between the sample and the sample holder. This is important, since the heating effect due to the incoming ion beam can be considerable, causing heat damage to the resist.

The sample holder is tilted to the correct angle. For YBCO, the sample is kept horizontal. This ensures that the resulting YBCO features have identical sidewall profiles. It was found that dielectrics such as CeO_2 etch slower than YBCO (possibly due to charging effects at the surface). Tilting the sample tends to enhance the etch rate. Since the functioning of bi-epitaxial devices is critically dependent on the removal of the undesired seed layer region, the sample is placed at a 45° angle to increase the etch rate.

The sample holder is placed in the centre of the milling chamber. Depending on the stand used to support the sample holder, the distance between the sample and the extraction grids (the working distance) can be altered. For the etching performed in this work, a working distance of approximately 100 mm was used.

The chamber is now evacuated to a base pressure of 4×10^{-5} mbar using a system consisting

of a roughing pump and a diffusion pump. Argon gas is allowed to enter the chamber, raising the pressure to 2.5×10^{-4} mbar. The water cooling for the entire system is switched on. The plasma is then ignited by switching on the RF power source (set at 40 W output power). The tuning network is adjusted to minimise the reflected power (which should be below 3 W). Finally, the high voltage sources for the extraction grids are turned on. The system is then left for the allotted etching time, after which it is switched off and the sample removed.

Aston and Kaufman used the extraction grids in a configuration where the grid on the plasma side, the screen grid, was at a positive voltage V^+. The middle grid, the accelerator grid, was at a negative voltage V^-. The final grid, the decelerator grid, was kept at ground. Ions emerging from the grounded plate then have energies of about V^+ (in eV).

With this configuration, it was found that etching occurs at an extremely slow rate (needing several hours for appreciable amounts of material to be removed). It was decided to use the final grid for further acceleration. This was done by reversing the voltages on the middle and final grids. Ions emerging into the milling chamber now have energies of $V^+ - V^-$. Note that V^- is negative, so the energy is larger than for the previous configuration.

V^+ was set to 1.5 kV and V^- to -2 kV for the fabrication of the prototype. Etch runs on thick layers of YBCO and CeO_2 were performed. The YBCO sample was placed horizontally and the CeO_2 at 45°. The CeO_2 layer was etched for 30 min. The resulting trench depth was measured using Atomic Force Microscopy (AFM) (see Figure 6.3), giving a depth of approximately 315 nm. The YBCO layer was etched for 20 min, resulting in a trench of 140 nm. This implies etch rates of 10.5 nm/min for CeO_2 at 45° and 7 nm/min for YBCO placed horizontally.

Note from Figure 6.3 that the step angle is 12°. One must not discount the risk of unwanted step-edge junctions forming due to prolonged etching of the seed layer. Because the sample will be over-etched to ensure the removal of the seed layer (since there is no equipment to verify its absence experimentally), extra care will be taken during testing to distinguish between undesired low-angle step-edge junctions and 45° asymmetric grain boundary junctions.

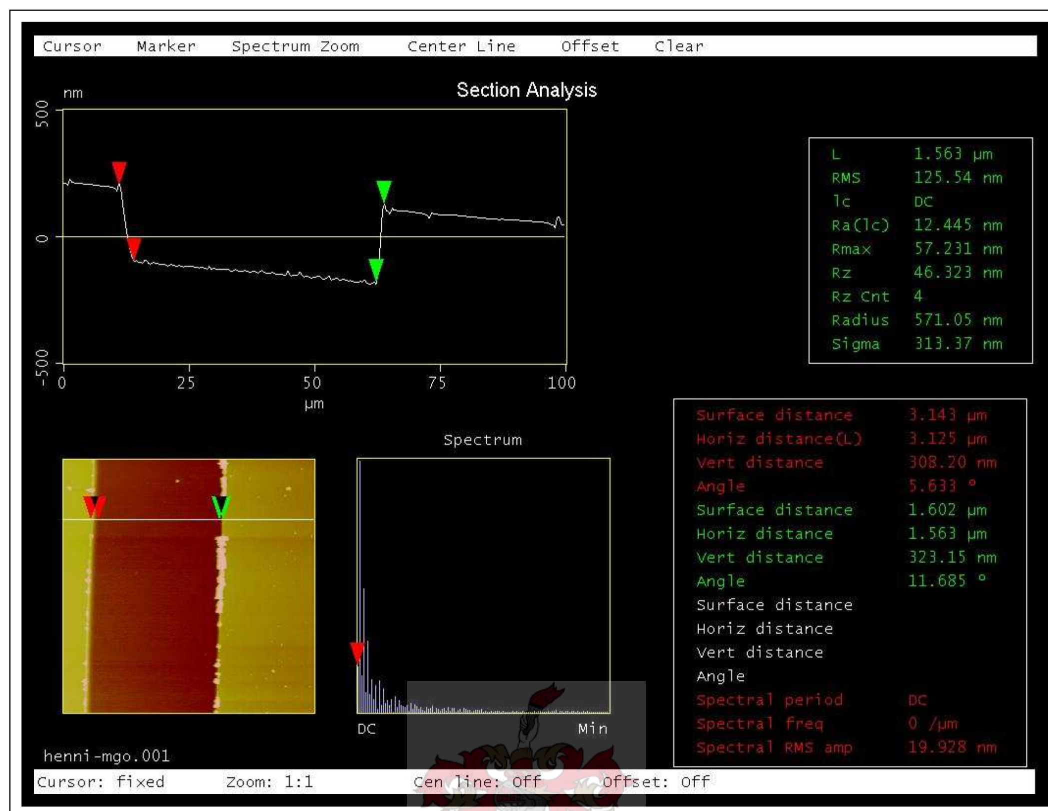

Figure 6.3: AFM image of CeO_2 test trench

6.4 Summary

A basic overview of the thin film patterning process has been given. Ultraviolet photolithography has been outlined followed by argon ion milling. Etching uniformity was improved using a multi-aperture extraction grid system. Etch rates on CeO_2 and YBCO were determined for a given set of milling parameters to be used later during device fabrication.

Chapter 7

Device Fabrication

7.1 Introduction

In order to demonstrate the workability of bi-epitaxy using the improved processes already discussed, it was decided to make a device similar to that of Petersen *et al* [28] utilising an MgO substrate. This device employs a single seed layer of CeO_2 to produce the required grain boundary. The process has been described conceptually in Section 3.7.3.

As already discussed, CeO_2 growth on MgO presents some difficulties. It is however possible to produce a proof-of-concept device using this method in order to demonstrate the feasibility of the manufacturing process and the functionality of the test setup[1]. Performance and reproducibility can then be improved by the addition of an YSZ buffer layer under the seed layer.

7.2 Seed Layer Deposition

The first step in the fabrication process is the deposition of the seed layer, in this case CeO_2. As stated previously, the seed layer should be extremely thin, on the order of

[1]The lack of an YSZ target at the time of prototype manufacture necessitated this compromise.

20 nm. Furthermore, we require that the surface should be as free from particulates as possible so as to provide a good template for YBCO growth and the subsequent grain boundary.

To achieve these ends, a shadow mask is used during the deposition process. This eliminates most particulates, leaving a relatively boulderless thin-film. Since the shadow mask also drastically reduces the deposition rate, allowing the growth of extremely thin layers, this is an ideal way of meeting the required specifications.

The seed layer was deposited using a pulsed oxygen source and a shadow mask. This run corresponds to sample P1 in Table 5.3. The setup employed has already been discussed in Chapter 5. The deposition parameters are restated in Table 7.1 for convenience.

CeO_2 PLD with Pulsed Oxygen Source

Laser Parameters:	
Laser Energy	14.3 J/cm^2
Spot Dimensions	4×0.7 mm^2
Pulse Frequency	16 Hz

Deposition Conditions:	
Deposition Temperature	740 °C
Deposition Time	30 min
Average Oxygen Pressure	0.1 mbar

Deposition Geometry:	
Target-Substrate Distance	74 mm
Valve-Substrate Distance	72 mm
Valve-Target Distance	65 mm
Shadow Mask	Yes

Table 7.1: CeO_2 deposition parameters (sample P1)

7.2.1 Optical Inspection

After deposition, visual inspection of the sample suggested that the layer was very thin. The sample also appeared to be uniform, with no visible irregularities. An image of the film obtained with optical microscopy is shown in Figure 7.1. The film was extremely reflective, as can be seen from the intensity of the image. Note the near absence of macroscopic particulates.

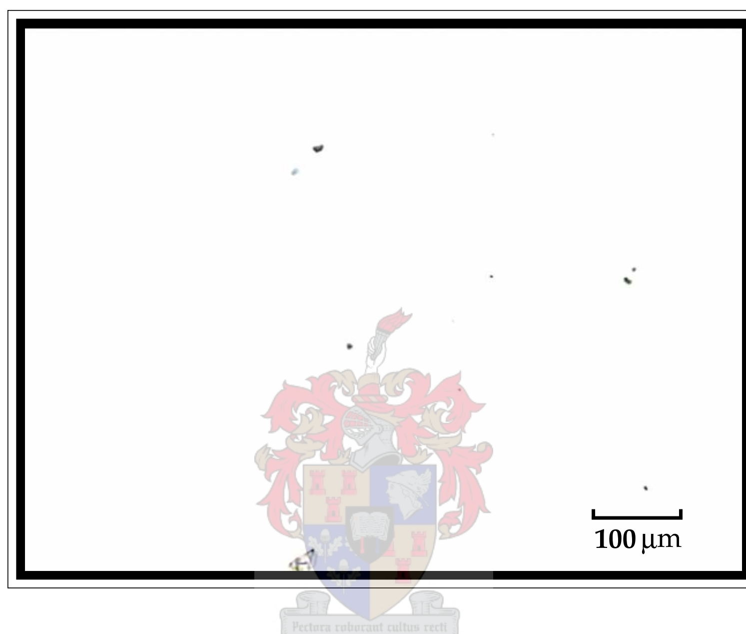

Figure 7.1: Post-deposition seed layer surface

7.2.2 Layer Crystallinity

In terms of crystallinity, the deposited thin-film represents one of the best CeO_2 layers deposited directly on MgO during the course of this work.

A powder diffraction pattern was obtained, shown in Figure 7.2. Accounting for a noise background of about 1 cps, the pattern has a sharp (100)-peak in the region of 25 cps, with a small, indistinct (111)-peak very close to the noise floor of the measurement. This shows that the desired (100)-growth dominates, with (111)-growth accounting for a very small fraction of the sample.

The preceding results suggest the good quality of the seed layer. The deposition was followed by the patterning of the thin-film, which is discussed next.

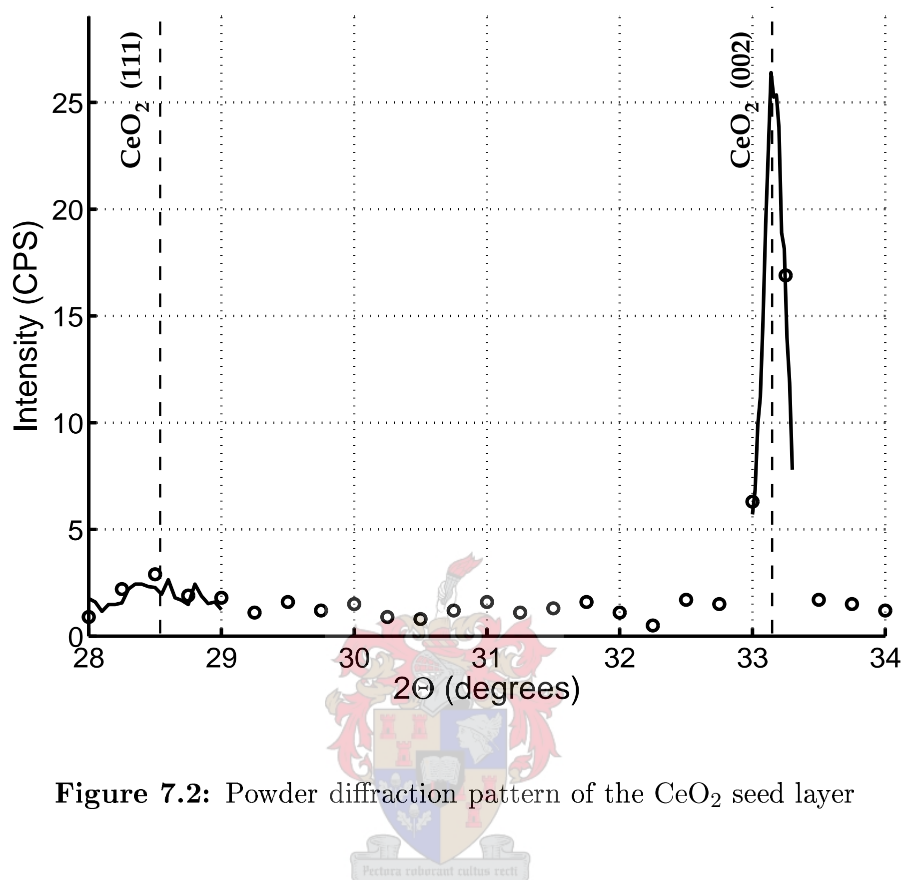

Figure 7.2: Powder diffraction pattern of the CeO_2 seed layer

7.3 Seed Layer Patterning

In this step, the seed layer is selectively removed from the sample surface in order to define the places where grain boundaries will form. For this device, a grain boundary must be formed along the middle of the sample. Therefore, the seed layer on one side of the substrate must be removed. In order to achieve this, a mask which leaves half of the substrate open and the other half covered during UV exposure is required.

Because no such mask was available, some improvisation was necessary to produce a suitable photoresist mask. It was realised that one of the step-edge masks designed by Snetler [32] could be used to create a usable resist pattern. By employing the step-edge line as an alignment marker, a large rectangular region of the substrate could be exposed, with

one side of the rectangle lying close enough to the substrate centre for easy subsequent alignment with the device mask pattern. Figure 7.3 illustrates this configuration with the sample outline superimposed on the step-edge mask.

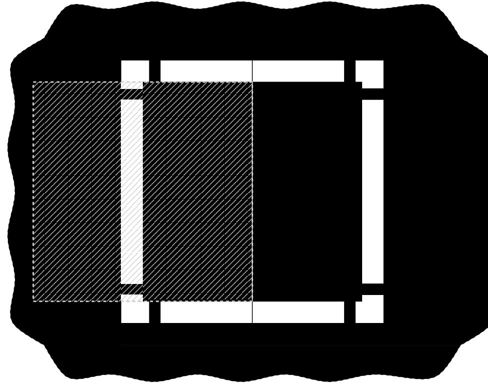

Figure 7.3: Sample outline on step-edge mask by Snetler [32] for seed layer photomasking

This method holds the disadvantage that an additional grain boundary is formed on the other side of the rectangular region. However, this grain boundary will only cross very wide lines of YBCO, leading to very high critical currents for the junctions so formed. These high critical current junctions will not be easily observable in conditions of zero magnetic field. Therefore we can ignore them for the purposes of extracting I(V) curves and Shapiro steps. The extra grain boundary will however affect the critical current modulation due to an externally applied magnetic field and we shall return to this at the appropriate time.

The parameters used to create the photoresist layer are given in Table 7.2. Rohm and Haas SPR 700-1.8 photoresist was used, along with the accompanying MF-24A developer. Optical microscopy was used to verify the quality of the photoresist mask. Figure 7.4 demonstrates that the process produced good results.

Argon ion milling was used to etch the sample as outlined in Chapter 6. It was decided to mill the sample for an extended period of time so as to ensure that all the CeO_2 is removed from the exposed region. This incurred some risk of producing low angle step-edge junctions (recall that the test etch of CeO_2 produced a step angle of 12°). Nevertheless, later critical current modulation results suggested that the correct junction type was formed. The parameters used during the etch process are given in Table 7.3. A picture taken of the region boundary after etching is given in Figure 7.5.

Photomasking Procedure

Step Description	Duration	Parameters
Resist Spin-on	60 s	4500 rpm
Soft bake	65 s	115 °C
UV Exposure	20 s	
Development	50 s	
Hard bake	10 min	100 °C

Table 7.2: Photoresist parameters for seed layer patterning

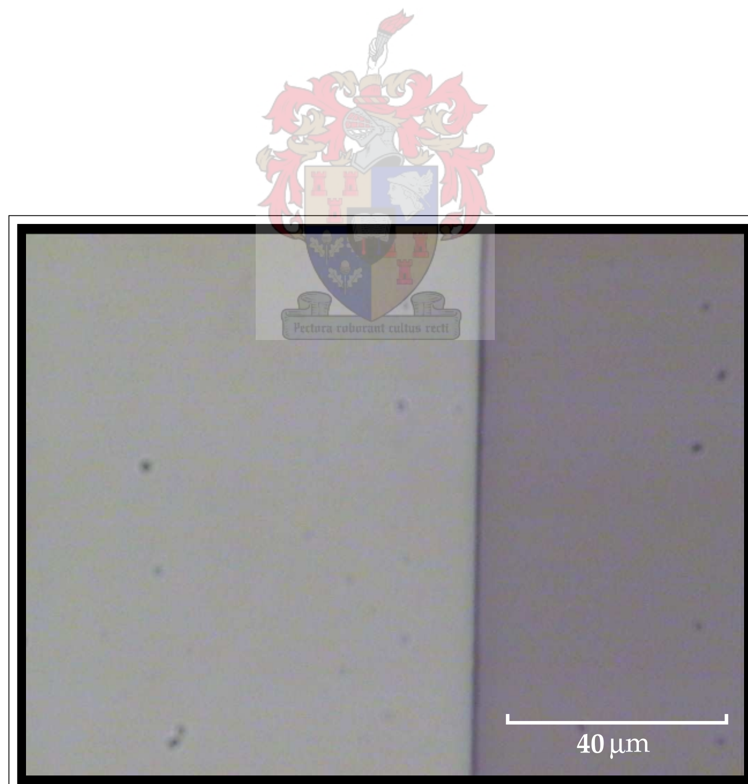

Figure 7.4: Photoresist mask for the boundary (white region is CeO_2)

Argon Ion Milling

Parameter	Value
Sample Angle	45°
Working Distance	100 mm
Milling Time	40 min
Base Pressure	4×10^{-5} mbar
Working Pressure	2.5×10^{-4} mbar
RF Power	40 W
V^-	V^+
2 kV	1.5 kV
I^-	I^+
3 mA	3.6 mA

Table 7.3: Seed layer milling parameters

Pectora roborant cultus recti

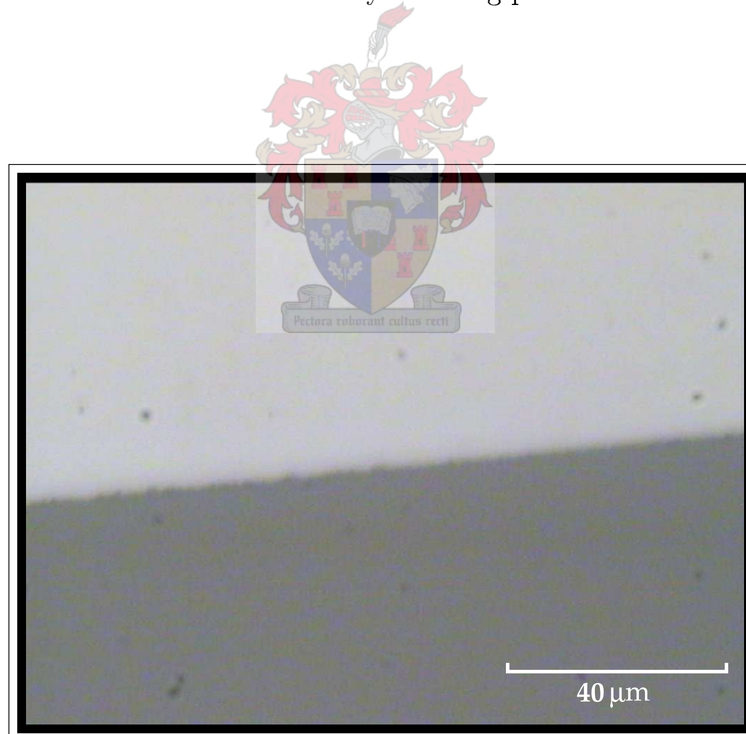

Figure 7.5: Post-mill device surface (dark region is the milled area)

7.4 YBCO Deposition

The next step in the process is the deposition of the superconducting thin-film. A pulsed oxygen source was again utilised during the PLD of the YBCO. The deposition parameters are given in Table 7.4.

A shadow mask was not utilised because of concerns surrounding potential deviations from the correct stoichiometry. This can occur because YBCO is a multicomponent material. Certain of the ablation plume species are heavier than others and are therefore less easily diverted from their trajectories by collisions. This renders them less likely to be scattered into the shadowed region. This can cause changes in the ratio of deposited species [33]. Therefore it was decided as a matter of caution not to use the shadow mask for this run.

YBCO PLD with Pulsed Oxygen Source

Laser Parameters:	
Laser Energy	13 J/cm^2
Spot Dimensions	4×0.7 mm^2
Pulse Frequency	12 Hz

Deposition Conditions:	
Deposition Temperature	725 °C
Deposition Time	20 min
Average Oxygen Pressure	6×10^{-2} mbar
Anneal Temperature	500 °C
Anneal Time	30 min

Deposition Geometry:	
Target-Substrate Distance	76 mm
Valve-Substrate Distance	76 mm
Valve-Target Distance	64 mm
Shadow Mask	No

Table 7.4: YBCO deposition parameters

Inspection of the sample, using optical microscopy, reveals differences in the YBCO growth in the two adjacent regions (see Figure 7.6). The boundary between the two regions is

clearly defined, suggesting the success of the process to this point.

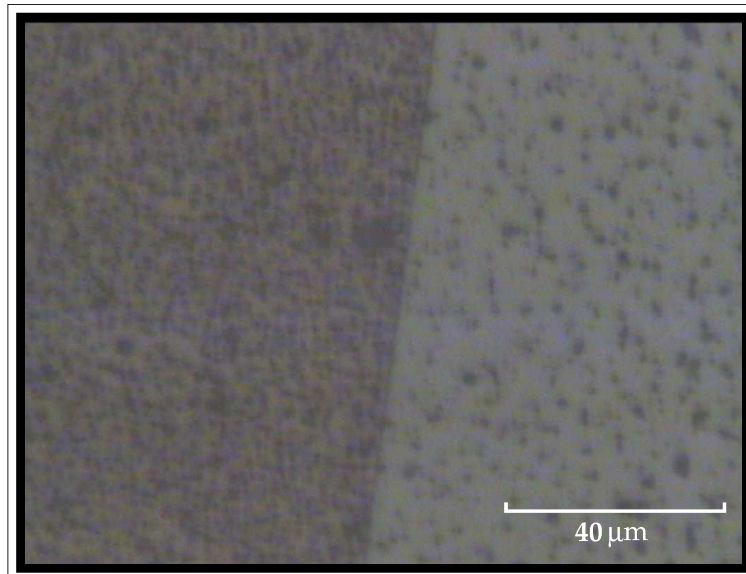

Figure 7.6: Grain boundary after YBCO deposition (dark region is YBCO on CeO_2)

A susceptibility test was performed on the thin-film to check for superconductivity. Figure 7.7 shows the transition curve for the sample. The onset of superconductivity is observed at 80 K, but the curve has a slow transition. The sample becomes more or less fully superconductive at 60 K (note that the unit produces measurements of around 20 % for superconducting films). Although this transition is not very good, superconductivity is still achieved and we can proceed, keeping in mind that the resulting junctions will have correspondingly lower T_c values.

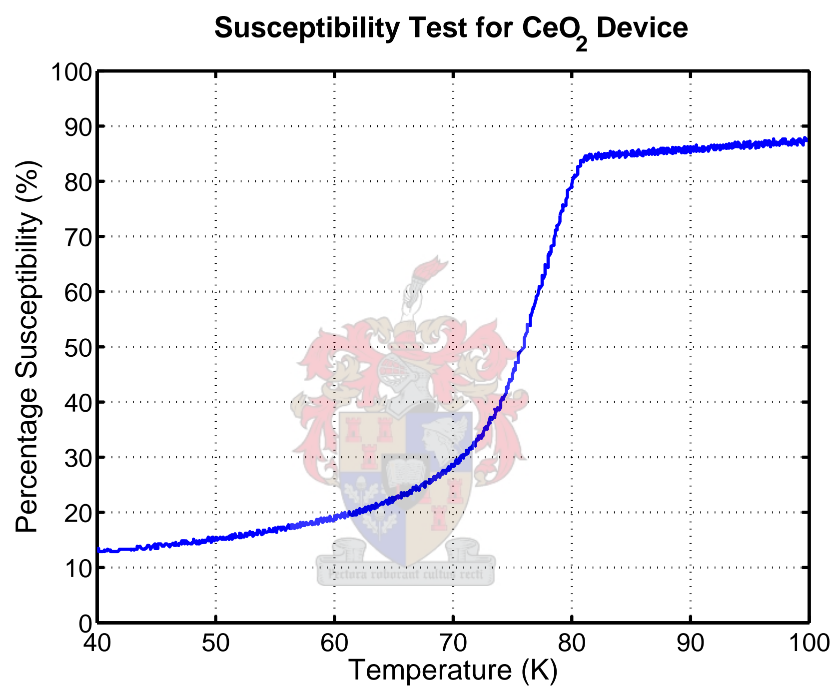

Figure 7.7: Susceptibility test for the YBCO thin-film

7.5 YBCO Patterning

YBCO patterning is very similar to the patterning of the seed layer. A different mask is used which contains the test pattern designed by Snetler [32] as shown in Figure 7.8. This mask defines a set of junctions with widths between 4 μm and 10 μm.

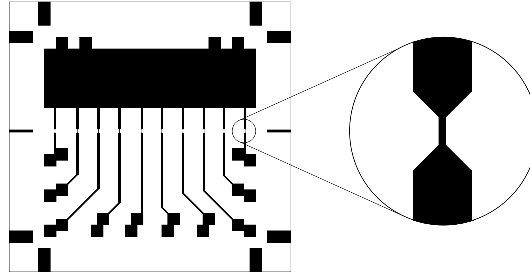

Figure 7.8: Device mask designed by Snetler [32]

Figure 7.9 shows the numbers assigned to each of the device legs for reference in the work that follows. The two center legs are the narrowest, with widths of 4 μm each. The legs become progressively wider towards the outside of the device.

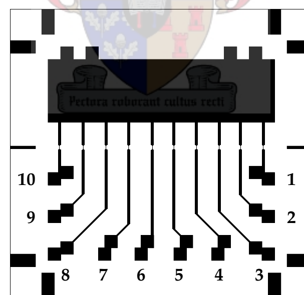

Figure 7.9: Leg numbering convention

It was found that photoresist on YBCO, with its dark and less reflective surface, requires slightly longer UV exposure. Therefore, an additional 3 seconds were added to the exposure time. All other parameters remained the same. The parameters used are listed in Table 7.5. Figure 7.10 shows the resulting photoresist mask on the YBCO layer with the junction legs crossing the grain boundary as required.

Photomasking Procedure

Step Description	Duration	Parameters
Resist Spin-on	60 s	4500 rpm
Soft bake	65 s	115 °C
UV Exposure	23 s	
Development	50 s	
Hard bake	10 min	100 °C

Table 7.5: Photoresist parameters for YBCO patterning

The sample was milled in a fashion similar to the way in which the seed layer was milled, but with the sample placed horizontally so that all the resulting YBCO sidewall angles will be equal. The sample was initially milled for 30 minutes, then checked at 10 minute intervals until the unwanted YBCO was completely removed. The relevant parameters are shown in Table 7.6.

Argon Ion Milling

Sample Angle	0°
Working Distance	100 mm
Milling Time	60 min
Base Pressure	4×10^{-5} mbar
Working Pressure	2.5×10^{-4} mbar
RF Power	40 W
V^-	V^+
2 kV	1.5 kV
I^-	I^+
3 mA	3.6 mA

Table 7.6: YBCO milling parameters

The resulting patterned YBCO is shown in Figure 7.11. Comparing the image with that of the photoresist mask, we see that the width of the photoresist line (in Figure 7.10) and the width of the resulting YBCO line appear close. The line edges also appear to be well defined. The unprotected YBCO has been completely removed (excluding the small resistant granules visible in the photos). It is clear that the etch process has produced good results.

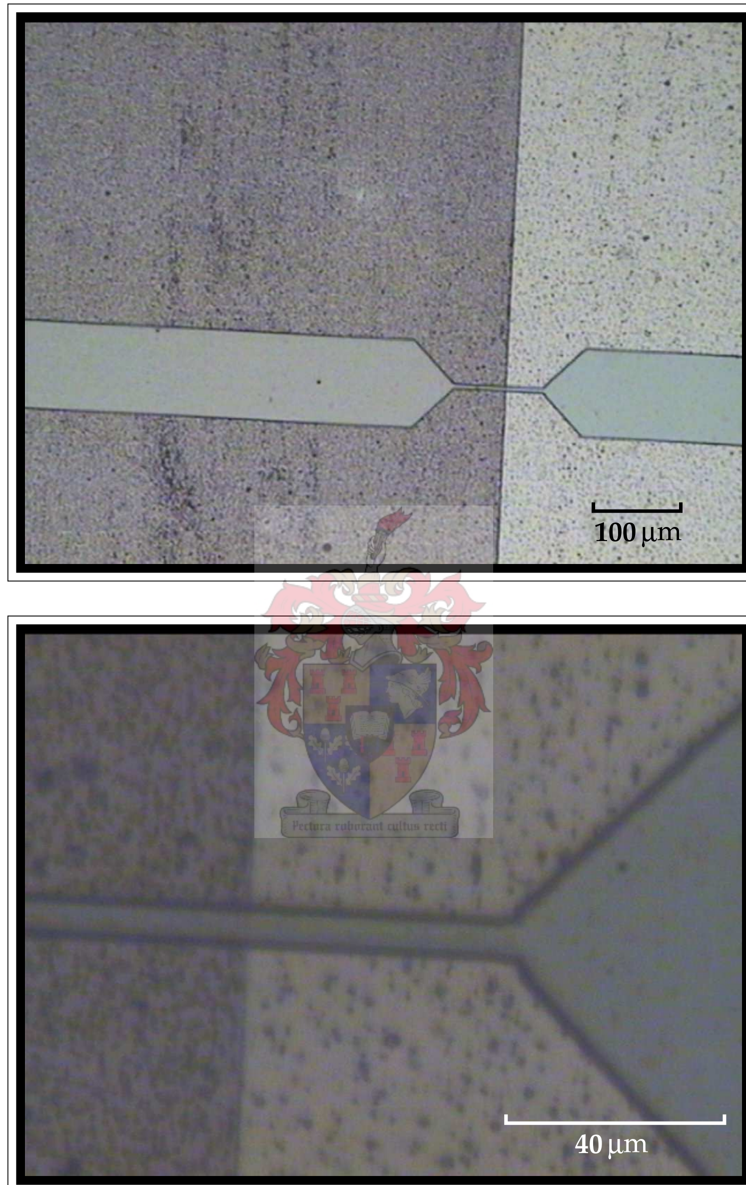

Figure 7.10: Photoresist pattern showing leg 4 (dark region is YBCO on CeO_2)

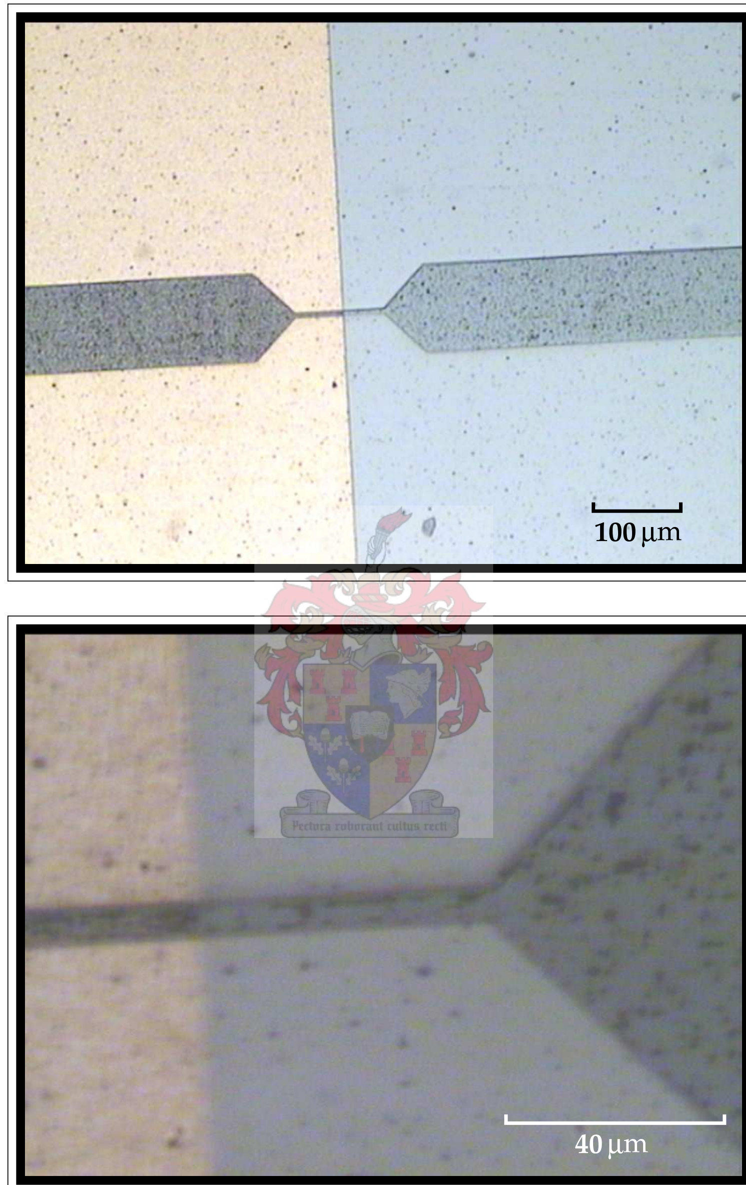

Figure 7.11: Patterned YBCO showing leg 4 (yellow region is CeO_2)

7.6 Gold Pads and Wirebonding

With the device fabricated, connections must be made to the contact pads so that tests can be performed. The sample needs to be mounted on a suitable test PCB, which must provide electrical contacts to which external equipment can be connected. The contact pads of the sample must also be connected to the test PCB. In general, this is performed by bonding extremely thin gold wire ultrasonically onto the device's contact pads and connecting them with the metallised tracks on the test PCB.

Wirebonding of gold wire cannot be done directly onto YBCO. Instead, it is necessary to prepare the contact pads by metallising them with either silver or gold [35]. In this work, contact pad metallisation was performed by the PLD of gold through a mask with holes which define the pad locations. The PLD parameters used during the metallisation process are listed in Table 7.7.

Gold PLD with Ambient Oxygen

Laser Parameters:	
Laser Energy	13 J/cm^2
Pulse Frequency	15 Hz
Deposition Conditions:	
Substrate Temperature	430 °C
Deposition Time	45 min
Ambient Oxygen Pressure	5×10^{-2} mbar
Deposition Geometry:	
Target-Substrate Distance	76 mm

Table 7.7: Gold deposition parameters

Earlier attempts at pad metallisation involved the deposition of gold at temperatures ranging from room temperature up to 350 °C. Wirebonding failed, or was unreliable, for each of these samples. The resulting pads only became usable when the deposition temperatures were on the order of 430 °C. Another important condition is the thickness of the pads, since

wirebonding fails if the gold pads are too thin. It was found that, for these parameters, a deposition of around 45 minutes resulted in pads of sufficient thickness.

Wirebonding was performed on the sample after mounting it on the test PCB. Because of limited connections available on the PCB, only legs 3 through 6 were bonded, along with the ground plane connections.

Figure 7.12 shows the result of the pad metallisation and wirebonding processes. The figure shows a single contact pad with four gold wires wirebonded to its surface.

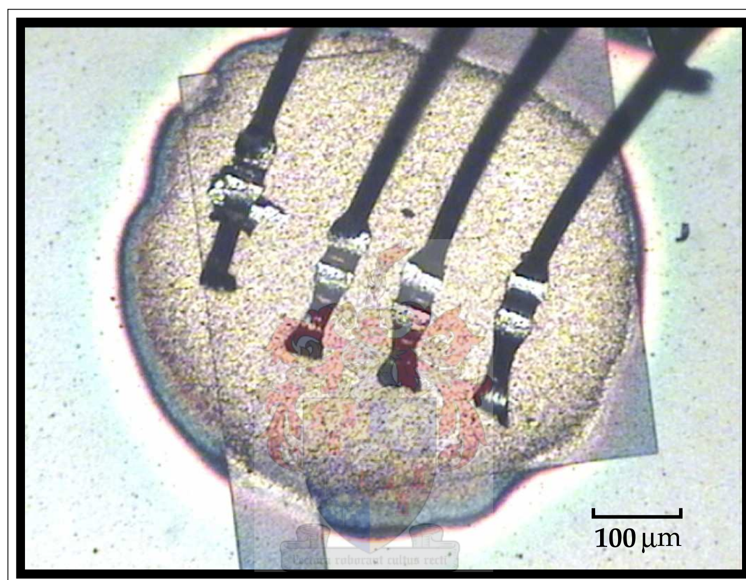

Figure 7.12: Gold pad with wirebonds

Having successfully completed the wirebonding, the device is now ready for testing. This will be discussed in the next chapter.

7.7 Summary

The fabrication of a bi-epitaxial test circuit using a CeO_2 thin-film as a seed layer has been demonstrated. The PLD of the seed layer was performed using a pulsed oxygen source. A shadow mask was used to decrease surface particulates. The seed layer was patterned

using argon ion milling. YBCO was deposited on the sample using PLD. Inspection of the sample, using an optical microscope, revealed a well defined boundary between the regions with and without the seed layer. Argon ion milling was employed to pattern the YBCO layer into the test circuit. Optical microscope images reveal the good results of the etch process. Gold pad deposition was performed, followed by wirebonding to achieve contact with the test PCB.

An integrated fabrication process has been presented (the success of which is verified in the next chapter). Previous attempts at device manufacture at the University of Stellenbosch were unsuccessful for various reasons. The device discussed in this chapter represents one of the first to be created entirely locally.

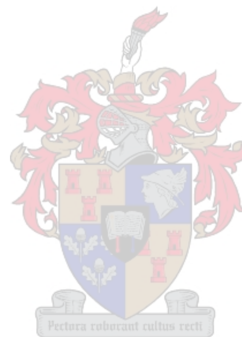

Chapter 8

Device-level Testing and Results

8.1 Introduction

Verifying device functionality is an indispensable part of the development cycle. Many challenges have to be overcome in order to find a test setup which delivers the required accuracy and repeatability. In this chapter the testing of the prototype device will be discussed along with the results obtained. The equipment setup for each of the tests will be considered.

There are three main measurement goals that need to be achieved. Firstly, the presence of the Josephson effect must be demonstrated. Secondly, the nature of the weak link must be investigated (whether or not the link is due to an asymmetric 45° grain boundary). Thirdly, simple parameter extraction must be done in order to obtain an idea of the junction performance.

A direct way of testing for the presence of the Josephson effect is the generation of Shapiro steps. This unambiguously demonstrates the AC Josephson effect. A prerequisite for this test is a normal I(V) curve, which will be obtained first in Section 8.2 before proceeding to Section 8.3 where the AC Josephson effect is investigated.

Once the Josephson effect has been demonstrated, the nature of the weak link must be

Pectora roborant cultus recti

determined. Fortunately, asymmetric 45° grain boundaries demonstrate anomalous critical current modulation in the presence of magnetic fields. Section 8.4 will search for these telltale indications.

Simple parameter extraction will be performed. Parameters considered will include the critical current (I_c), normal state resistance (R_n) as well as the temperature and magnetic field dependencies of the former.

8.2 I(V) Characteristics

8.2.1 Test Setup

In order to measure the I(V) characteristics of the Josephson junctions, they are driven by a low-noise constant current source. The voltage generated by the device is then amplified for display on an oscilloscope. By combining the applied signal and the returned signal in an X-Y plot, the I(V) characteristic of the junctions can be displayed.

The unit containing the current source and amplifier used to perform these measurements was manufactured by Conductus to accompany a SQUID demonstration kit [17]. Since the unit was intended to test SQUIDs which were manufactured using bi-epitaxy, it is ideal for this purpose. The unit is battery operated and therefore adds very little to the ambient environmental noise in the laboratory.

Pectora roborant cultus recti

Unfortunately, the environment in which the measurements were performed was itself extremely noisy. The lack of adequate mu-metal shielding also had a detrimental effect. As a result, flux trapping effects were observed during testing, leading to changes in the measured critical currents. The resulting uncertainty should therefore be stated at the outset. The test setup will have to be refined in order to perform more accurate measurements.

In performing measurements of the critical current, a criterion must be defined for the transition to the normal state. For the purposes of the results presented in this chapter, a voltage of $2\,\mu$V was taken as indicative of the normal state. Note that the figures presented have different vertical scales from the ones used to measure critical current. This was done

for the sake of providing clean I(V) curves, since 2 μV is very close to the noise floor of the experiment.

8.2.2 Results

An I(V) curve, shown in Figure 8.1, was obtained at 42 K for leg 4 of the production device. This curve can be used to extract the critical current and normal state resistance of the junction. The curve shows that the device has a critical current of about 150 μA. In order to obtain the normal state resistance R_n, the DC current offset was adjusted so as to reveal the normal region of the I(V) curve. From the slope of the curve, a value of approximately 0.67 Ω was obtained. From these two values, we find that the I_cR_n product of the junction at 42 K is 0.1 mV.

The critical current was measured as a function of temperature. The results of these measurements are plotted in Figure 8.2. The plot suggests that the critical current has a linear dependence with respect to temperature, with a critical temperature of 60 K and a critical current of 160 μA at 40 K.

Pectora roborant cultus recti

Leg 6 was also tested (the measurements for leg 6 are presented in Appendix C). The I(V) curve for this leg (shown in Figure C.1) exhibits a critical current of 300 μA and a normal state resistance of approximately 1.5 Ω. This gives an I_cR_n product of 0.45 mV for this junction. The critical current was plotted against temperature in Figure C.2. The data implies a linear dependence of the critical current on temperature. The junction was more sensitive to flux trapping, possibly because of its smaller width. This caused large variations in the apparent critical current (the values given here represent the maximum values obtained). For this reason, the results of leg 4 are presented in the main body of this text, since this leg was less affected by flux trapping.

The I_cR_n values obtained (0.1 mV and 0.45 mV) compare well with those obtained for similar junctions found in the literature. When considering CeO_2 single seed layer devices, Petersen *et al* [28] reported an I_cR_n product of 0.1 mV at 30 K. Yang *et al* [39] reported an I_cR_n product of 0.056 mV at 20 K. Therefore, in relation to this figure of merit, the tested junctions appear to be better than their counterparts in the literature.

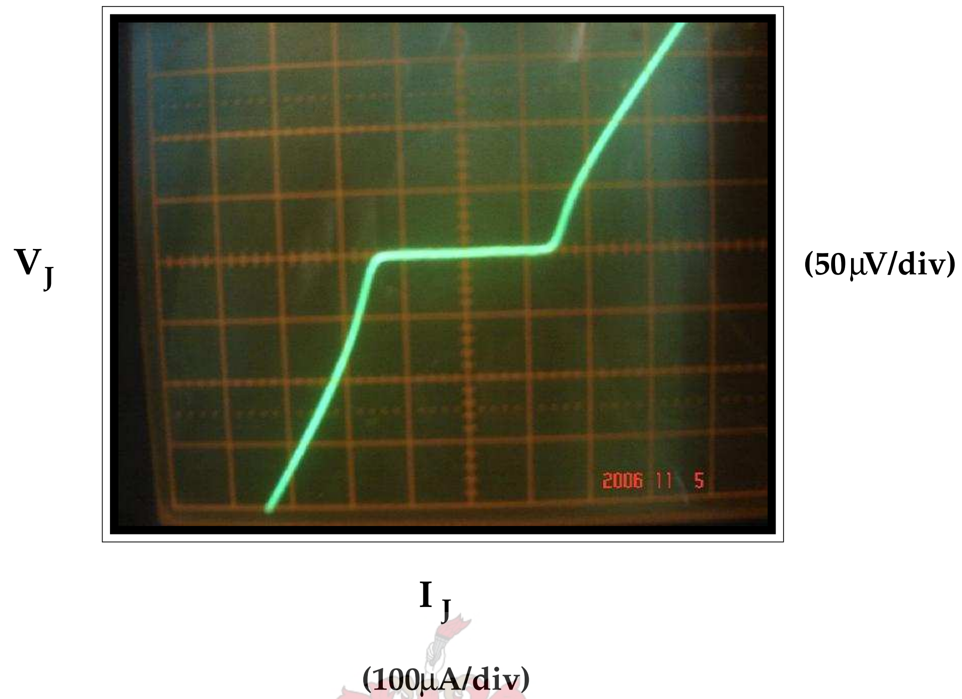

Figure 8.1: I(V) curve for leg 4 of the prototype (T=42 K)

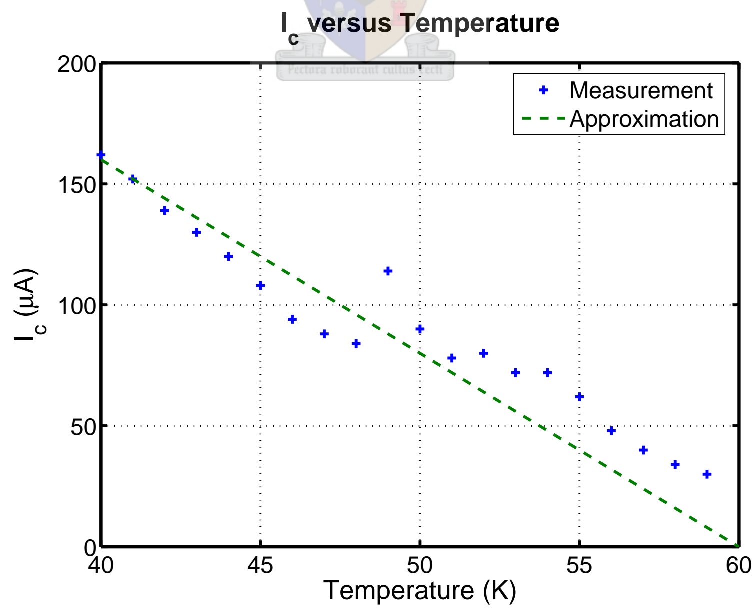

Figure 8.2: Critical current versus temperature for leg 4

8.3 AC Josephson Effect

Unfortunately the observation of a superconducting transition in the I(V) curve is not enough to verify without doubt the presence of the Josephson effect, since normal superconducting strips also have such a transition. Although the shape of the I(V) curves obtained strongly suggest the Josephson effect (note the characteristic "knee" at the transition to the normal state), a stronger test is needed to provide proof of its presence.

The AC Josephson effect is a clearcut way of demonstrating the existence of a Josephson junction since the stair-step behaviour of the I(V) curves under microwave irradiation is unique to these devices.

8.3.1 Test Setup

In order to observe the AC Josephson effect, RF power at frequencies exceeding 1 GHz has to be coupled into the junction. This was done by placing a simple wire loop antenna above the sample inside the cryocooler. The wire loop is connected to an external RF power source via an SMA cable. The RF power source used was an HP 8671B synthesised CW generator with an output frequency range of 2 to 18 GHz.

8.3.2 Results

Using this setup, an I(V) curve showing Shapiro steps was obtained for leg 4 at an RF power frequency of 18.09 GHz as shown in Figure 8.3 (the Shapiro steps obtained for leg 6 are shown in Figure C.3). The output power of the source was approximately -10 dBm. We can see that the steps are well-defined, with even the 4th order steps still discernable.

From the figure, we note that the 4th order step in the negative voltage regime is at $-150\,\mu$V (the third division below ground). Recalling the formula for the step height from (2.5.5), we have

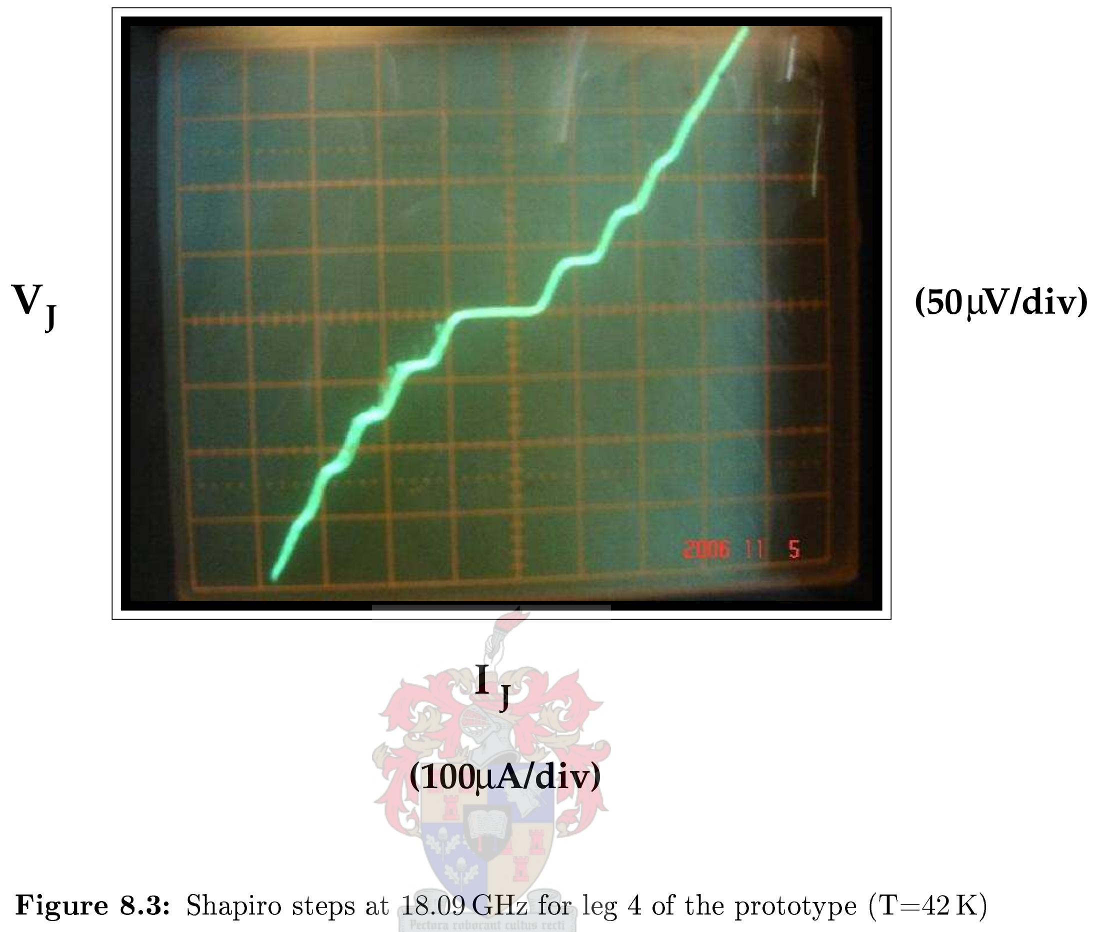

Figure 8.3: Shapiro steps at 18.09 GHz for leg 4 of the prototype (T=42 K)

$$V_0 = n\frac{\Phi_0}{2\pi}\omega_s. \tag{8.3.1}$$

We can rewrite this equation to obtain an expression for Φ_0

$$\Phi_0 = \frac{V_0}{nf}. \tag{8.3.2}$$

Given that we know the value of Φ_0 ($2.07\times10^{-15}\,\mathrm{T\cdot m^2}$), we can use this expression to verify the accuracy of our measurement. Taking $V_0 = -150\,\mu\mathrm{V}$, $n = -4$ and $f = 18.09\,\mathrm{GHz}$, we obtain

$$\Phi_0 = \frac{V_0}{nf} \approx \frac{-150 \times 10^{-6}}{-4 \times 18.09 \times 10^9} = 2.073{\times}10^{-15}\,\mathrm{T{\cdot}m^2}. \tag{8.3.3}$$

This value is extremely close to the theoretical value, differing by only 0.15 %. The presence of Shapiro steps and the excellent agreement with theoretical predictions provide clear evidence of the Josephson effect.

8.4 Critical Current Modulation

To investigate the nature of the weak link, we now proceed by investigating the behaviour of the junction under the application of an external magnetic field.

8.4.1 Test Setup

To measure to effect of an applied DC magnetic field, a Helmholtz coil was added to the test setup. The coil provides a magnetic flux density oriented from the surface of the thin film down towards the substrate (consistent with the geometry presented in Section 2.6).

A Helmholtz coil consists of a coil pair with equal radii. The coils are separated by a distance equal to their radius. In the setup used during this work, each coil in the pair consisted of 20 turns. The outer diameter of the coils was 31 cm, with the inner diameter being 29 cm. From (D.1.4) in Appendix D, the theoretical value for the magnetic field density at the centre of the coil is given by

$$B = \left(\frac{4}{5}\right)^{\frac{3}{2}} \frac{\mu_0 n I}{R} \tag{8.4.1}$$

Where μ_0 is the permeability of free space, n is the number of turns in each coil, I is the current and R is the average radius of the coil turns. Using this equation we can obtain a prediction of the generated field.

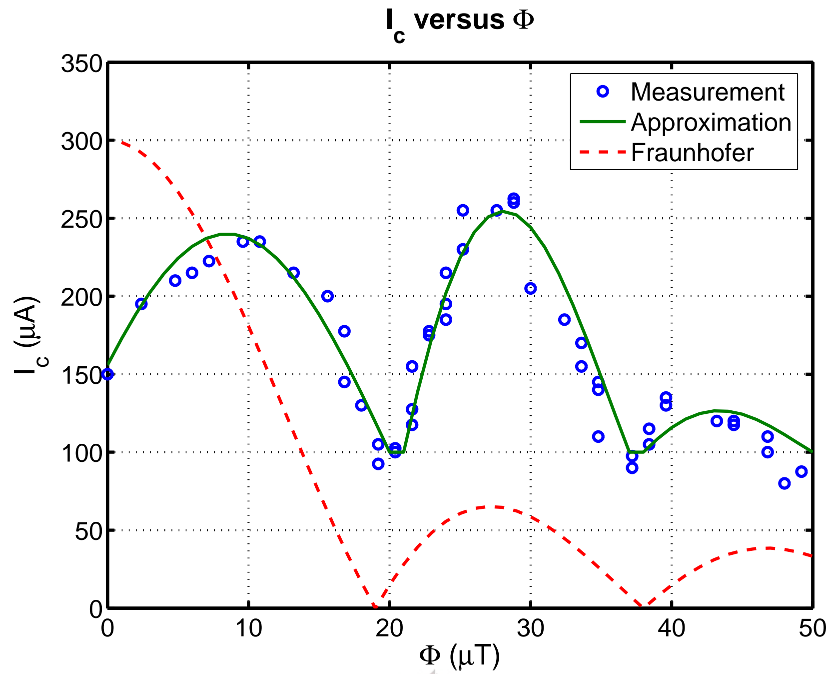

Figure 8.4: Critical current modulation for leg 4

$$\frac{B}{I} = \left(\frac{4}{5}\right)^{\frac{3}{2}} \frac{4\pi \times 10^{-7} \times 20}{0.15} = 120\,\mu\mathrm{T/A} \tag{8.4.2}$$

This value was used in converting the values for the current applied to the coils into values for the applied magnetic flux. Using this setup the effects of an applied magnetic field were studied as described in the following section.

8.4.2 Results

Critical current modulation measurements were performed on leg 4. The results of the measurements are shown in Figure 8.4. We can clearly see evidence of critical current suppression with increasing magnetic field.

The figure shows two possible approximations to the data. The dashed line represents a fit to the Fraunhofer modulation pattern as discussed in Section 2.6. A null periodicity of

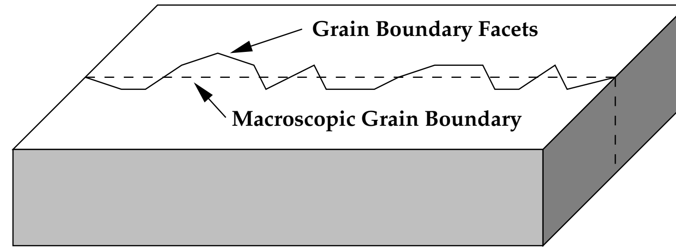

Figure 8.5: Illustration of grain boundary faceting

19 μT was assumed. A further hand-fitted curve shown by the solid line is also provided.

It is easily observed that the Fraunhofer pattern is a poor fit for the data. Although the data does suggest null periodicity similar to that found in Fraunhofer modulation, the peak magnitudes are very inconsistent. However, this type of behaviour is well known for 45° asymmetric grain boundaries, as will be discussed below.

For 45° asymmetric grain boundaries, we find that grain boundary faceting causes non-Fraunhofer type modulation patterns [10, 15]. Grain boundary faceting refers to the meandering of the true grain boundary about the macroscopic grain boundary plane as illustrated in Figure 8.5. This leads to a situation where the angle with which two neighbouring grains meet changes according to the local direction of the grain boundary.

In a superconductor with an isotropic (s-wave) superconducting order parameter, this would have little effect. However, YBCO exhibits strong evidence of d-wave symmetry. Since the order parameter now has an angular dependence, the changing angle with which the grains meet causes corresponding changes in the critical current. Because the critical current varies from facet to facet, the critical current density $J_c(\mathbf{r})$ is itself inhomogeneous. This causes large deviations from Fraunhofer modulation, which requires small[1] and spatially homogeneous Josephson junctions [15].

Increased misorientation angle leads to critical current modulation which deviates greatly from the normal Fraunhofer pattern. The data presented in Figure 8.4 agrees well with

[1]Recall from Section 7.3 that there is also a long grain boundary junction present in series with the smaller junction. Since the long junction encloses more flux, we expect its behaviour to dominate when the magnetic field is non-zero. Although one now expects some deviation from Fraunhofer modulation, key properties still hold in the case of an unfaceted boundary, such as a global critical current maximum at zero field and decreasing peak magnitudes in the modulation pattern with increasing field [27].

Pectora roborant cultus recti

this phenomenon, sharing key aspects of this type of behaviour. The most important agreement lies in the fact that the global maximum of the pattern does not occur at zero applied field [23]. Furthermore, successive maxima do not necessarily decrease in size as for the Fraunhofer pattern. It is easily observed from the data that the second maximum is at least as large as the first (if not greater). The fact that the minima are non-zero is also consistent with the inhomogeneity of boundaries of this type. These observations provide strong evidence for the presence of the desired 45° asymmetrical grain boundary.

8.5 Summary

In this chapter, working Josephson junctions each with a T_c of 60K were demonstrated. The critical currents obtained at 42K were $150\,\mu$A and $300\,\mu$A respectively with associated I_cR_n products of 0.1 mV and 0.45 mV. It was noted that the I_cR_n products are superior to similar devices found in the literature. Shapiro steps were observed, providing indisputable proof of the Josephson effect. Critical current modulation measurements show that the behaviour of the junctions are consistent with the intended 45° asymmetrical grain boundary. We can therefore conclude that the fabrication process was successful.

Contributions to the University of Stellenbosch high-T_c superconducting microelectronics project include:

- *Demonstration of test setup functionality.* The results presented in this chapter prove that simple measurements can be performed with the test equipment. The analyses also show that measurements of reasonable accuracy can be obtained in this way (particularly the Shapiro step measurement).
- *Additions to the test setup.* Previous test setups only included the I(V) curve measurement unit. Additions were made to the test setup in conjunction with other researchers [3, 36]. The additions include an RF source and wire loop antenna for AC Josephson effect measurements, as well as a coil setup to demonstrate critical current modulation effects. These additions have been shown to be both successful and valuable in providing additional information of the junction properties.

Pectora roborant cultus recti

- *Working Josephson junctions.* The junctions tested in this chapter represent some of the first to be fabricated at the University of Stellenbosch after many previous failed attempts. This is therefore an exciting step forward for the manufacturing program. A suitable foundation is now present for work on a reproducible process and, eventually, more complicated devices such as SQUIDs.

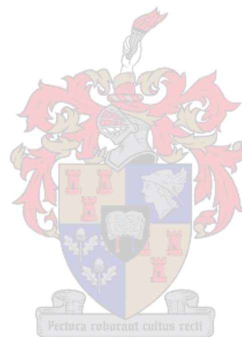

Chapter 9

Conclusions and Recommendations

9.1 Conclusion

In this thesis, issues relevant to the manufacture of bi-epitaxial grain boundary junctions have been explored. An overview of Josephson junction theory has been provided. The various types of high-T_c Josephson junctions have been described, with special attention being given to bi-epitaxial junctions. Epitaxy and texturing in thin-films have been described. X-ray powder diffraction was selected as a powerful tool for verifying the correct epitaxy of deposited thin-films. The PLD process was detailed. Shortcomings of the standard PLD configuration were stated. A pulsed oxygen source and a plate shadow mask were utilised to improve the quality of the resulting thin-films. Thin-film patterning was discussed, along with changes made to the local milling process to improve process uniformity. A prototype device was manufactured with a CeO_2 seed layer. The fabrication procedure was documented, showing the process in various stages of completion. The resulting device was tested for the DC and AC Josephson effects, as well as critical current modulation under the application of a magnetic field. It was shown that the prototype exhibits behaviour consistent with similar devices found in the literature, demonstrating the success of the process.

Contributions made to local efforts to manufacture high-T_c Josephson junctions include:

- *A new direction.* Previous attempts at creating high-T_c Josephson junctions at the University of Stellenbosch were unsuccessful. This past research attempted the fabrication of bicrystal and step-edge junctions. Bi-epitaxy was identified as a simple and relatively inexpensive alternative to these processes, which succeeded where the other attempts had failed.

- *Increased PLD uniformity.* The increased working distances and the addition of a plate shadow mask allowed the PLD to produce films of higher quality. This was essential to the success of this work, since the seed layer must be of good quality if it is to serve as a growth template for subsequent YBCO deposition.

- *Deposition of new dielectric materials.* CeO_2 and YSZ are important and versatile buffer materials in the high-T_c superconductor field. Future researchers at the University of Stellenbosch can now utilise these materials for purposes which are not necessarily tied with bi-epitaxy. It was demonstrated that, for the bi-epitaxy process, a suitable seed layer can be manufactured locally using a combination of CeO_2 and YSZ.

- *Improved uniformity of the argon ion mill.* The researcher contributed towards the implementation of a multi-aperture set of ion extraction grids which improved the uniformity of the argon ion mill.

- *An integrated fabrication process.* The entire fabrication process for the prototype has been documented, allowing similar devices to be made in the future. This contributes towards the future implementation of practical devices such as SQUIDs.

- *Working Josephson junctions.* The junctions in the prototype represent some of the first high-T_c Josephson junctions to be manufactured at the University of Stellenbosch. This is in itself an enormous step forward, allowing future researchers to improve on a now functioning process.

- *Extended test setup.* Previous researchers at the University of Stellenbosch only tested for the DC Josephson effect. These tests failed, but even their success could still have been construed as ambiguous. In conjunction with other researchers, testing for the AC Josephson effect and critical current modulation were added to the ensemble of

experimental techniques available to future workers, which will prove invaluable in verifying device functionality.

The original aim of this thesis was to provide a proof-of-concept manufacturing process for the local manufacture of high-T_c Josephson junctions. Given the previously stated contributions, it can be concluded that the work was successful in achieving this end. This provides a strong foundation for an improved process, or other processes if the work is suitably adapted.

9.2 Recommendations

A large amount of time during the course of this research was spent towards the production of simple, but functioning, devices. Having successfully achieved this aim in the form of a working prototype, there remains a great amount of work to be done in order to make devices with practical applications. This section is dedicated to outlining areas for future research. Many of the aspects addressed in this section are also critical for processes which are not necessarily based on bi-epitaxy.

- *Prototype using a combined CeO_2 and YSZ seed layer.* Because of funding constraints at the Laser Research Institute (LRI), the excimer laser could not be given a much needed gas charge. The laser energy was too poor to deposit the YBCO layers necessary for further device production. Immediate extentions of this work should test the effect of using a combined CeO_2 and YSZ seed layer. If successful, the properties of the resulting junctions should be more reproducible in terms of seed layer epitaxy, as implied by the earlier X-ray diffraction results.
- *Film thickness measurement.* It is critical that a way be found to measure film thicknesses locally. The method should preferably be non-destructive and it should be available for routine use. Thin-film thickness is a critical parameter. Specifically, bi-epitaxy requires that seed layers be as thin as possible to avoid step-edge junctions from forming. It is also important to be able to verify seed layer removal unambiguously after the etching process. YBCO thickness is another important parameter which must be determined. Ellipsometry is one candidate technique, although

YBCO's opaqueness makes this optical process less attractive. As a compromise, Rutherford Backscattering (RBS) may be used.

- *Microtexture analysis of grain boundaries.* Although the AC Josephson effect measurements confirm the presence of weak links in the prototype, and the critical current modulation measurements are consistent with the presence of 45° asymmetric grain boundary junctions, indisputable verification of this is obtainable using microtexture analysis techniques such as Electron Back-scatter Diffraction (EBSD). Also, since local efforts currently focus on grain boundary engineering, it would be sensible to be able to directly measure their presence.

  It is strongly suggested that access be obtained to such equipment. The researcher has provided a brief overview of the process in Appendix E in hopes of highlighting the important contribution this could make to production efforts.

- *Process reproducibility.* The focus of the work performed in this thesis was on producing working junctions. As such, emphasis was placed on the crystallinity of the thin-films. Systematic studies still have to be performed of, amongst others, film thickness and nanoscale roughness (that is, surface roughness in the absence of boulders). Furthermore, the fidelity of pattern transfer from the photolithographic mask to the device needs to be studied in detail. Although the methods employed in this work were sufficient to demonstrate functionality, a thorough investigation of these aspects needs to be performed in order to obtain reasonable and well-known parameter spreads.

- *Improvement or replacement of component processes.* Having established an integrated process, the influence of the improvement or replacement of component processes can be investigated. In particular, attention needs to be paid to the PLD process. This is the only part of the fabrication process that depends on equipment not belonging to the electronic engineering department (excluding the diagnostic equipment). As such, the work of other researchers sharing this equipment causes problems with reproducibility (since the setup is constantly being adjusted to meet the needs of other groups). There is also the real threat of contamination due to residue left by other deposition runs.

- *Improvement of the test setup.* The test setup needs to be improved in order to allow reliable measurements to be performed. Although the setup in its current state was

sufficient to verify the functionality of the prototype, much work remains to be done in order to minimise the noise to which devices are exposed during testing.

- *Practical device applications.* There now exists the real potential for practical device applications. The logical first step would be the implementation of a simple SQUID magnetometer. Many previous researchers at the University of Stellenbosch have investigated the requirements for such devices and have produced designs that may be workable [9, 30, 11]. The work in this thesis can be used to realise these previous design efforts. Since SQUID magnetometers are themselves very important in practice, this raises the exciting prospect of moving towards industry applications of the group knowledge base.

Apart from the ones presented here, there remains a rich set of possible avenues of exploration. It is the hope of the researcher that the knowledge that has been gained will be applied in future work to further improve the competitiveness of local workers with respect to the international research community.

Appendix A

Pulsed Valve Control

A.1 Timing generator

Figure A.1: Stanford Research Systems DG535

To generate the waveforms necessary for the triggering events, a Stanford Research Systems DG535 digital delay and pulse generator was employed (shown in Figure A.1). This unit

allows for the generation of two pulses of controllable duration seperated by a specified time delay. The system is controlled by setting 4 timing parameters A, B, C and D. These parameters can be set relative to the internal trigger, or relative to one of the preceding parameters. The system then generates both active high and active low TTL pulses for the AB and CD pairs respectively. Figure A.2 shows a timing diagram for the setup employed.

For our purposes, we have set A to be synchronous with the internal trigger, with B lagging A by 1 ms. This provides 1 ms pulses to trigger the pulsed valve driver unit. The output is taken from the active low AB output, since the driver unit is negative edge triggered.

We now set C to lag A by some value. This will be the delay between the triggering of the gas valve and the laser pulse. We also set D to lag C by 1 ms so that the generated pulses are 1 ms in duration. We utilise the active high CD output for the laser since it is positive edge triggered.

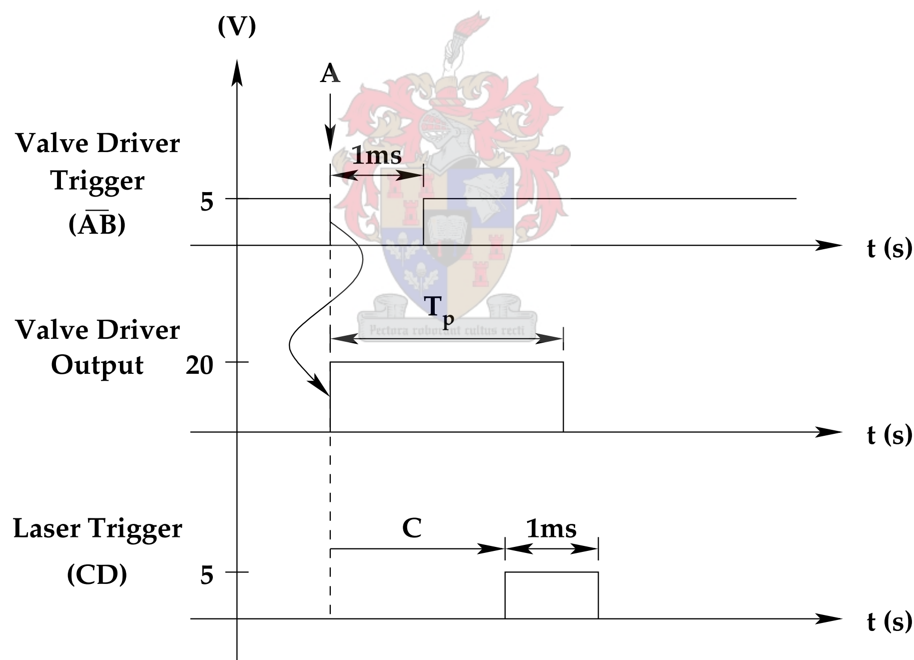

Figure A.2: Timing diagram for synchronisation setup

Figure A.3: Valve driver unit

A.2 Valve driver unit

Pectora roborant cultus recti

The valve driver unit employed (shown in Figure A.3) has the function of producing pulses of sufficient voltage (20V) to open and close the pulsed valve. It provides an input for external negative edge triggering.

The output pulse duration is set on an uncalibrated dial. To find the true pulse durations, the output pulses were measured using an oscilloscope and the results are listed in Table A.1 (note that the pulse duration range indicated on the unit itself is incorrect). The delay between the trigger event and the output going high was also measured and found to be negligable ($<10\,\mu$s). The output pulse duration can be approximated (using least-squares) by the second order polynomial

$$T_p = -0.010315s^2 - 0.095490s + 2.6339 \tag{A.2.1}$$

where T_p is the resulting pulse duration in milliseconds and s is the dial setting.

Dial Setting	Output Pulse Duration (ms)
0	2.65
1	2.55
2	2.4
3	2.2
4	2.05
5	1.9
6	1.7
7	1.5
8	1.25
9	0.95
10	0.6

Table A.1: Valve driver output pulse durations

Appendix B

X-ray Diffraction Results

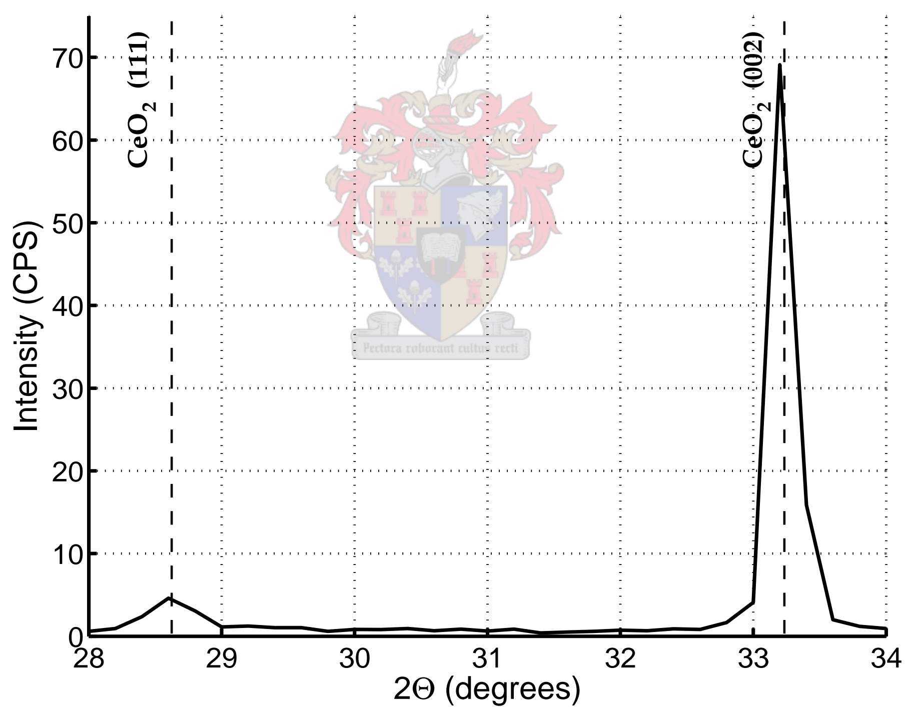

Figure B.1: Powder diffraction pattern for sample S1

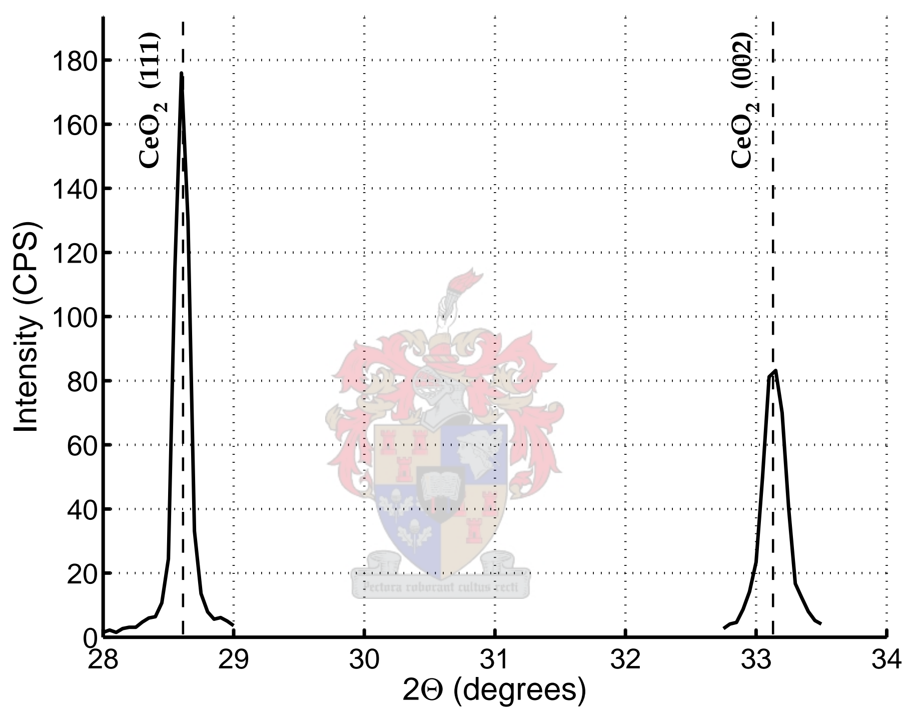

Figure B.2: Powder diffraction pattern for sample S2

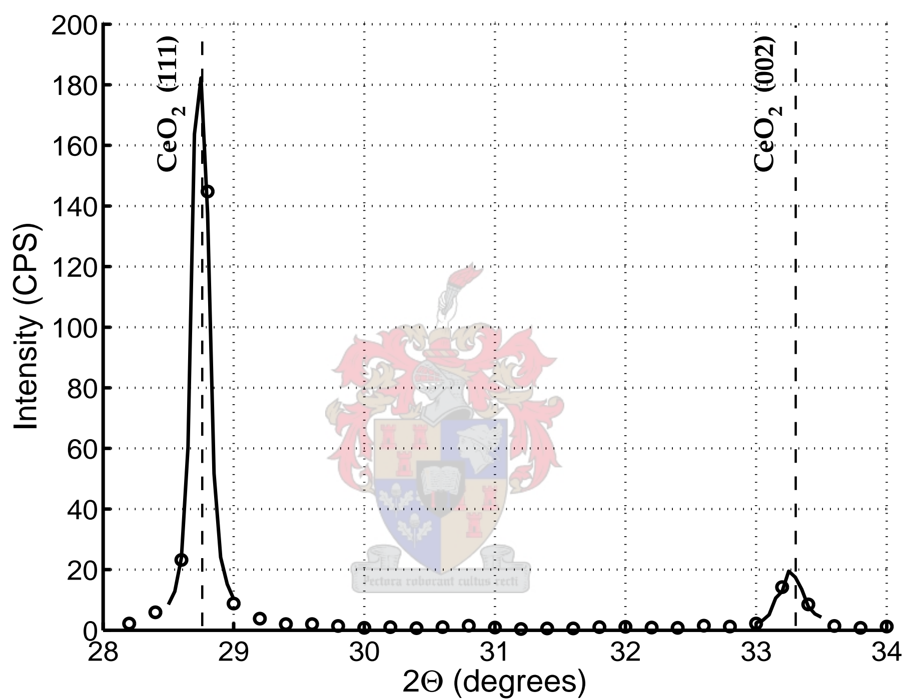

Figure B.3: Powder diffraction pattern for sample S3

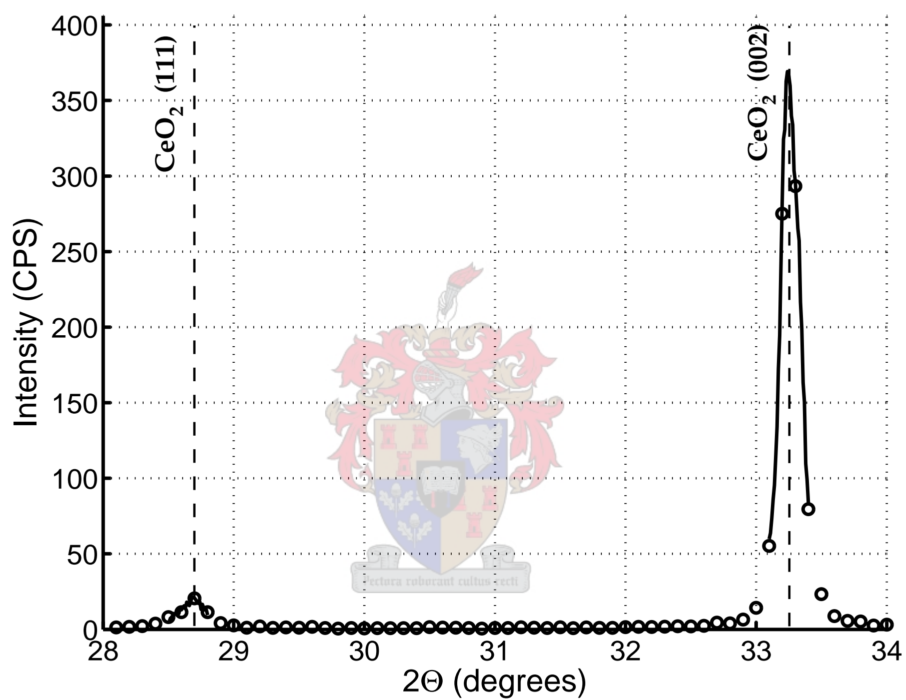

Figure B.4: Powder diffraction pattern for sample S4

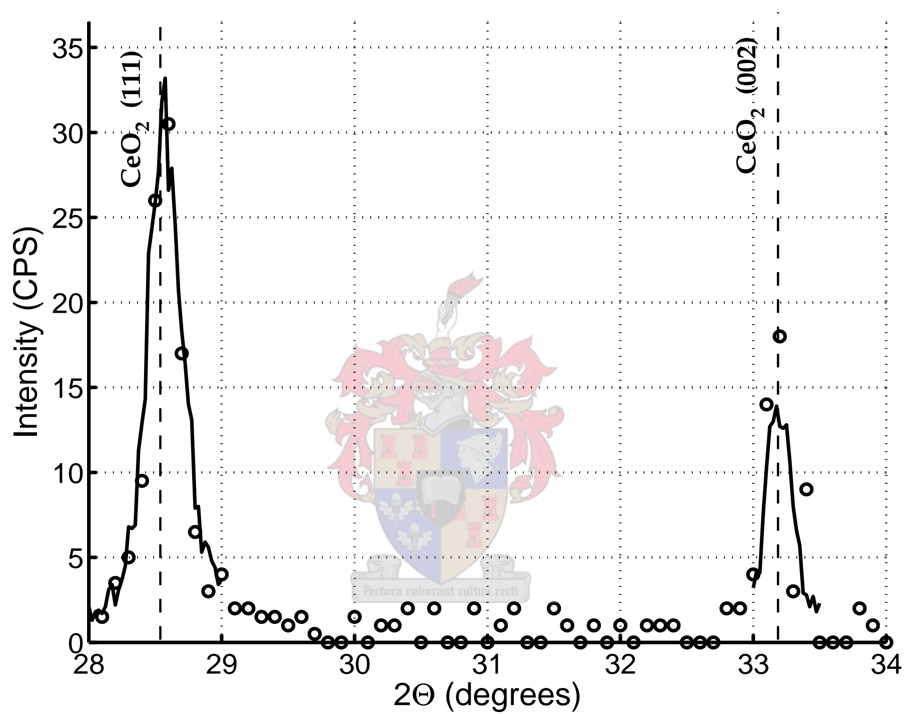

Figure B.5: Powder diffraction pattern for sample S5

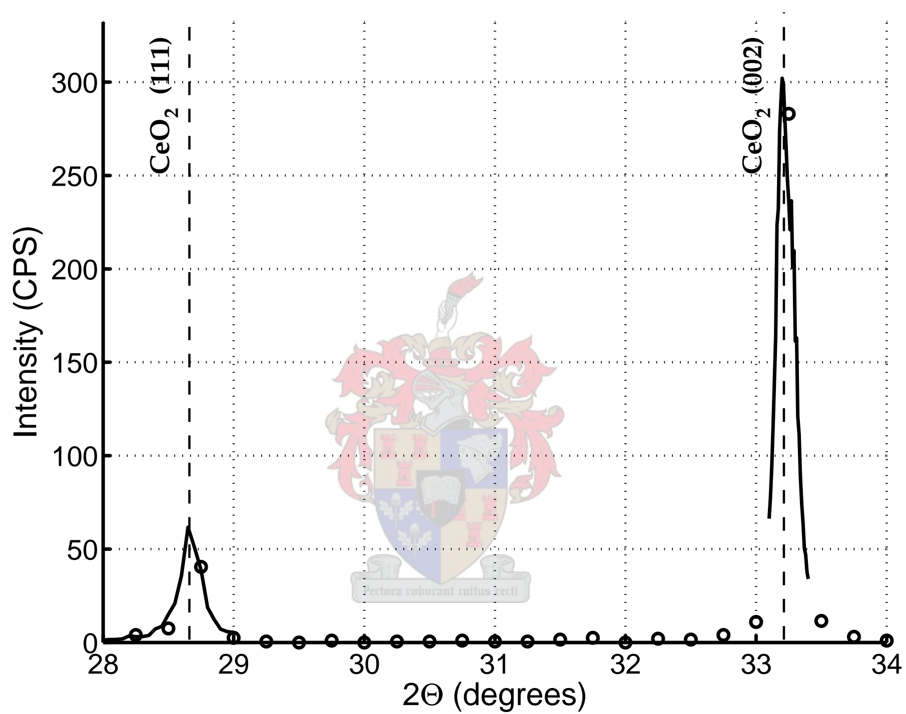

Figure B.6: Powder diffraction pattern for sample S6

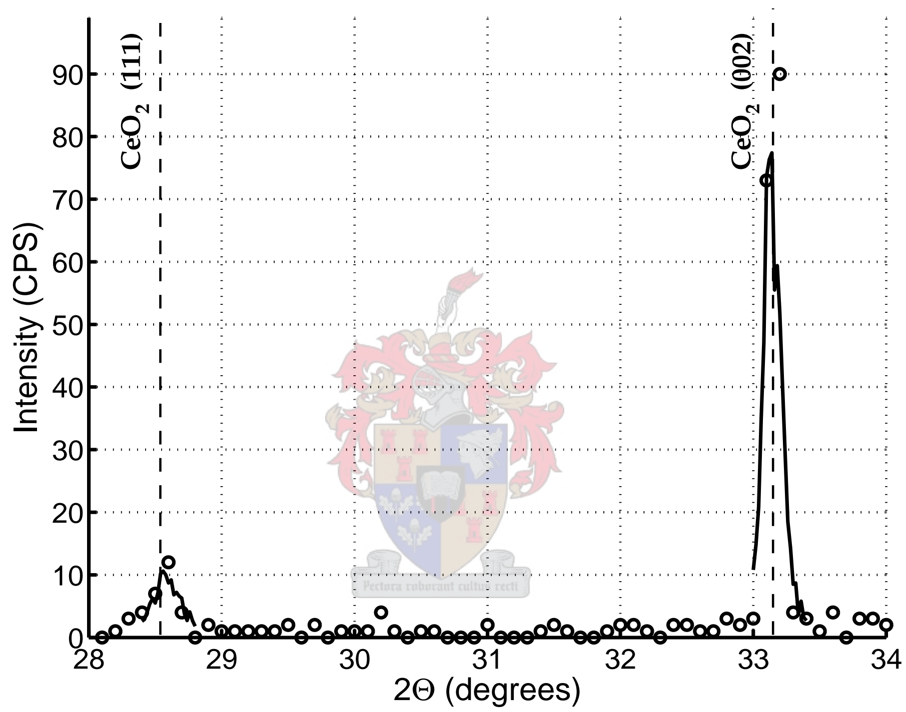

Figure B.7: Powder diffraction pattern for sample S7

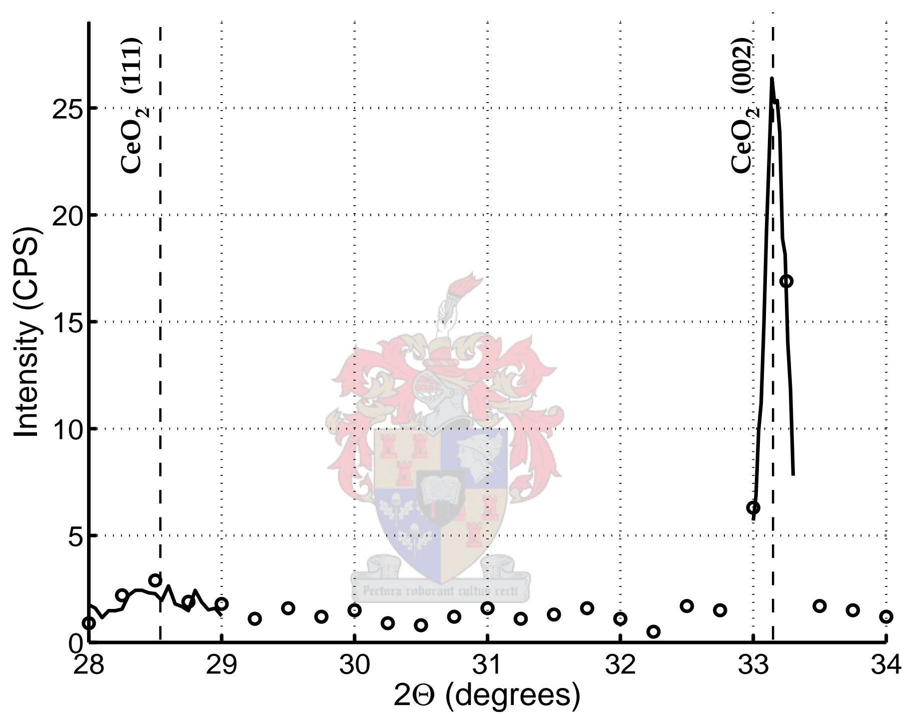

Figure B.8: Powder diffraction pattern for sample P1

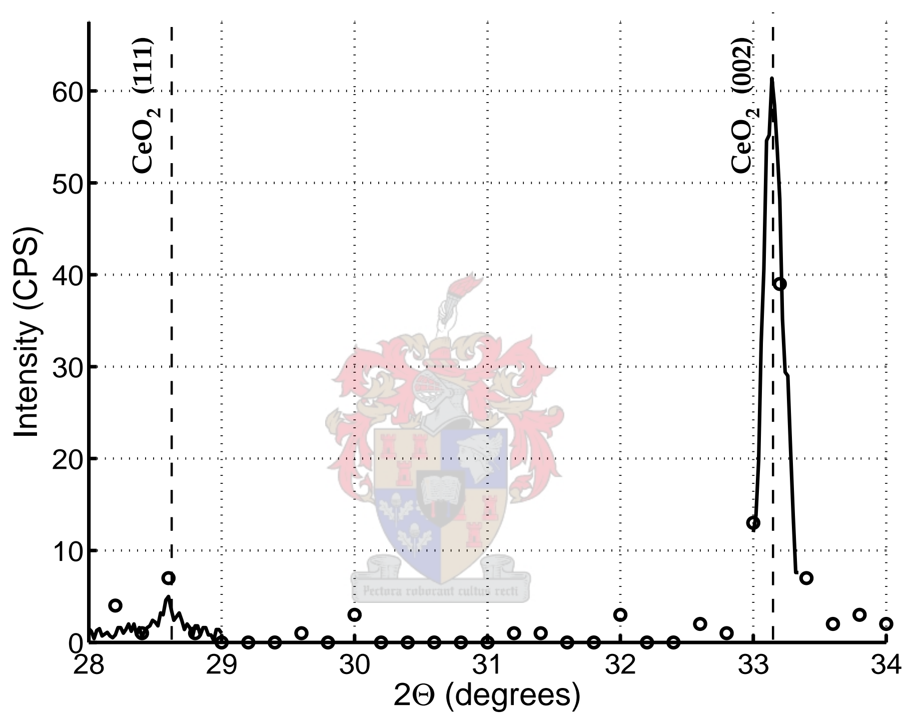

Figure B.9: Powder diffraction pattern for sample P2

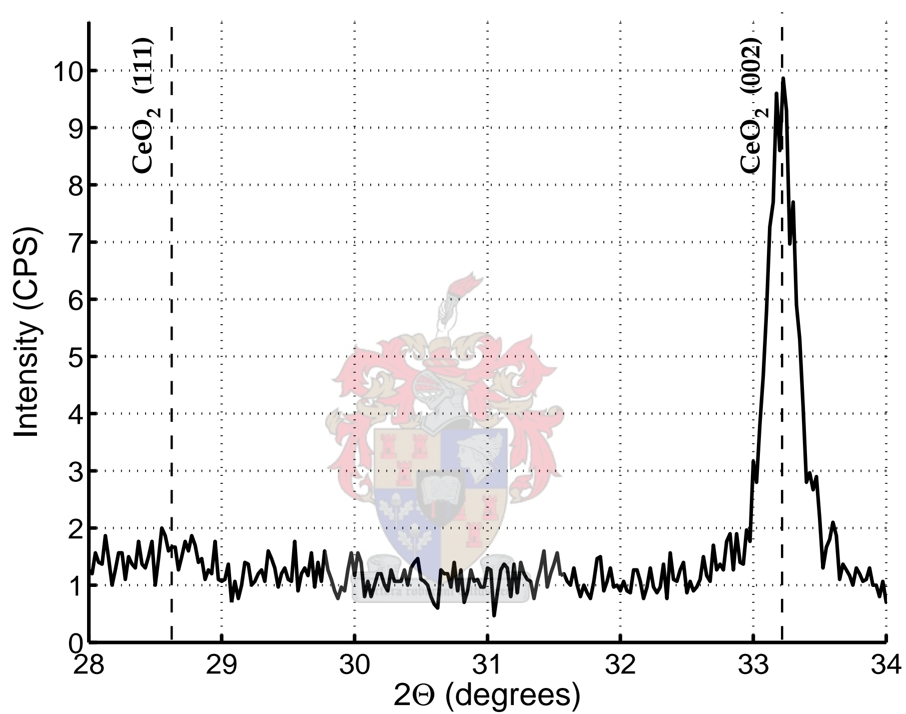

Figure B.10: Powder diffraction pattern for sample P3

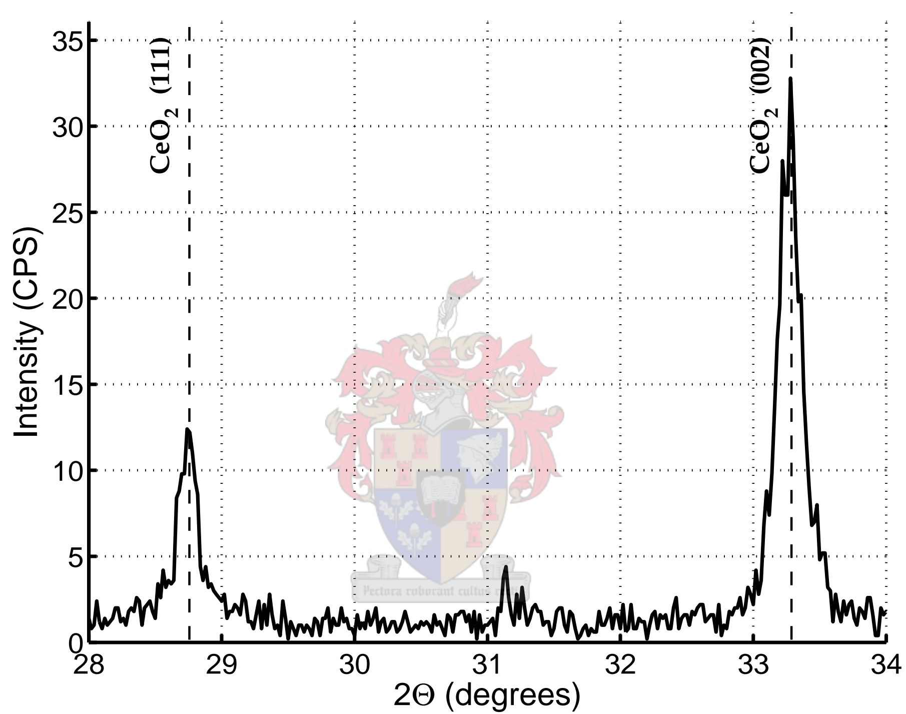

Figure B.11: Powder diffraction pattern for sample P4

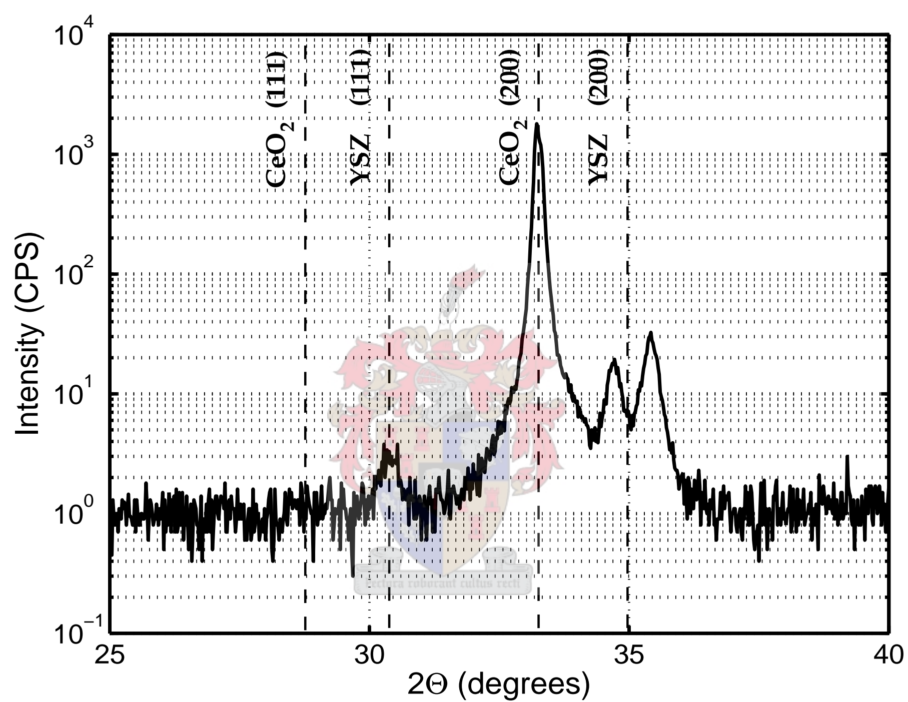

Figure B.12: Powder diffraction pattern for sample D1

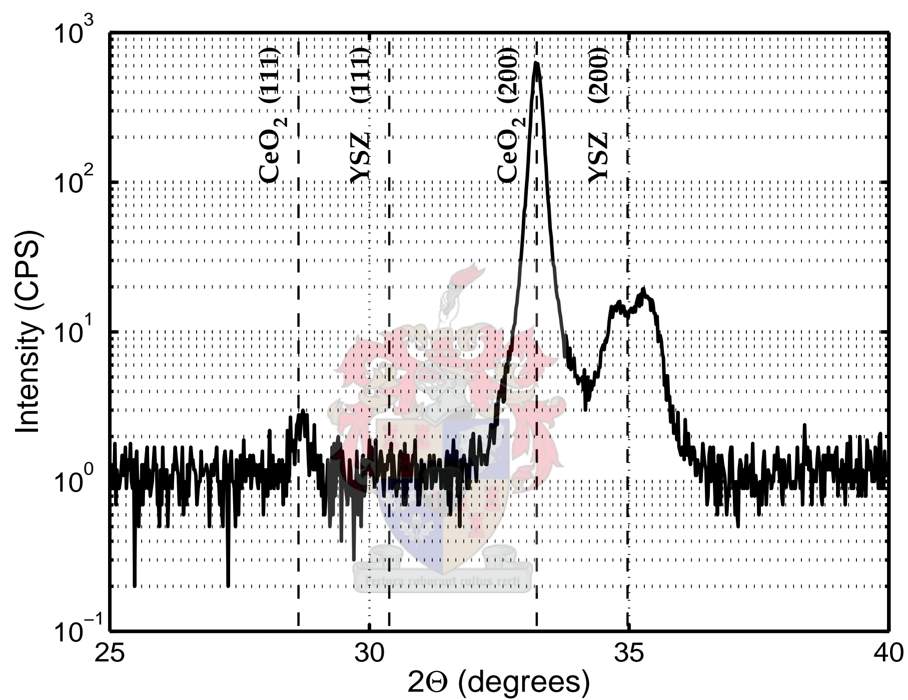

Figure B.13: Powder diffraction pattern for sample D2

Appendix C

Supplementary Results

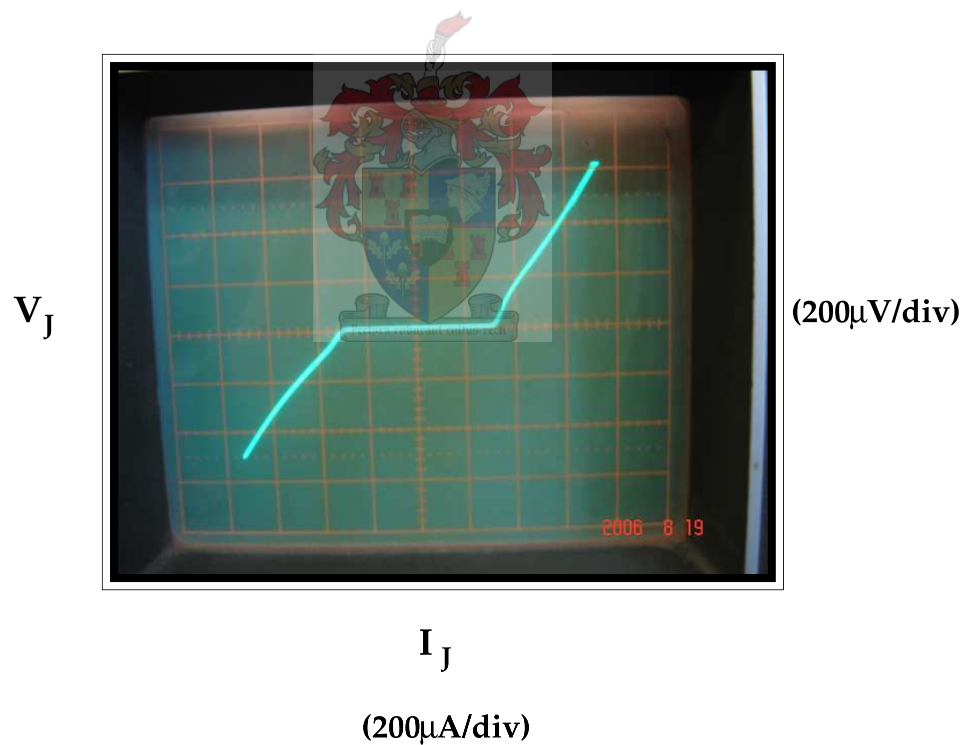

Figure C.1: I(V) curve for leg 6 of the prototype (T=42 K)

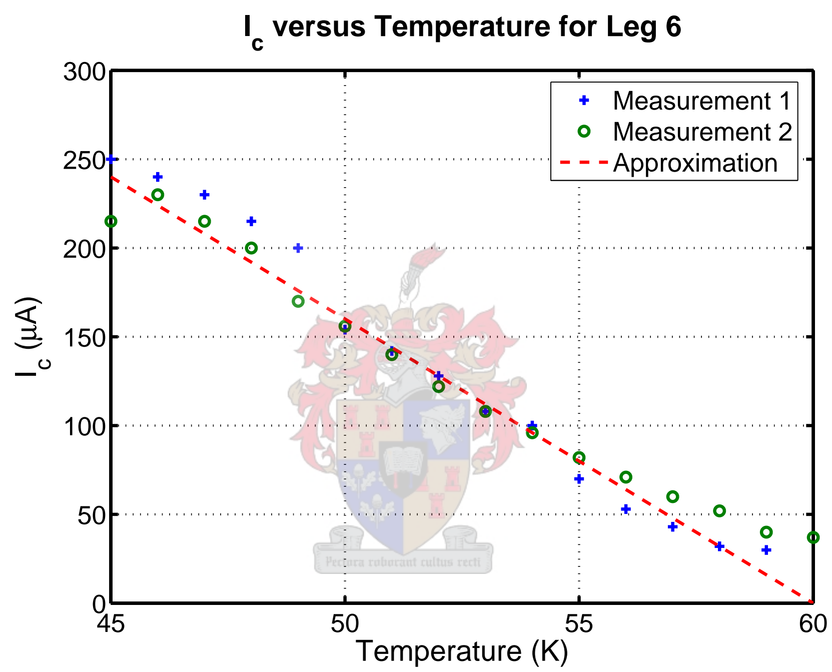

Figure C.2: Critical current versus temperature for leg 6 of the prototype

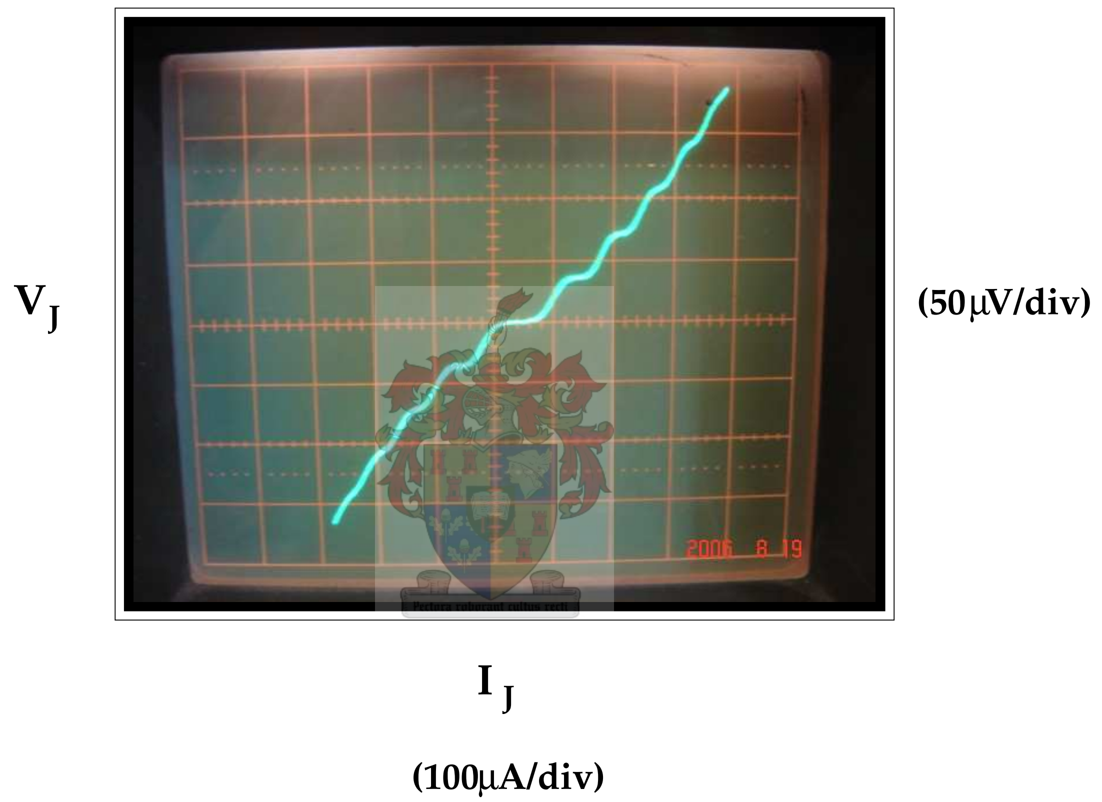

Figure C.3: Shapiro steps at 18.00 GHz for leg 6 of the prototype (T=42 K)

Appendix D

Axial Field of a Helmholtz Coil

In this appendix, a derivation of the magnetic field density at the centre of a Helmholtz coil setup will be presented. A Helmholtz coil consists of a pair of coils, each with n turns carrying a current I in the same direction. Each coil has a radius of R, which is also the distance separating the pair. To derive the magnetic flux density at a point halfway between the coils along the centre axis, we begin with the equation for the magnetic flux density along the z-axis for a coil lying in the x-y plane with the origin as its centre. The flux density is given by

Pectora roborant cultus recti

$$B_z = \frac{\mu_0 I R^2}{2(z^2 + R^2)^{\frac{3}{2}}} \tag{D.1.1}$$

where μ_0 is the permeability of free space [7]. Displacing the coil along the z-axis by a distance of $\frac{R}{2}$ gives a magnetic flux density at the origin of

$$B_z = \frac{\mu_0 I R^2}{2((\frac{R}{2})^2 + R^2)^{\frac{3}{2}}}. \tag{D.1.2}$$

Simplification of the preceding expression gives

$$B_z = \frac{1}{2}\left(\frac{4}{5}\right)^{\frac{3}{2}} \frac{\mu_0 I}{R}. \tag{D.1.3}$$

Given that there are 2 coils, and that each has n turns, the total field for the coil pair is thus given by

$$B_z = \left(\frac{4}{5}\right)^{\frac{3}{2}} \frac{\mu_0 n I}{R}. \tag{D.1.4}$$

Appendix E

Electron Back-scatter Diffraction

Microtexture analysis techniques measure the orientation of a few or even single grains at a time. This allows for the direct observation of grain boundary transitions and interface properties. In the past, transmission electron microscopy (TEM) has been the workhorse for such tasks. However, electron back-scatter diffraction (EBSD), a technique based on scanning electron microscopy (SEM) has revolutionised the field. It allows for the automated orientation mapping of samples, achieving spatial resolutions on the order of $0.5\,\mu$m. Samples can be taken at relatively high speeds (5 Hz or more) [29].

Pectora roborant cultus recti

EBSD operates by using an incident electron beam to generate a diffraction pattern which depends on the lattice parameters of the local crystal structure in the affected region, as well as its crystallographic orientation. The pattern generated in this way is referred to as a Kikuchi diffraction pattern. The manner in which the pattern is generated will now be discussed following the outline provided in [29].

A schematic representation of the diffraction geometry employed is shown in Figure E.1. The sample is tilted through an angle of about 60° to 70°. A focused beam of electrons is directed towards the area of interest on the sample surface. The electrons in the beam scatter diffusely in a manner which we can approximate as a point source relative to the size of the phosphor screen.

Since the point source emits electrons in all directions, there are incident electrons available

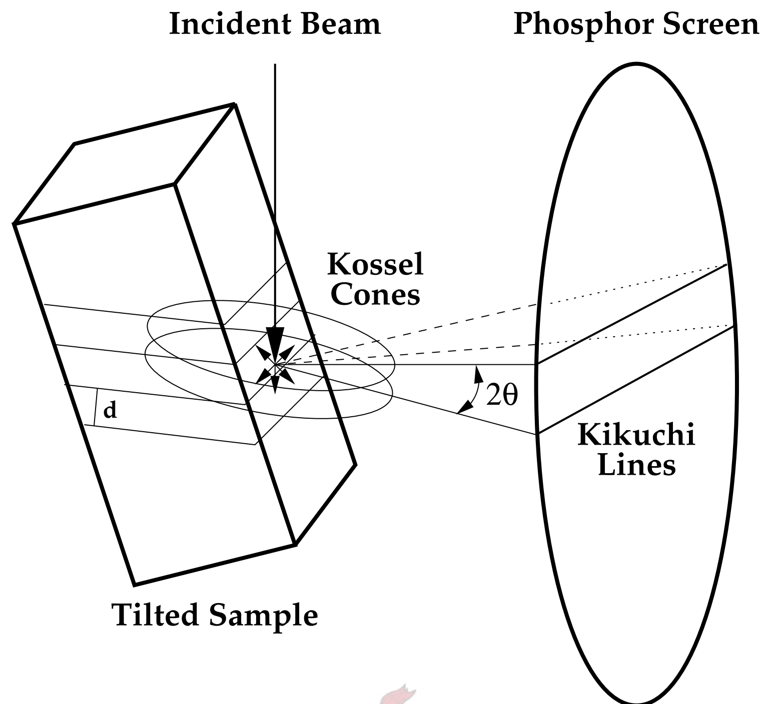

Figure E.1: Geometry for EBSD analysis (adapted from [29])

at the Bragg diffraction angle for each set of lattice planes. Bragg's law (4.3.5) can be satisfied for any rotation around the surface normal. Therefore, each set of lattice planes produces two cones (called Kossel cones), enclosing the top and bottom normals of the lattice planes respectively.

Each cone has an angle of $180°-2\theta_b$ at its apex (where θ_b is the Bragg diffraction angle). Since θ_b is generally quite small (around 0.5°), the cones are almost flat. If one places a phosphor screen some distance away from the point source, the cones intersect the screen in a fashion that is almost linear, forming a pair of Kikuchi lines for each set of lattice planes[1]. A line normal to a pair of Kikuchi lines is approximately an arc segment subtended by an angle of $2\theta_b$ with the point source as the origin. Therefore, we can find the interplanar distance (d) between a set of lattice planes from the distance separating the Kikuchi lines it produces.

[1]Generally, one finds that one of the lines (called the excess line) is more intense than the other (called the defect line). This difference is harder to distinguish using data obtained using EBSD than with TEM-based methods, where this effect becomes clearly visible.

Determination of grain orientation becomes possible when we observe that the orientation of the Kikuchi lines on the screen is dependent on the spatial orientation of the targeted grain within the sample. Given enough of these lines, we can extract the orientation of the targeted grain from the diffraction pattern. This ability of EBSD to target specific grains and provide their absolute orientation relative to the sample makes the method extremely attractive for research on grain boundary engineering.

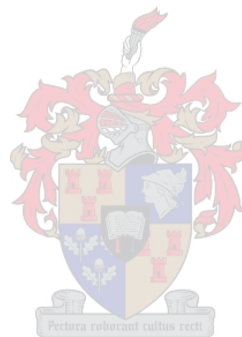

Bibliography

[1] M. N. R. Ashfold, F. Claeyssens, G. M. Fuge, and S. J. Henly. Pulsed laser ablation and deposition of thin films. *Chemical Society Review*, 33:23–31, 2004. (Cited on pages xi, 42, 44, and 47.)

[2] G. Aston and H. Kaufman. Ion beam divergence characteristics of three-grid accelerator systems. *AIAA Journal*, 17:64–70, 1979. (Cited on pages xii, 69, and 70.)

[3] U. Büttner. The development of fabrication equipment for thin-film nanostructures. Master's thesis, University of Stellenbosch, (Unpublished). (Cited on pages 57, 69, and 99.)

[4] K. Char, M. S. Colclough, S. M. Garrison, N. Newman, and G. Zaharchuk. Bi-epitaxial grain boundary junctions in $YBa_2Cu_3O_7$. *Applied Physics Letters*, 59:733–735, 1991. (Cited on page 23.)

[5] K. Char, M. S. Colclough, L. P. Lee, and G. Zaharchuk. Extension of the bi-epitaxial Josephson junction process to various substrates. *Applied Physics Letters*, 59:2177–2179, 1991. (Cited on page 26.)

[6] W. Chen, A.W. Rylyakov, V. Patel, J.E. Lukens, and K.K. Likharev. Rapid single flux quantum T-flip flop operating up to 770GHz. *IEEE Transactions on Applied Superconductivity*, 9:3212–3215, 1999. (Cited on page 1.)

[7] D. K. Cheng. *Fundamentals of engineering electromagnetics*. Addison-Wesley, 1994. (Cited on page 126.)

[8] D. B. Chrisey and G. K. Hubler, editors. *Pulsed laser deposition of thin films*. Wiley, 2003. (Cited on pages 42, 43, and 46.)

[9] E. H. Conradie. The design and fabrication of DC SQUID magnetometers. Master's thesis, University of Stellenbosch, 1998. (Cited on pages 24 and 105.)

Pectora roborant cultus recti

[10] C.A. Copetti, F. Rüders, B. Oelze, C. Buchal, B. Kabius, and J.W. Seo. Electrical properties of 45° grain boundaries of epitaxial YBaCuO, dominated by crystalline microstructure and d-wave-symmetry. *Physica C*, 253:63–70, 1995. (Cited on page 98.)

[11] F. W. Graser. A reproducible design and manufacturing process for SQUID magnetometers. Master's thesis, University of Stellenbosch, 2004. (Cited on pages 24, 52, 66, and 105.)

[12] R. Gross, L. Alff, A. Beck, O. M. Froehlich, D. Koelle, and A. Marx. Physics and technology of high temperature superconducting Josephson junctions. *IEEE Transactions on Applied Superconductivity*, 7:2929–2935, 1997. (Cited on page 18.)

[13] A. Gupta and B. W. Hussey. Laser deposition of $YBa_2Cu_3O_{7-\delta}$ films using a pulsed oxygen source. *Applied Physics Letters*, 58:1211–1213, 1991. (Cited on pages xii, 49, 50, 55, 56, and 57.)

[14] H. Hilgenkamp and J. Mannhart. Grain boundaries in high-T_c superconductors. *Reviews of Modern Physics*, 74:485–549, 2002. (Cited on pages xi, 20, 21, 23, and 31.)

[15] H. Hilgenkamp, J. Mannhart, and B. Mayer. Implications of $d_{x^2-y^2}$ symmetry and faceting for the transport properties of grain boundaries in high-T_c superconductors. *Physical Review B*, 53:14586–14593, 1996. (Cited on page 98.)

[16] J. R. Hook and H. E. Hall. *Solid state physics*. Wiley, second edition, 1991. (Cited on pages xi, 34, and 35.)

[17] Conductus Inc. *Mr. SQUID user's guide*. 1992. (Cited on pages 23 and 91.)

[18] C. Kittel. *Introduction to Solid State Physics*. Wiley, seventh edition, 1996. (Cited on page 67.)

[19] E. C. Knox-Davies. The design and fabrication of a high-T_c DC SQUID gradiometer. Master's thesis, University of Stellenbosch, 1999. (Cited on page 24.)

[20] D. Koelle, R. Kleiner, F. Ludwig, E. Dantsker, and J. Clarke. High-transition-temperature superconducting quantum interference devices. *Reviews of Modern Physics*, 71:631–686, 1999. (Cited on pages xi, 2, 11, and 19.)

[21] M. Y. Li, H. L. Kao, W. J. Chang, C. L. Lin, C. C. Chi, W. Guan, and M. K. Wu. Control of the in-plane epitaxy for bi-epitaxial grain boundary junctions using a new multilayer structure. *Journal of Applied Physics*, 77:4584–4588, 1995. (Cited on pages 28, 29, 59, 60, and 62.)

Pectora roborant cultus recti

[22] M. Madou. *Fundamentals of Microfabrication.* CRC Press, second edition, 2002. (Cited on pages xiv, 25, 66, and 68.)

[23] J. Mannhart, B. Mayer, and H. Hilgenkamp. Anomalous dependence of the critical current of 45° grain boundaries in $YBa_2Cu_3O_{7-x}$ on an applied magnetic field. *Zeitschrift für Physik B*, 101:175–179, 1996. (Cited on page 99.)

[24] A. Marcu, C. Grigoriu, W. Jiang, and K. Yatsui. Pulsed laser deposition of YBCO thin films in a shadow mask configuration. *Thin Solid Films*, 360:166–172, 2000. (Cited on page 52.)

[25] W. Massa. *Crystal Structure Determination.* Springer, second edition, 1999. (Cited on pages 36 and 39.)

[26] T. P. Orlando and K. Delin. *Foundations of applied superconductivity.* Addison-Wesley, 1991. (Cited on pages xi, 5, 6, 8, 11, 12, 13, 14, 15, and 19.)

[27] S. Pagano, B. Ruggiero, and E. Sarnelli. Magnetic-field dependence of the critical current in long Josephson junctions. *Physical Review B*, 43:5364–5369, 1991. (Cited on page 98.)

[28] K. Petersen, C. Stölzel, M. Schmitt, C. Krimmer, W. Wilkens, J. Söllner, H. W. Grueninger, and H. Adrian. Fabrication of biepitaxial YBCO Josephson junctions on different substrates. *IEEE Transactions on Applied Superconductivity*, 5:2180–2183, 1995. (Cited on pages 28, 29, 58, 73, and 92.)

[29] V. Randle and O. Engler. *Introduction to texture analysis.* Gordon and Breach, 2000. (Cited on pages xiii, 31, 128, and 129.)

[30] P. A. Rottier. Establishing a process for the fabrication of high-quality HTc SQUIDS. Master's thesis, University of Stellenbosch, 2002. (Cited on pages xiv, 24, 52, 57, 68, and 105.)

[31] R. K. Singh and D. Kumar. Pulsed laser deposition and characterization of high-T_c $YBa_2Cu_3O_{7-x}$ superconducting thin films. *Materials Science Engineering*, R22:113–185, 1998. (Cited on pages 18, 42, and 46.)

[32] L. H. Snetler. High-temperature superconductor step-edge fabrication for the implementation of RSFQ circuits. Master's thesis, University of Stellenbosch, 2004. (Cited on pages xii, 25, 66, 68, 69, 76, 77, and 83.)

[33] Z. Trajanovic, S. Choopun, R. P. Sharma, and T. Venkatesan. Stoichiometry and thickness variation of $YBa_2Cu_3O_{7-x}$ in pulsed laser deposition with a shadow mask. *Applied Physics Letters*, 70:3461–3463, 1997. (Cited on page 80.)

Pectora roborant cultus recti

[34] T. Van Duzer and C. W. Turner. *Principles of Superconductive Devices and Circuits*. Prentice Hall, second edition, 1999. (Cited on pages 5, 8, and 10.)

[35] C. Van Niekerk. An investigation into the manufacture and measurement of superconducting microwave devices. Master's thesis, University of Stellenbosch, 1995. (Cited on page 87.)

[36] W. F. Van Staden. The fabrication of PBCO buffered step-edge junctions. Master's thesis, University of Stellenbosch, 2006. (Cited on pages 69 and 99.)

[37] P. R. Willmott and J. R. Huber. Pulsed laser vaporization and deposition. *Reviews of Modern Physics*, 72:315–328, 2000. (Cited on page 48.)

[38] X. D. Wu, L. Luo, R. E. Muenchausen, K. N. Springer, and S. Foltyn. Creation of 45° grain-boundary junctions by lattice engineering. *Applied Physics Letters*, 60:1381–1383, 1992. (Cited on pages xiv, 27, 28, 38, 39, 59, and 62.)

[39] S. Y. Yang, C. H. Chen, H. E. Horng, W. L. Lee, and H. C. Yang. Characteristics of YBCO SQUIDs with step-edge and biepitaxial grain boundaries. *IEEE Transactions on Applied Superconductivity*, 9:3121–3124, 1999. (Cited on pages 58 and 92.)

[40] S. Y. Yang, H. E. Horng, W. L. Lee, H. W. Yu, and H. C. Yang. Fabrication of biepitaxial $YBa_2Cu_3O_{7-y}$ Josephson junctions and SQUIDs. *Chinese Journal of Physics*, 36:409–415, 1998. (Cited on page 28.)

[41] A. A. Yurgens. Intrinstic Josephson junctions: Recent developments. *Superconductor Science and Technology*, 13:R85–R100, 2000. (Cited on page 19.)

Pectora roborant cultus recti